A Lightweight High-sensitivity Chemical Mass Spectrometer for Organic Compounds

Zur Erlangung des akademischen Grades eines

DOKTORS DER NATURWISSENSCHAFTEN

von der Fakultät für Physik des

Karlsruher Institutes für Technologie (KIT)

genehmigte

DISSERTATION

von

M.Sc. Joel Ferreira de Brito

aus São Paulo

Tag der mündlichen Prüfung: 13. April 2011

Referent: Prof. Dr. Johannes Orphal
Korreferent: Prof. Dr. Thomas Leisner

Abstract

In this work a high-sensitivity Proton-Transfer-Reaction mass spectrometer (PTR-MS) has been developed for airborne measurements of Volatile Organic Compounds (VOCs). The spectrometer has two notable new features, an unheated permeation source for continuous calibration and an ion funnel (IF) enhanced drift tube. The former is specially designed for airborne deployment and, moreover, increases the system duty-cycle and accuracy. The latter has enhanced the system sensitivity in 30 %, achieving a limit of detection in the low pptv range for usual VOCs (pptv = 10^{-12} mol/mol), e.g. 4 pptv in 1 min integration time for acetone.

The new instrument, entitled PTR-IF-MS, shall be deployed on the new German research aircraft HALO, where lightweight construction is crucial. Almost entirely built in-house, the PTR-IF-MS weighs less than half of a standard PTR-MS system (57 kg instead of 120 kg).

Besides instrumental development, the first long-term study of the correlation between acetone and carbon monoxide in the upper troposphere (UT) is presented. Often emitted due to similar sources (e.g. biomass burning or incomplete combustion), both species can show a good correlation in the UT. Furthermore, the ratio between them, i.e. the correlation slope, contains information on their sources and the following chemical processing in the atmosphere.

The data used in this analysis were gathered over a period of 3 years onboard the CARIBIC passenger aircraft, where a strongly modified commercial PTR-MS, recently implemented with some features of the PTR-IF-MS, is regularly deployed. The correlation slope, given in pptv acetone/ppbv CO, shows a well pronounced increase with latitude. This parameter ranges from 12.2 at the equator to 33.9 at 60°N during summertime and from 7.6 to 16.5 during wintertime.

Zusammenfassung

Im Rahmen dieser Arbeit wurde ein hochempfindliches Protonen-Transfer-Reaktions-Massenspektrometer (PTR-MS) für flugzeuggestützte Messungen von flüchtigen organischen Verbindungen (VOCs) entwickelt. Das Spektrometer wurde durch eine unbeheizte Permeationsquelle zur kontinuierlichen Kalibrierung und einer mit einem Ionentrichter (engl.: Ion Funnel, kurz: IF) erweiterten Driftröhre bedeutend erweitert. Die kontinuierliche Kalibrierung erhöht die Frequenz des Mess-Zyklus sowie die Genauigkeit des Systems. Die Implementierung der elektrodynamischen Driftröhre führte zu einer Erhöhung der Empfindlichkeit des Systems um 30 % und somit zu einer Erniedrigung der Nachweisgrenze für übliche VOCs auf den unteren pptv (pptv = 10^{-12} mol/mol) Bereich, z.B. 4 pptv nach 1 min Integrationszeit für Aceton.

Das neue Instrument (PTR-IF-MS) soll auf dem deutschen Forschungsflugzeug HALO eingesetzt werden, für das eine besonders leichte Konstruktion von entscheidender Bedeutung ist. Das PTR-IF-MS, welches fast ausschlielich selbst entwickelt wurde, wiegt mit 57 kg weniger als die Hälfte eines Standard-PTR-MS Systems (120 kg).

Neben der Entwicklung des Instrumentes wird die erste Langzeitstudie zur Korrelation von Aceton und Kohlenmonoxid in der oberen Troposphäre (UT) vorgestellt. Da beide Verbindungen oft von gleichen Quellen (z.B. Biomasseverbrennung, unvollständige Verbrennung) stammen, können sie in der UT eine hohe Korrelation aufweisen. Darüber hinaus beinhaltet die Steigung der Korrelationsgeraden, also das Verhältnis beider Komponenten, Informationen über die Emissionsquellen und die erfolgten chemischen Prozesse in der Atmosphäre.

Die für diese Analyse untersuchten Daten wurden über einen Zeitraum von 3 Jahren mit einem stark modifizierten kommerziellen PTR-MS Gerät gemessen, welches regelmäig im CARIBIC Passagierflugzeug eingesetzt wird und zwischenzeitlich durch Elemente des PTR-IF-MS erweitert wurde. Die Steigung der Korrelationsgeraden in pptv acetone / ppbv CO zeigt einen ausgeprägten Anstieg mit dem Breitengrad. Dieser Parameter variiert im Sommer zwischen 12.2 am Äquator und 33.9 bei 60 nördlicher Breite und zwischen 7.6 und 16.5 im Winter.

Contents

Chapter 1

Introduction

Climate change is the most serious environmental issue mankind faces today, with various implications on economy and political stability [1–4]. All current predictions on future climate rely on models, which in turn strongly impact our present mitigation strategies [5, 6]. One fundamental cornerstone for validating and improving such climate models is the collection of highly accurate and highly resolved observations of the trace gas composition of the atmosphere, specially from airborne platforms. [7–9].

A key region in this respect is the upper troposphere and lower stratosphere (UT/LS). This region is located between ∼6 km and ∼20 km altitude and generates the major part of the natural greenhouse effect of ∼33 °C [10]. However, the UT/LS belongs to the less well-understood regions in the atmosphere, largely due to its difficult accessibility by appropriate trace gas instruments and its extreme dynamical and chemical complexity [11, 12].

This shortcoming led German scientists in the early 2000s to apply for a high-flying, long-endurance research aircraft. The proposal was successful and the German research ministry, together with some research institutions, bought a business aircraft (Gulfstream GV-550). After strong modification for research application, the aircraft was named **H**igh **A**ltitude and **LO**ng Range Research Aircraft (HALO[1]).

The Institute of Meteorology and Climate Research (IMK[2]), group Tropopause (TOP), was involved in planning and defining the research needs as well as the aircraft specifications. It proposed furthermore the construction of a mass spectrometer for the accurate measurement of diverse Volatile Organic Compounds (VOCs) onboard HALO.

VOCs, being all vapour-phase atmospheric organics excluding CO and CO_2, play

[1] http://www.halo.dlr.de/
[2] http://www.imk-asf.kit.edu

a fundamental role in the atmosphere [13, 14]. As pollutants they act as "fuel" for the production of the tropospheric ozone (O_3) [15, 16]. Furthermore, VOCs constitute a major source for aerosol particles, especially in the tropics [17, 18]. Indeed, many processes in which VOCs are involved are only qualitatively known and understood [19–21].

One further crucial process for the dry UT/LS is the production of the hydroxyl radical (OH) from the photolysis of acetone (CH_3COCH_3). The OH radical is known as the most efficient "cleaning agent" in the troposphere. This denomination reflects the large number of pollutants OH reacts with and which usually leads to their removal from the atmosphere [10].

The dominant role of acetone for the production of OH in the UT has been proposed in the 1990s [22–26]. However, some recent studies have considerably changed this picture [27], and furthermore, other important uncertainties on the role of acetone in this region continue to be raised [28]. To better quantify processes in which acetone is involved requires a fast and accurate measurement technique.

Real-time measurement of acetone and other VOCs aboard aircraft is essentially only possible with chemical ionization mass spectrometers (CIMS). CIMS are characterized by high sensitivity (in the pptv range, pptv = 10^{-12} mol/mol), time resolution from seconds to 1 minute, and weight usually between 120 to 250 kg [29–35].

Proton-Transfer-Reaction mass spectrometry (PTR-MS) stands out among chemical mass spectrometers due to its combination of low weight, sensitivity and usability[1] [29]. Currently, besides environmental research, PTR-MS technology is used in a wide range of applications such as medical, food and flavour science, etc. Given the variety of applications, the commercial PTR-MS version by IONICON (Innsbruck, Austria)[2] does not match airborne requirements such as light construction and the use of aircraft certified materials.

I joined the group TOP in April 2007 with the task of developing a custom-made PTR-MS for airborne application. Given the strong weight restriction usually associated with such deployment, the new system should be, besides accurate, very lightweight. Moreover, the system would be the first PTR-MS implemented with an Ion Funnel (hereafter referred to as PTR-IF-MS), an electrodynamic technique to increase the system sensitivity. The financing of the instrument and of my position was secured by a special HALO fund from the Helmholtz Association of German Research Centres (HGF) and the German Research Foundation (DFG).

[1] Due to soft ionization, low ion fragmentation simplifies spectra analysis.
[2] `http://www.ptrms.com/`

The system was planned to be deployed during the HALO campaign **O**xidation **M**echanisms **O**bservations (OMO) and missions thereafter. Originally planned for 2009, OMO has been successively postponed due to certification issues and currently is expected to take place in 2012, beyond the scope of this project. Therefore, we present a study of the correlation of two pollutants in the upper troposphere, namely acetone and carbon monoxide (CO). These observations were made onboard the passenger aircraft within the project CARIBIC[1] (Airbus A340). Currently our group deploys five in-situ instruments in CARIBIC (from a total of 15), including a strongly modified PTR-MS purchased in 2003 [36, 37].

Chapters 2 and 3 lay the foundation for this work, reviewing the role of VOCs in the atmosphere and the PTR-MS technology, respectively. The former presents an overview on chemical reactions in the atmosphere, VOC oxidation and budget analysis with focus on the role of acetone in the atmosphere, further discussed in a later section of this work. The latter includes a brief introduction to mass spectrometry techniques followed by presentation of state-of-the-art PTR-MS technology, including up-to-date alternative designs for a complete review.

The development of an unheated calibration source is detailed in Chapter 4, the ion funnel enhanced drift tube in Chapter 5, and the PTR-IF-MS in Chapter 6, concluding the instrumental development of this work. Chapter 7 presents the study of the correlation of acetone and CO in the upper troposphere. Chapter 8 concludes the work with a summary and outlook.

[1] **C**ivil **A**ircraft for the **R**egular **I**nvestigation of the atmosphere **B**ased on an **I**nstrument **C**ontainer. `http://www.caribic-atmospheric.com/`

Chapter 2

Volatile organic compounds in the atmosphere

2.1 The atmosphere

The Earth's atmosphere is composed primarily of the gases N_2 (78 %), O_2 (21 %), and Ar (1 %), whose abundances are controlled over geological timescales by the biosphere, uptake and release from crustal material, and degassing of its interior. Water vapour is the next most abundant constituent. It is found mainly in the lower atmosphere and its concentration is highly variable, reaching concentrations as high as 3% in the tropics and as low as 0.0003 % at the tropical tropopause at ∼18 km high. The remaining gaseous constituents, the trace gases, represent less than 0.1% of the atmosphere.

Although the troposphere accounts for only a small fraction of the atmosphere's total height, it contains ∼83 % of its total mass. It can be divided into the planetary boundary layer (PBL), extending from the Earth's surface up to typically 1-2 km, and the free troposphere, above the PBL, which extends to the tropopause.

A summary of the present-day composition of the atmosphere is given in Table 2.1. The trace gas concentrations are determined by an equilibrium between emission, in-situ formation and decomposition (chemical loss, photolysis, wet and dry deposition)

This Chapter will give an overview on distribution and chemical reactions of volatile organic compounds (VOCs) in the atmosphere. The term VOCs is used to denote the entire set of vapour-phase atmospheric organics excluding CO and CO_2.

Table 2.1: Mean gaseous chemical composition of the atmosphere at ground level. *Adapted from Prinn.* [38]

Constituent	Chemical formula	Mole fraction in dry air [a]
Nitrogen	N_2	78.08 %
Oxygen	O_2	20.95 %
Argon	Ar	0.93 %
Carbon dioxide	CO_2	385 ppmv
Neon	Ne	18 ppmv
Ozone (stratosphere)	O_3	0.5-10 ppmv
Helium	He	5.2 ppmv
Methane	CH_4	1.7 ppmv
Nitrogen oxides	NO_y	10 pptv-1000 ppbv
Hydrogen	H_2	550 ppbv
Ozone (troposphere)	O_3	10-500 ppbv
Nitrous Oxide	N_2O	310 ppbv
Carbon monoxide	CO	50-200 ppbv
Nonmethane Hydrocarbons	C_xH_y	5-20 ppbv
Hydrogen peroxide	H_2O_2	0.1-10 ppbv
Formaldehyde	CH_2O	0.1-1 ppbv
Sulphur dioxide	SO_2	0.01-1 ppbv
Ammonia	NH_3	0.01-1 ppbv
Chlorofluorocarbon 12	CF_2Cl_2	540 pptv
Carbonyl sulphide	OCS	500 pptv
Hydrogen sulphide	H_2S	5-500 pptv
Carbon disulphide	CS_2	1-300 pptv
Chlorofluorocarbon 11	$CFCl_3$	265 pptv
Dimethyl sulphide	CH_3SCH_3	10-100 pptv
Carbon tetrachloride	CCl_4	98 pptv
Methyl chloroform	CH_3CCl_3	65 pptv
Hydroperoxyl radical	HO_2	2 pptv
Hydroxyl radical	OH	0.05 pptv

[a] Especially short-lived compounds can show considerably variation.

[b] ppmv = 10^{-6} mol/mol; ppbv = 10^{-9} mol/mol; pptv = 10^{-12} mol/mol

VOCs play a central role in atmospheric chemistry and air pollution [13, 14]. Being pollutants themselves, VOCs also react with nitrogen oxides in the presence of sunlight to generate ozone [15, 16], a tropospheric pollutant. In the course of their various reactions, VOCs may form organic compounds with higher molecular weight which condense to produce secondary organic aerosols (SOA) [18]. By their very nature, the detailed chemical composition of SOA is seldom known and the aerosol is very difficult to characterise and quantify. Organic aerosols are indeed one of the largest unknowns in present climate modelling [19–21, 39].

Table 2.2 lists a number of VOCs found in the atmosphere along with their chemical group.

Table 2.2: Atmospheric Organic Species. *Adapted from Seinfeld and Pandis* [10]

Type of compound	General chemical formula	Example
Alkanes	R−H	CH_4, methane
		CH_3CH_3, ethane
Alkenes	$R_1C{=}CR_2$	$CH_2{=}CH_2$, ethene or ethylene
		$CH_3{-}CH{=}CH_2$, propene
Alkynes	RC≡CR	HC≡CH, acetylene
Aromatics	C_6R_6	C_6H_6, benzene
		$C_6H_5(CH_3)$,toluene
Alcohols	R−OH	CH_3OH, methanol
		CH_3CH_2OH, ethanol
Aldehydes	RC≡CR	CHCO, formaldehyde
		CH_3CHO, acetaldehyde
Ketones	RCOR	$CH_3C(O)CH_3$, acetone
Peroxides	R−OOH	CH_3OOH, methylhydroperoxide
Organic acids	R−COOH	HC(O)OH, formic acid
		$CH_3C(O)OH$, acetic acid
Organic nitrates	$R{-}ONO_2$	CH_3ONO_2, methyl nitrate
		$CH_3CH_2ONO_2$, ethyl nitrate
Alkyl peroxy nitrates	RO_2NO_2	$CH_3O_2NO_2$, methyl peroxynitrate
Acylperoxy nitrates	$R{-}C(O)OONO_2$	$CH_3C(O)O_2NO_2$,
		peroxyacetyl nitrate (PAN)
Biogenic compounds	C_5H_8	$CH_2{=}C(CH_3){-}CH{=}CH_2$, isoprene
	$C_{10}H_{16}$	α-pinene, β-pinane
Multifunctional species		$CH_3C(O)CHO$, methylglyoxal
		$CH_2(OH)CHO$, glycolaldehyde

The major classes of VOCs are alkanes, alkenes, aromatic hydrocarbons, and oxygenated compounds, with vegetative emissions typically being composed of alkenes (isoprene, monoterpenes, and sesquiterpenes) and oxygenated VOCs (including 2-methyl-3-buten-2-ol, acetone, methanol, cis-3-hexenol, cis-3-hexenyl acetate, and camphor). In urban air the nonmethane VOCs are typically made up of the following: alkanes, 40-45%; alkenes, 10%; aromatic hydrocarbons, 20%; and oxygenates, 10-15%; plus unidentified VOCs [40, 41].

2.2 Chemical reactions in the atmosphere

Three types of homogeneous chemical reactions occur in the atmosphere:

$$\text{First-order (unimolecular)} \qquad \mathrm{A} \rightarrow \mathrm{B} + \mathrm{C} \tag{2.1}$$

$$\text{Second-order (bimolecular)} \qquad \mathrm{A} + \mathrm{B} \rightarrow \mathrm{C} + \mathrm{D} \tag{2.2}$$

$$\text{Third-order (termolecular)} \qquad \mathrm{A} + \mathrm{B} + \mathrm{M} \rightarrow \mathrm{AB} + \mathrm{M} \tag{2.3}$$

The reaction rate of a first-order reaction is expressed as

$$\frac{d[\mathrm{A}]}{dt} = -\kappa_1[\mathrm{A}] \tag{2.4}$$

where [A] is the compound concentration (molecules cm^{-3} s^{-1}) and κ_1 the first-order rate coefficient (s^{-1}). The Eq. 2.4 can be integrated to give

$$[\mathrm{A}] = [\mathrm{A}]_0 \exp(-\kappa_1 t) \tag{2.5}$$

where $[\mathrm{A}]_0$ is the initial concentration.

In the atmosphere, by far the most important class of first-order reactions is photodissociation, or photolysis, in which absorption of a photon ($h\nu$) by the molecule induces a chemical reaction. Photodissociation reactions are written as

$$\mathrm{A} + h\nu \rightarrow \mathrm{B} + \mathrm{C} \tag{2.6}$$

in which $h\nu$ symbolizes a photon. First-order reactions include as well dry deposition at the Earth's surface and scavenging by cloud droplets [10].

Thermal decomposition of a molecule (e.g. PAN) is also represented as first-order reaction [42]. However, the energy required for decomposition is supplied through

collisions with another molecule M:

$$A + M \rightarrow B + C + M \tag{2.7}$$

Since M is at great excess relative to A and its concentration can be assumed to be constant, the concentration of M is considered in the reaction rate coefficient. Therefore the reaction can be simply written as $A \rightarrow B + C$.

Respectively, the rate of a second-order, or bimolecular, reaction is

$$\frac{d[A]}{dt} = -\kappa_2[A][B] \tag{2.8}$$

where the second-order rate coefficient κ_2 has units of cm^3 $molecule^{-1}$ s^{-1}.

2.2.1 Lifetime of compounds in the atmosphere

Atmospheric lifetimes vary from less than a second for the most reactive free radicals to many years (even millions) for the most stable molecules. Associated with each species is a characteristic spatial transport scale; species with very short lifetimes have comparably small characteristic spatial scales while those with lifetimes of years have a characteristic spatial scale equal to that of the entire atmosphere (Fig. 2.1). Depending on local conditions, hydroxyl radical (OH) may have a lifetime as short as 0.01 s, which corresponds to a spatial transport scale of only about 1 cm. Methane, on the other hand, with its lifetime of about 10 years, can become more or less uniformly mixed over the hemispheres. Spatial scales characteristic of various atmospheric chemical phenomena are given in Table 2.3.

Table 2.3: Spatial scales of atmospheric chemical phenomena [10].

Phenomenon	Length scale (km)
Urban air pollution	1 - 100
Regional air pollution	10 - 1 000
Acid rain/deposition	100 - 2 000
Toxic air pollutants	0.1- 100
Stratospheric-tropospheric exchange	0.1- 100
Tropospheric transport and oxidation processes	1 - 40 000
Stratospheric transport and oxidation processes	1 - 40 000
Aerosol-climate interactions	100 - 40 000
Stratospheric ozone depletion	1 000 - 40 000
Greenhouse gas increases	1 000 - 40 000

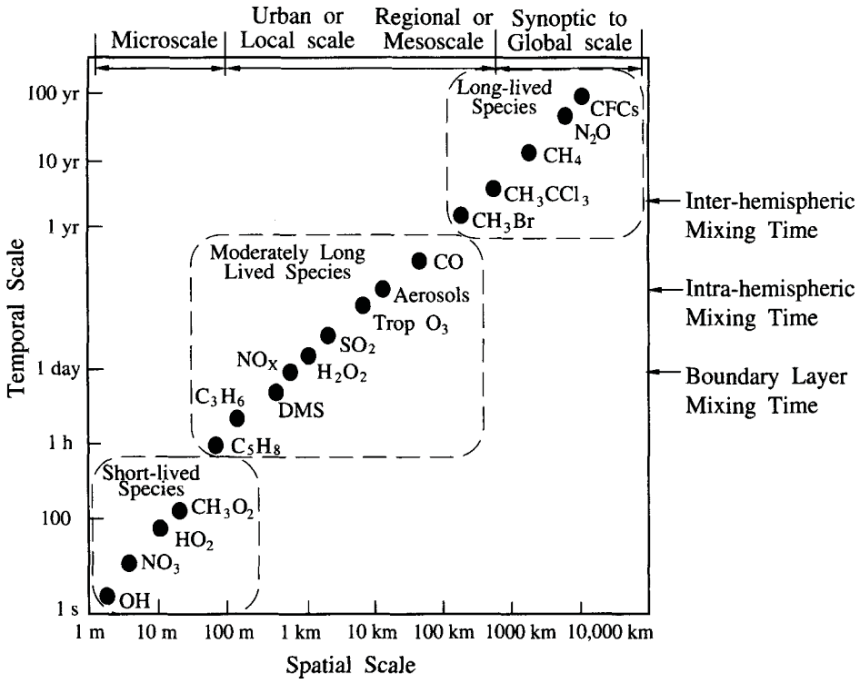

Figure 2.1: Characteristic spatial and temporal scales in the atmosphere. *Reproduced from Seinfeld and Pandis* [10]

2.3 VOC oxidation and budget analysis

Volatile organic compounds are emitted into the atmosphere from anthropogenic and biogenic sources and are formed in situ in the atmosphere during the degradation of other VOCs. Globally, with an emission rate of $\sim$1150 Tg (C) yr^{-1} of VOCs from biogenic sources (mainly vegetation) dominates over $\sim$100 Tg (C) yr^{-1} per year from anthropogenic sources. Nevertheless, in urban areas VOCs from anthropogenic sources often dominate [43].

In the troposphere, VOCs are transformed in other species due to photolysis, reaction with the hydroxyl (OH) radical, reaction with the nitrate (NO_3) radical (during evening and night-time hours), reaction with O_3, and in coastal and marine areas reaction with Cl atoms during day-time [10].

Whereas reactions specificities will depend on various classes of VOCs (alkanes, alkenes, alkynes, aromatics,...), the tropospheric reactions of VOCs share many reaction sequences in common. Moreover, certain areas of uncertainty which affect tropospheric ozone formation and NO_x cycling and removal are also common to almost all VOCs.

Photolysis and the initial reactions of many VOCs with OH radicals and NO_3 radicals lead to the formation of alkyl or substituted alkyl ($\dot{R}$) radicals, and the reactions of O_3 with alkenes and other VOCs containing >C=C< bonds lead to the formation of organic peroxy ($R\dot{O}_2$) radicals. A generalized tropospheric degradation scheme which is applicable for most VOCs is given in Fig. 2.2, showing that the intermediate organic radicals include alkyl (or substituted alkyl) radicals ($\dot{R}$), organic peroxy radicals ($R\dot{O}_2$) and alkoxy (or substituted alkoxy) radicals ($R\dot{O}$).

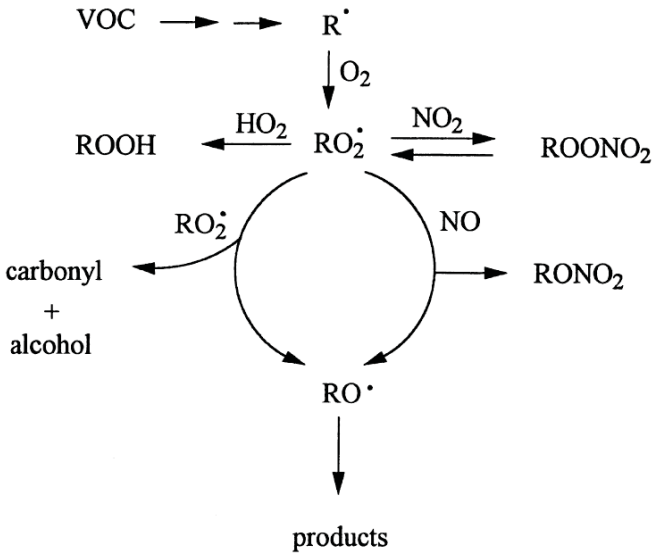

Figure 2.2: Generalized degradation scheme for VOCs. *Reproduced from Seinfeld and Pandis*[10].

The intermediate radicals $R\dot{O}_2$ and HO_2 play an important role in the O_3 production. O_3 is formed photochemically from the photolysis of NO_2,

$$NO_2 + h\nu \rightarrow NO + \dot{O} \tag{2.9}$$

$$\dot{O} + O_2 + M \rightarrow O_3 + M \tag{2.10}$$

where M is air. Since O_3 reacts rapidily with NO, the net result is a photoequilibrium between NO, NO_2 and O_3 with no net formation or loss of O_3.

However, in the presence of VOCs (including long-lived compounds such as methane), the degradation reactions of VOCs lead to the formation of intermediate $R\dot{O}_2$ and HO_2

radicals. These HO_2 and $R\dot{O}_2$ radicals react with NO, converting NO to NO_2,

$$HO_2 + NO \rightarrow OH + NO_2 \quad (2.11)$$

$$R\dot{O}_2 + NO \rightarrow R\dot{O} + NO_2 \quad (2.12)$$

which then photolyzes to form O_3, leading to a net formation of O_3.

The photolysis of O_3 and subsequent reaction with H_2O to form OH radicals leads to a decrease of O_3. In the absence of NO or at sufficiently low NO concentrations (which are defined below), reactions of O_3 with OH and HO_2 radicals

$$OH + O_3 \rightarrow HO_2 + O_2 \quad (2.13)$$

$$HO_2 + O_3 \rightarrow OH + 2O_2 \quad (2.14)$$

are additional loss processes for tropospheric ozone.

Net photochemical formation of O_3 versus net photochemical loss of O_3 in the troposphere therefore depends on the NO concentration, where the threshold NO mixing ratio of 10-30 pptv was identified [44]. NO mixing ratio above that value would lead to net photochemical O_3 formation whereas mixing ratio below would lead to net photochemical O_3 destruction.

As previously discussed, all VOCs are transformed in the troposphere by essentially the same processes. However, as evident from the range of tropospheric lifetimes for VOCs shown in Table 2.4, different VOCs react at differing rates in the troposphere.

In Chapter 7, results from correlation analysis between acetone and carbon monoxide in the upper troposphere is given. Therefore, a short discussion on the role of acetone in the atmopshere is provided.

2.3.1 The role of acetone in the atmosphere

Acetone is an omnipresent atmospheric specie with a mixing ratio in the range of 0.2-3 ppbv and an atmospheric inventory of 3.8 Tg [45, 46]. Under extremely clean conditions, ground-level background mixing ratios of 550 pptv have been found throughout the North hemispheric troposphere. In the free troposphere, acetone mixing ratios on the order of 500 pptv are present at northern mid-latitudes, declining to about 200 pptv at Southern latitudes [24].

Table 2.4: Calculated lifetimes for selected VOCs with respect to photolysis, reaction with the OH radical, reaction with the NO_3 radical, and reaction with O_3. *Adapted from Atkinson* [15].

	Lifetime due to[a,b]			
Organic	OH[c]	NO_3[d]	O_3[e]	Photolysis[f]
Limonene	50 min	3 min	2.0 hours	-
α-Pinene	2.6 hours	5 min	4.6 hours	-
Isoprene	1.4 hours	50 min	1.3 days	-
2-3-Butanedione	49 days	-	-	1 hour
trans-2-Butene	2.2 hours	1.4 hours	2.1 hours	-
Styrene	2.4 hours	3.7 hours	1.0 day	-
Pinonaldehyde	2.9 hours	2.3 days	>2.2 yr	-
Formaldehyde	1.2 days	80 days	>4.5 yr	4 hours
Propene	5.3 hours	4.9 days	1.6 days	-
Butanal	5.9 hours	-	-	-
Acetaldehyde	8.8 hours	17 days	>4.5 yr	6 days
Diethyl ether	11 hours	17 days	-	-
Benzaldehyde	11 hours	18 days	-	-
2-Butanol	1.3 days	17 days	-	-
Ethene	1.4 days	225 days	10 days	-
Toluene	1.9 days	1.9 yr	>4.5 yr	-
2-Pentanone	2.4 days	-	-	-
2,2,4-Trimethylpentane	3.2 days	1.4 yr	-	-
Ethanol	3.5 days	26 days	-	-
Dimethyl ether	4.1 days	180 days	-	-
Benzene	9.4 days	>4 yr	>4.5 yr	-
Propane	10 days	$\sim$7 yr	>4500 yr	-
Methanol[g]	12 days	1 yr	-	-
Acetone	53 days	>11 yr	-	$\sim$60 days

[a] Rate constants at $\sim$298 K.

[b] VOCs lifetime are often revised due to better understanding of reaction quantum yields, atmospheric budget and local concentration.

[c] For a 12-h daytime average OH concentration of 2.0×10^6 molecule cm^{-3}.

[d] For a 12-h nighttime average NO_3 concentration of 5×10^8 molecule cm^{-3}.

[e] For a 24-h average O_3 concentration of 7×10^{11} molecule cm^{-3}.

[f] For overhead sun.

[g] Wet and dry deposition also expected to be important.

From atmospheric data and three-dimensional photochemical models, a global acetone source of $95\pm15\,\mathrm{Tg\,yr^{-1}}$ has been estimated, composed of emission from terrestrial vegetation (33%), photochemical degradation of dissolved organic matter in oceans (26%), oxidation of C_3-C_5 isoalkanes (26%), oxidation of monoterpenes and methylbutenol (7%), emission from biomass burning (5%), emission from plant decay (2%), and from anthropogenic emissions (1%) [46].

It must be however stressed that there is still no agreement on the acetone budget. Recent studies, in fact, have modified significantly the estimated sources/sinks.

Currently it is widely thought that acetone has a net sink in the ocean [47, 48]. The lack of emissions from the ocean in the budget, however, is partially compensated by reduced photolysis yields [27] and increased biogenic emissions [47].

The long lifetime of acetone near the surface allows for transport out of the boundary layer [43], where its photolysis play an important role in the upper troposphere chemistry [24–26]. Its photolysis at wavelength λ=389 nm yields acetyl radicals

$$\mathrm{CH_3C(O)CH_3} + h\nu \;\rightarrow\; \mathrm{CH_3C\dot{O}} + \mathrm{C\dot{H}_3} \tag{2.15}$$

which then react with O_2 to produce peroxyacetyl radicals

$$\mathrm{CH_3C\dot{O}} + \mathrm{O_2} + \mathrm{M} \;\rightarrow\; \mathrm{CH_3CO(\dot{O}_2)} + \mathrm{M} \tag{2.16}$$

which can further react with NO_2 to form relatively stable peroxyacetyl nitrate (PAN)

$$\mathrm{CH_3CO(\dot{O}_2)} + \mathrm{NO_2} + \mathrm{M} \;\rightarrow\; \mathrm{CH_3CO(O_2)NO_2} + \mathrm{M} \tag{2.17}$$

In the cold, dry conditions of the upper troposphere, acetone photolysis is an important initiator of free-radical chemistry, leading to generation of O_3 and OH. Formerly it was assumed to be HO_x dominant precursor [22–26] although recent studies have considerably reduced it [27].

Instead of producing peroxyacetyl radicals (Reaction 2.16), acetyl radicals may react with O_2 as follows [25]:

$$\mathrm{CH_3C\dot{O}} + \mathrm{O_2} \;\rightarrow\; \mathrm{OH} + \text{products} \tag{2.18}$$

leading to a net formation of OH.

Theoretical calculations showed that reaction of HO_2 with acetone could be an important sink and source for acetic acid in the tropopause region [49]. Nevertheless

recent experimental results have not confirmed such claims [28].

Besides first retrievals from infrared spectrometers onboard balloons [50] and satellites [51], precise acetone data from the UT/LMS have originated from research aircraft campaigns [24, 30, 52–60].

Recently, results from CARIBIC project have been published (as depicted in Fig. 2.3) with the first systematic and regular monitoring of acetone in the extratropical UT/LS over a period of 3 years [34]. More accurate observations of acetone in the UT/LS are expected to contribute to a better understanding of its atmospheric budget and thus better quantification of its role in the oxidative cycle of the atmosphere.

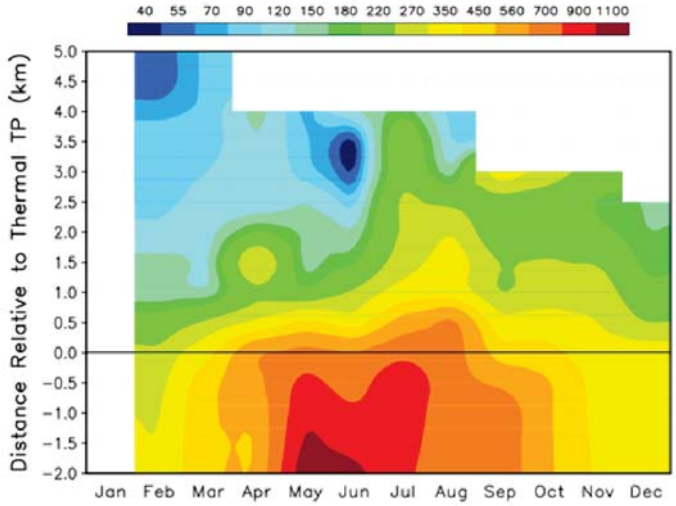

Figure 2.3: Seasonal variation of acetone in the UT/LS. Mixing ratios in pptv (see color scale) for a range of distances relative to the thermal tropopause. *Reproduced from Sprung and Zahn*[34].

2.4 Conclusion

This Chapter has presented a brief overview on the distribution and chemical reactions of VOCs in the atmosphere. Emitted from a wide variety of natural and man-made sources, in the troposphere, VOCs are transformed in other species mostly due to photolysis, reaction with OH, reaction with NO_3, and reaction with O_3. As a result from such reactions, VOCs may form secondary organic aerosols, one of the largest unknowns in present climate modelling.

Special focus is given on acetone, an omnipresent atmospheric specie. The relative long lifetime of acetone allows for transport out of the boundary layer where its pho-

tolysis leads to formation of PAN, one of the main compounds of the reactive nitrogen family (NO_y) and a major temporary NO_x reservoir gas. Acetone is considered to have an important role in the oxidative cycle in the atmosphere, still not accurately quantified.

The next Chapter describes the Proton-Transfer-Reaction mass spectrometry (PTR-MS), a chemical ionization technique for real time measurement of many VOCs which has strongly contributed for a better understanding of atmospheric chemistry in the past decade.

Chapter 3

Proton Transfer Reaction mass spectrometry

Proton-Transfer-Reaction mass spectrometry (PTR-MS) allows real-time measurement of Volatile Organic Compounds (VOCs) in air with high sensitivity. This Chapter presents an overview of the technique and is intended to familiarize the reader with state-of-the-art PTR-MS technology, referred throughout the rest of the work.

Up-to-date, the technology has been applied in a number of different fields including atmospheric chemistry [29, 61], air quality [62], aerosol formation chemistry [63], breath analysis [64, 65], flavor chemistry [66], food diagnostics [67, 68], and the study of biochemical pathways in plants and small animals [69, 70]. Here, focus will be given on the atmospheric chemistry application.

For a clear and elucidative presentation, this Chapter is divided according to the major components of a PTR mass spectrometer:

1. Ion source

2. Reaction chamber

3. Detection system

The function of each component will be outlined from Sections 3.2 to 3.4, along with the ongoing physical processes. Moreover, alternative designs to the so-called "standard" PTR-MS, which refer to the original design proposed by Lindinger et al. [71, 72], are briefly discussed. The use of different reagent ions allows different species to be detected. A review on alternative reagent ions is given in Section 3.5.

The calibration of the PTR-MS is discussed in Section 3.6. In this respect, see Chapter 4, where a new unheated calibration source designed for field campaigns is described. Finally, a short review on the application of PTR-MS in atmospheric chemistry is given in Section 3.7.

3.1 Historical background

3.1.1 Mass spectrometry is born

The mass spectrometry has not long ago completed 100 years of existence. J.J. Thomson, at the University of Cambridge, developed in 1897 an apparatus that, by the use of magnetic deflection, was able to measure the mass of the electron, an achievement for which he was awarded the Nobel prize in 1906 in physics. Later, mass spectrometry was used to separate and prove the existence of elemental isotopes. It was the importance of isotopes to the Manhattan Project and World War II that led its use to disseminate, mainly applied to better understand the fundamental nature of the atom.

Mass spectrometry first expanded outside nuclear physics in the 1930s. Together with biologists, Nier provided ^{13}C-enriched carbon for tracer studies. Along with geochemists, Nier measured ^{207}Pb/^{206}Pb in the planet's crust to determine the age of the earth as well.

By the 1940s, mass spectrometers were commercially available and MS was firmly established as a useful technique among physicists and industrial chemists. The next breakthrough was to use MS to identify unknown molecular structures, under leadership of McLafferty[73], Biemann[74], and Djerassi[75]. These three chemists in distinct groups in the U.S. revolutionized the use of mass spectrometers into the chemistry community and laid the groundwork for modern biological MS research.

In the 1950s, A.T. James and J.P. Martin proposed gas chromatography (GC) [76], a technique for compound separation that was some years later successfully coupled to a mass spectrometer by McLafferty and Gohlke. The technique is still largely used in many fields - including VOC analysis (more on Section 3.4.2).

3.1.2 From early mass spectrometers to the PTR-MS

Since Thomsom's first model, many orders of magnitude improvement in accuracy, limit of detection and mass resolution have been achieved. Nevertheless, mass spectrometry relies on the same key process, sample ionization and ion detection.

In 1966, Munson and Field led a revolution in sample ionization, developing the

chemical ionization mass spectrometry (CI-MS) [77]. It is considered of the origin of PTR-MS and many other techniques largely used nowadays.

Through electron impact, a primary molecule (present in large excess) is ionized forming the reagent ion $P^{\pm}_{ion}$ (Reaction 3.1). After being formed, the reagent ion undergoes gas phase ion/molecules reactions with a secondary compound S present at low concentration (usually $< 1\%$) creating the secondary ion $S^{\pm}_1$ and neutrals (Reaction 3.2).

$$\begin{aligned} e + P_{ion} &\rightarrow P^{\pm}_{ion} && (3.1)\\ P^{\pm}_{ion} + S &\rightarrow S^{\pm}_1 + N_1 && (3.2) \end{aligned}$$

It may occur that the product ion itself will fragment in one or more pathways (Reaction 3.3), hence, analysis of the array of ions $S^{\pm}_1$ to $S^{\pm}_i$ will provide valuable information on P, S and N.

$$\begin{aligned} S^{\pm}_1 &\rightarrow S^{\pm}_2 + N_2 \\ &\rightarrow S^{\pm}_3 + N_3 \\ &\rightarrow S^{\pm}_i + N_i \end{aligned} \qquad (3.3)$$

By making use of gas-phase ion/molecule reactions to ionize molecules of interest, the choice of primary and secondary compound can be tailored for every problem. In the analysis of VOCs, H_3O^+ is often used as primary ion ($P^{\pm}_{ion}$) due to its selective ionization and low fragmentation (slightly exothermic ionizing reaction with most VOCs).

Still in the 1960s, a major improvement in the CI-MS technique was made. Ferguson and co-workers introduced the so-called swarm technique, by making use of a flowing afterglow (FA) [78, 79]. Prior to the swarm technique, Reactions 3.1 to 3.3 were performed in one single reactor. However, in the FA, ions were stabilized in an ion source before being extracted through a gas flow into a separate chamber, where they would react with molecules.

A weakness of the technique was related to the reagent ion purity. For reactions of relatively simple ions, such as N^+_2, this caused little difficulty, but for more complex molecular ions, the possibility of producing a variety of secondary ions in the discharge source caused excessive complications in the product analysis. This key step was tackled by Adams and Smith in a ground-breaking piece of work that introduced the Selected Ion Flow Tube (SIFT) technique [80].

The basic components of a SIFT instrument are illustrated in Fig. 3.1. As in the flowing afterglow method, ions are produced by an electrical discharge, but now a

quadrupole filter allows ions of only a specific reagent ion ($P^{\pm}_{ion}$) to pass into the next part of the instrument, the flow tube.

In the flow tube, selected primary ions are mixed with flowing helium, whose purpose is to thermalize the ions for the ion/molecule reactions. The neutral reagent is added downstream of the inlet (after proper primary ion thermalization). The resulting ion products and unreacted ions are then detected by the mass spectrometer at the end of the flow tube.

Since the reaction time is solely determined by the distance travelled by the reacting mixture (flow tube) and the flow rate of the carrier gas, a kinetic analysis of the ion-molecule chemistry is possible if the flow rate is varied.

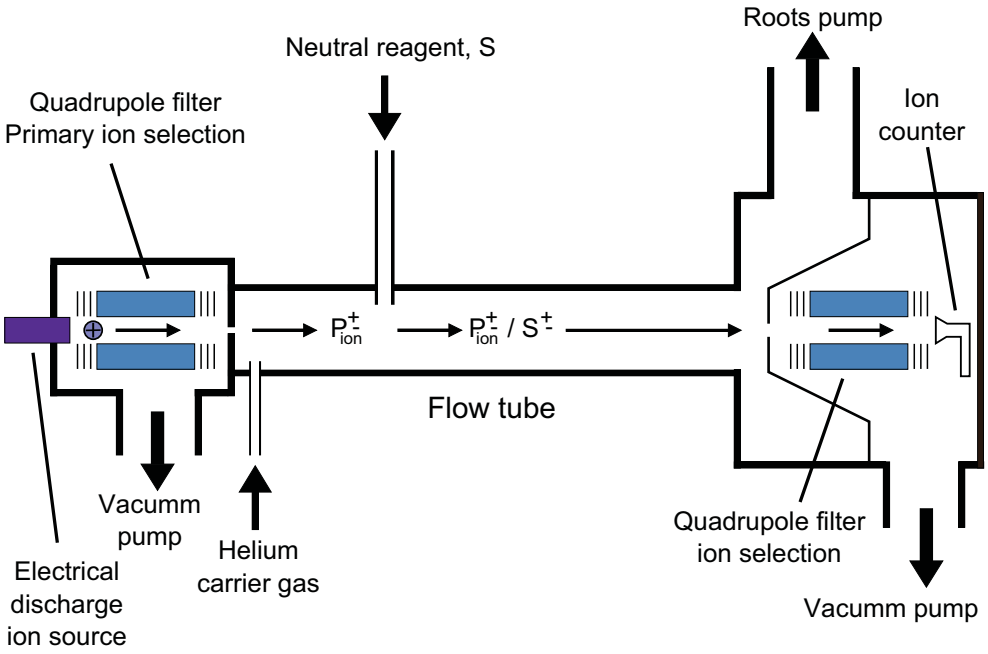

Figure 3.1: Schematic view of a Selected Ion Flow Tube instrument.

Early work with SIFT concentrated on fundamental studies of ion-molecule reaction kinetics as well as being of enormous value in other fields where ion-molecule reactions are important, such as atmospheric and interstellar chemistry. SIFT is still used today for the investigation of ion-molecule reaction kinetics, but it has also been developed as a means of detecting and quantifying trace gases in air [81, 82].

The apparatus employed is essentially the same as that shown in Fig. 3.1, but at the point where neutral reagent S is injected, the analyte sample (e.g. air) is continuously added instead. The focus on organic compounds is achieved by careful selection of

the reagent ions. Due to ionization selectivity, normal constituents of clean air are "transparent" to the spectrometer. As previously discussed, the most commonly used primary ion for VOCs analysis is H_3O^+, which ionizes via proton transfer reaction. Other ions, such as NO^+ and O_2^+, have also received considerable attention. A more detailed description of such ionization reactions will be given in the Section 3.3.

Variations of the SIFT-MS technique have been carried out. Lindinger and co-workers coupled a high purity H_3O^+ source with a flow drift tube in 1994 and showed that this was an effective approach to analyse trace organic gases in air [83]. In a flow tube, ions are transported by added carrier gas, whereas in a drift tube an electric field is responsible for the ion transport. A flow drift tube combines the two.

The effect of the electrical field in the selected ion flow drift tube mass spectrometry (SIFDT-MS) experiment is to increase the average collision energy of an ion with the buffer gas. This results in the declustering of hydrated hydronium ions of the type $H_3O^+ \cdot (H_2O)_n$, which tend to be formed in humid air and complicate kinetic analysis.

PTR-MS as it is known today was introduced by Lindinger in 1995 and involved two further important changes [71]. First, the mass filter that is employed in SIFT to select primary ions was dispensed and replaced with a hollow-cathode discharge source to generate H_3O^+ with high efficiency. A second innovation was to replace the flow tube with a relatively short drift tube (Fig. 3.2). Instead of employing a carrier gas to transport ions along the tube, the analyte air sample was directly injected into the drift tube and the unreactive components of the air (N_2, O_2, etc.) served as thermalizing agents, important for regulating the ion kinetic energy. The replacement of a drift tube where a DC field guides the ions instead of buffer flow allowed the use of much smaller pumps, improving its portability.

In SIFT-MS, the dilution of the analyte gas flow in excess helium is essential to minimize ion-molecule cluster formation, particularly those derived from residual water vapour. However, the substantially higher ion-molecule collision energies at the PTR-MS drift tube reduces $H_3O^+ \cdot (H_2O)_n$ and other cluster ions to considerably low levels without sample dilution. This can come at the expense of a shorter reaction time and some additional product ion fragmentation when compared to SIFT-MS, but the net result is a detection sensitivity for PTR-MS that is two orders of magnitude higher than that for SIFT-MS.

In the following, the major components of a PTR-MS are presented. In each Section, a general overview on the ongoing processes is presented, followed by description of the so-called "standard" version. Up-to-date published variations worth of note conclude each Section.

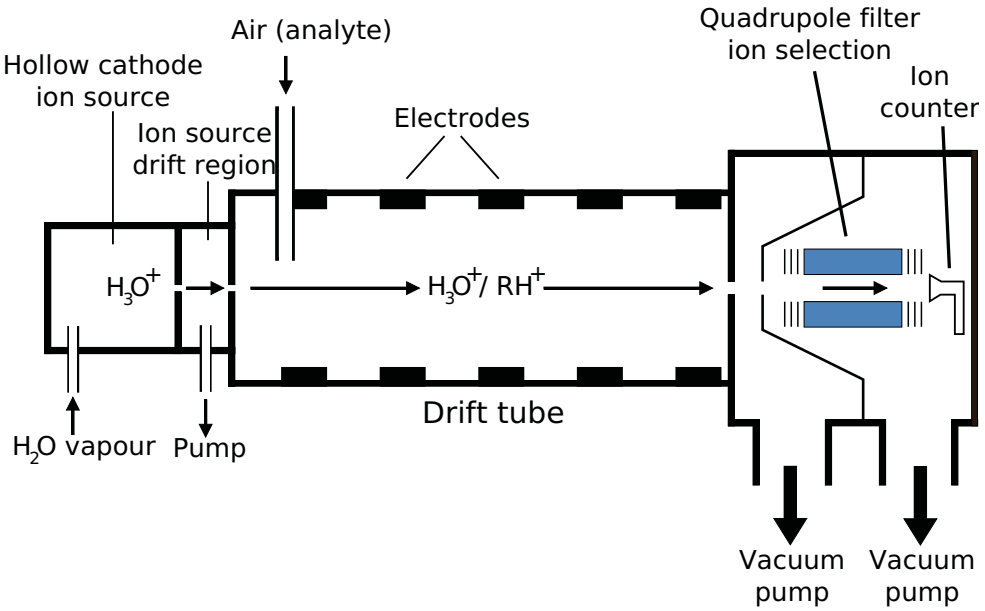

Figure 3.2: Schematic view of a PTR-MS.

3.2 The ion source

The chemical ionization reaction in the PTR-MS yields:

$$e^- + H_2O \rightarrow \ldots \rightarrow H_3O^+ \tag{3.4}$$

$$H_3O^+ + R \rightarrow H_2O + RH^+ \tag{3.5}$$

where H_3O^+ and RH^+ are the primary and secondary ions, respectively.

Note that Reaction 3.4 depicts only the first and last stage of the primary ion creation and the proton transfer depicted in Reaction 3.5 occurs only if energetically allowed, i.e. the proton affinity (PA) of R is higher than that of H_2O.

If RH^+ is assumed to be the only product, and, furthermore, conditions are chosen such that $[H_3O^+] \gg [RH^+]$, then a simple kinetic analysis shows that:

$$[RH^+] = [H_3O^+] \cdot \kappa \cdot t \cdot [R] \tag{3.6}$$

where κ is the proton-transfer rate coefficient and t is the reaction time.

VOC with mixing ratios as low pptv (pptv $= 10^{-12}$ mol/mol) can have an important role in the atmospheric chemistry, formation of secondary organic aerosol and influence

human health (Chapter 2). Consequently, high accuracy on low mixing ratios is an ongoing goal of in-situ VOC measurement devices.

The hollow cathode discharge source used in the PTR-MS provides a high number of H_3O^+ primary ions ($\sim 10^{10}$ ions/sec) with high degree of purity (>95%). However, the ion production rate is known to be extremely sensitive in many aspects, such as surface homogeneity (which deteriorates over time), pressure, geometry, H_2O purity, etc [29, 72].

For atmospheric VOC measurements, optimal behaviour of the ion source is crucial, because the system sensitivity is directly proportional to the number of primary ions in the reaction chamber (Reaction 3.6). Inversely, relative small changes in the ion source design have played an important role in the systems' large (factor ∼30) sensitivity improvement since first published by Lindinger et al. [71, 84].

3.2.1 The hollow cathode discharge source

The ion source used in the PTR-MS is called hollow cathode discharge source, or negative glow ion source. The former refers to the ion production process, by electrical discharge through a gas (e.g. water vapour). The latter to its violet light emitted by the ion-producing plasma.

The first report of a hollow cathode discharge (HCD) traces back to 1916, by F. Paschen. During many decades, it has been extensively used as a light source for spectrochemical analysis. In the 1970s, Howorka, Lindinger and colleagues published the use of HCD as an ion source for ion-molecule reaction analysis [85, 86].

Simply put, the HCD ion source combines two mechanisms, the glow discharge and the hollow cathode effect. The former deals with a controlled discharge which forms a plasma where electrons gain enough energy for ionizing or fragmenting neutrals. The latter increases the current density by a factor up to 10^3 due to geometrical considerations [87].

Through a quartz glass window at ion source, is possible to see the hollow cathode glow discharge and its different regions (Fig. 3.3). A more complete description of the ion production mechanisms in the HCD ion source is provided in Appendix A.

The ion source comprises two anodes (at same potential) and one cathode (Fig. 3.4). When the voltage between the electrodes is high enough, electrical breakdown occurs. Stability in ion production is ensured by regulating the discharge current. In the following, the PTR-MS ion source is presented.

Figure 3.3: View through a quartz glass of the ion production plasma and its regions on a HCD ion source. Picture taken during ion source optimization.

PTR-MS Ion source

The PTR-MS ion source is depicted in Fig. 3.4. It is usually supplied with 6 standard cubic centimetres per minute (sccm) of water vapour, extracted from the headspace of a liquid water reservoir.

At the ion source, ions such as O^+, H^+, H_2^+, OH^+ and H_2O^+ are produced. These ions undergo many collisions with the neutral gas in the hollow cathode. As Table 3.1 shows, all ions produced by electron impact react with H_2O and finally end up as H_3O^+ ions.

Table 3.1: Reactions of ions produced by electron impact upon H_2O [71].

Reaction				Rate constant (10^{-9}cm^3 s^{-1})
O^+	$+ H_2O$	$\rightarrow$	$H_2O^+ + O$	2.6
H^+	$+ H_2O$	$\rightarrow$	$H_2O^+ + H$	8.2
H_2^+	$+ H_2O$	$\rightarrow$	$H_3O^+ + H$	3.4
H_2^+	$+ H_2O$	$\rightarrow$	$H_2O^+ + H_2$	3.7
OH^+	$+ H_2O$	$\rightarrow$	$H_3O^+ + O$	1.3
OH^+	$+ H_2O$	$\rightarrow$	$H_2O^+ + OH$	1.8
H_2O^+	$+ H_2O$	$\rightarrow$	$H_3O^+ + OH$	1.8

By leaving the ion production region (through an orifice in the bottom anode), not

all ions have finished the reaction chain that ultimately leads to H_3O^+. Therefore, an intermediate chamber called ion source drift region (ISDR, Fig. 3.4, shown in yellow) has been considered [71].

A second function of the ISDR is to pump out most of the water vapour from the ion source to minimize water leakage into the reaction chamber (discussed in Section 3.3). At the end of the ISDR there is a second orifice that leads to the reaction chamber (seen in blue).

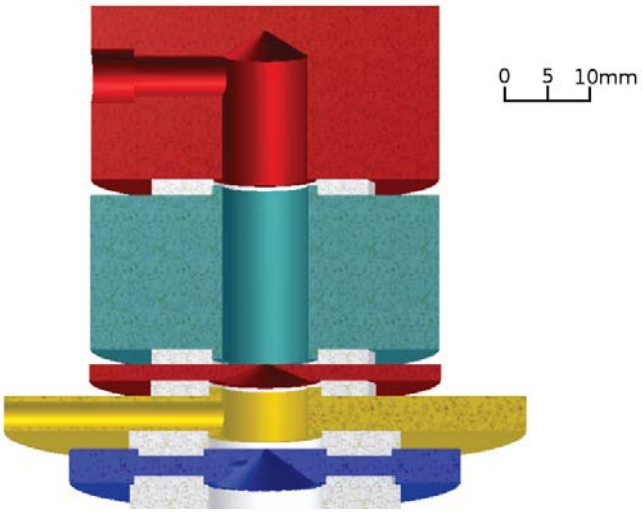

Figure 3.4: CAD view of the PTR-MS hollow cathode ion source. In red: anodes; in cyan: cathode; in yellow: ISDR; in blue: entrance to drift tube. Water vapour is supplied at the top anode and most of it is pumped out at the ISDR. The bottom anode orifice has a 0.6 mm diameter and the entrance of reaction chamber orifice has a 0.5 mm diameter.

By varying the accelerating voltage in the ISDR, more H_3O^+ ions will be transmitted into the reaction chamber, however at the cost of producing a higher fraction of O_2^+ and NO^+ impurity ions [29]. The latter are formed from air back streaming from the drift tube into the ion source. These impurity ions are unwanted as they undergo charge-transfer reactions with most VOCs [88].

Over time, carbon is deposited on the ion source walls. This arises either from impurities in the water vapour or air leak from drift tube and leads to a decrease in ion source efficiency. Therefore, ion source inner surfaces must be regularly (depending on discharge current and contamination rate) cleaned and polished.

Under standard operating conditions (pressure inside ion source ~3 hPa, 10 mm inner diameter), a voltage difference between cathode and anode of 600 V usually suffices for electrical breakdown to occur. The operating voltage stabilizes at around 450 V and

the ion current is regulated between 3-8 mA. Results presented in this work have been obtained with 5 mA discharge current.

3.2.2 Alternative designs

Despite small modifications, the ion source mostly used nowadays in the PTR-MS is essentially the same as presented by Lindinger et al. in 1995 [71]. Nevertheless, interesting alternative designs have been proposed throughout the years. In the following, a few selected designs are briefly discussed, completing the overview of state-of-the-art PTR-MS ion sources.

Radioactive ion source

An interesting alternative to the HCD ion source was proposed by Hanson et al. [89]. Instead of using electrical discharge, the ion source exploits a low-level α particle emitter, ^{241}Am, to ionize water vapour and generate H_3O^+. The α source is deposited on a metal strip located at the inner wall of a protective stainless steel cylinder, which replaces the discharge region in a hollow-cathode source. For this ion source, no external current driver is required and the long-term stability of the ion current is excellent [90].

Instead of pure water vapour, 20 sccm of a N_2/H_2O mixture is fed to the ion source. This acts to minimize the backstreaming of air and allows the drift tube to be operated at higher pressures, which confers higher VOC detection sensitivity (more on Section 3.3). Sensitivities of several hundred Hz per ppbv (ppbv = 10^{-9} mol/mol) were achieved for common VOCs such as acetone and isoprene, which means that detection sensitivities of a few tens of pptV for individual VOCs are possible in well under 1 s.

Although such ion source presents several advantages, some points are worth of note. In some circumstances (e.g. aircraft deployment), the inclusion of a radioactive component is undesirable from the (perceived) safety point of view. Moreover, the H_2O dilution in N_2 requires a high-pressurized gas bottle, thus increasing the instrument size/weight.

High pressure circular glow ion source

With the disadvantages of a radioactive ion source in mind, Hanson et al. presented a high pressure circular glow discharge ion source [91].

The ions are produced in a circularly shaped sub-normal glow discharge, where the discharge current is $\sim$45 μA at a voltage drop of $\sim$380 V. Unlike the radioactive ion source, the ion source is not fed with an H_2O/N_2 mixture. Instead, humidified clean

air (∼3 %) is supplied, obtained by a simple set-up of a catalyst converter and a water bubbler.

Due to its geometry it does not require a secondary chamber to convert unwanted ions to H_3O^+. By making use of humidified air, no additional pumping of the ion source is necessary. Moreover, it can be directly coupled with a higher pressure drift tube (Section 3.3).

Despite using a higher pressure in the drift tube, the reported sensitivity is comparable with a standard PTR-MS, which indicates a lower ion production efficiency. Moreover, impurity ions (O_2^+, NO^+) show comparable levels with standard systems (1.5–3%).

Planar ion source

An alternative plane electrode discharge source has recently been reported by Inomata and co-workers [92]. As in the hollow-cathode source (Fig. 3.4), there is both a primary discharge region and a source drift region prior to the drift tube, seen in Fig. 3.5.

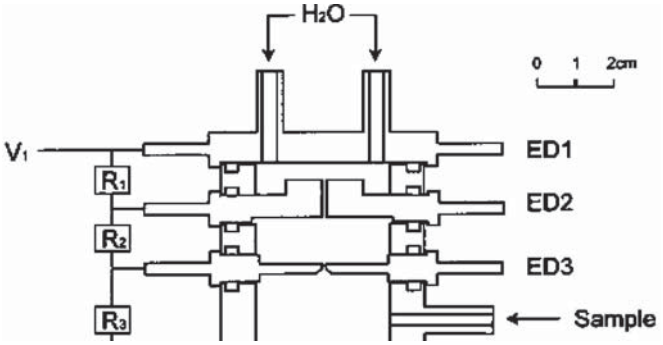

Figure 3.5: Planar ion source and drift tube proposed by Inomata [92]. ED1-ED2: Primary discharge region; ED2-ED3: ISDR.

The discharge is initiated by the entrance of water vapour between the anode and cathode plates. To help confine the discharge to this primary region, the primary and source drift regions are separated by a capillary of length 12 mm and diameter 1 mm in the cathode. With the capillary, air backstreaming is strongly reduced, therefore, even with a drift tube operated at a higher pressure (Section 3.3.2), the level of contamination by O_2^+ and NO^+ is low (∼0.5 %).

A lower H_3O^+ production rate from the ion source is compensated by high-pressure drift tube, achieving comparable sensitivity to a standard PTR-MS. Therefore, its main advantages relies on the low impurities production.

Off-axis ion source

In Section 3.6, sensitivity and measurement noise of the PTR-MS system will be discussed. Briefly, energetic photons created in the ion source glow discharge can reach the ion counter. This leads to quite high background noise, an issue partially overcome by tilting the drift tube. As such, due to the angle of inclination, most of the charged ions (but not the photons) will still follow the distorted electrical fields, being transmitted to the detection region.

Recently, Mikoviny et al. [93] presented a high temperature reaction chamber made of a resistive glass. However, due to its construction, tilting is not possible. In order to reduce noise on the detector, a new ion source had to be developed. In the proposed model, three off-axis hollow cylinder cathodes replace the standard PTR-MS ion source single on-axis cathode (Fig. 3.6). An exit anode lens with one central orifice of 0.8 mm diameter and three 0.5 mm diameter orifices, which were aligned with the cathode hollow cylinders. A water vapour flow of 8 sccm was supplied to the ion source.

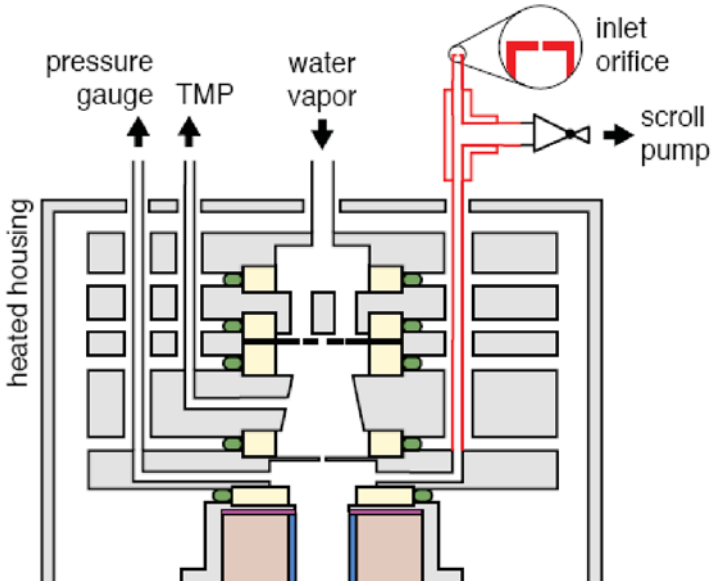

Figure 3.6: View of the off-axis ion source and drift tube proposed by Mikoviny et al. [93].

Ion production efficiency and impurity concentrations are comparable with the standard PTR-MS ion source, while maintaining low noise in the detector without tilting the drift tube.

3.3 The reaction chamber

The reaction chamber of a CI-MS is where the primary ions – H_3O^+ in the PTR-MS – will undergo ion/molecule reaction with neutrals (Eq. 3.5 on Page 22).

As previously discussed, due to the proton affinity, many compounds found in clean air (e.g. N_2, O_2, CO_2) will not be ionized. Therefore air acts as buffer gas and as analyte carrier. Table 3.2 depicts some of the compounds found in air and their proton affinity. Note that the detection mass is increased by one, due to the extra proton.

Besides ionization selectivity, another advantage in using H_3O^+ as primary ion arises from the relatively small proton affinity (PA) difference between water and most VOCs. A small PA difference means that the energy released by the reaction is considerably small (usually below 2.7×10^{-22} kJ or 1.7 eV), which strongly minimizes fragmentation that could otherwise complicate the spectrum analysis. However, for VOCs with proton affinity only slightly higher than that of water, the exothermicity of the ionization reaction (Reaction 3.5) is small and the rate coefficient of the reverse reaction

$$H_2O + RH^+ \rightarrow H_3O^+ + R \tag{3.7}$$

is non-negligible.

This is the case, for example, of formaldehyde. The rate coefficient for the reverse reaction is several orders of magnitude lower than that of the forward reaction, but since the H_2O concentration in the drift tube is much higher than the concentration of R, the overall rate of the forward and backward reactions can be comparable. Due to Chatelier's principle, the proton-transfer between H_3O^+ and VOCs such as formaldehyde is less efficient, and moreover, the overall rate depends on the humidity of the sampled air (Section 3.6).

The primary and secondary ions may cluster with water molecules in the sampled air as such:

$$H_3O^+ + nH_2O \leftrightarrow H_3O^+ \cdot (H_2O)_n \tag{3.8}$$

$$RH^+ + nH_2O \leftrightarrow RH^+ \cdot (H_2O)_n \tag{3.9}$$

Secondary ionization for most VOCs by proton transfer from a water clustered primary is allowed, as such:

$$H_3O^+ \cdot (H_2O) + R \rightarrow RH^+ + 2H_2O \tag{3.10}$$

Table 3.2: Proton affinity and mass of detection (if any) of some compounds found in air. *Obtained from NIST Chemistry WebBook*

Compound	Formula	Proton Affinity (kJ/mol)	Detection mass (amu)
Helium	He	177.8	-
Argon	Ar	369.2	-
Oxygen	O_2	421.	-
Nitrogen	N_2	493.8	-
Carbon dioxide	CO_2	540.5	-
Methane	CH_4	543.5	-
Carbon monoxide	CO	594.	-
Ozone	O_3	625.5	-
Water	H_2O	691.	19
Hydrogen sulphide	H_2S	705.	35
Hydrogen cyanide	HCN	712.9	28
Formaldehyde	CH_2O	712.9	31
Formic acid	HCOOH	742.0	47
Benzene	C_6H_6	750.4	79
Methanol	CH_3OH	754.3	33
Acetaldehyde	CH_3CHO	768.5	45
Ethanol	C_2H_5OH	776.4	47
Acetonitrile	CH_3CN	779.2	42
1,3-Butadiene[a]	C_4H_6	783.4	55
Acetic acid	CH_3COOH	783.7	61
Propanal	C_2H_5COH	786.0	59
Propanoic acid	C_2H_5COOH	797.2	75
Acetone	CH_3COCH_3	812.0	59
Isoprene	C_5H_8	826.4	69
Dimethyl sulphide	CH_3SCH_3	830.9	63
Ammonia[a]	NH_3	853.6	18
Nitrous acid[a]	HONO	858.4	30

[a] Despite compound ionization, ion source impurities complicate detection. Details in Section 3.5.

Since the PAs of $(H_2O)_n$ clusters are higher than that of H_2O, detection of species with a low PA (e.g. benzene and toluene) will be strongly dependent on humidity [94]. For all others, compound ionization is determined by Reactions 3.5 and 3.10 and is, consequently, independent of humidity. Nevertheless, it does not ensure a humidity-insensitive detection, given the different ion transmission for clustered ions and even possible mass overlap with other compounds/impurities.

By increasing the kinetic energy of the ions, the cluster hydrogen bond breaks as the ion collides with neutrals. This is accomplished by applying an electric field over the length of the drift tube. If the electrical field is set too high, ionization may occur by other channels (e.g. electron removal). Moreover, reaction (or drift) time is shorter at higher electrical fields, reducing the sensitivity. Therefore, the electrical field is usually chosen as a compromise between water clustered primary ions, fragments/impurities, and sensitivity.

3.3.1 Ion kinetics

When an electrical field E is applied, the ions will traverse the drift tube with an average drift velocity

$$\nu_d = \mu \times E \tag{3.11}$$

where μ is the ion mobility [95]. Generally, the reduced mobility μ_0 is defined as:

$$\mu_0 = \frac{p}{p_0} \times \frac{T_0}{T} \times \mu = \frac{N}{N_0} \times \mu \tag{3.12}$$

where p is the pressure, T the temperature, and N the number density of the gas in the drift tube. The parameter N_0 is the gas number density at standard pressure p_0 (1 atm) and temperature T_0 (273.15 K). Substituting Eq. 3.12 into 3.11 gives

$$\nu_d = \mu_0 \cdot N_0 \times (E/N) \tag{3.13}$$

Equation 3.13 shows the drift velocity as a function of the parameter E/N, which is frequently used when dealing with PTR-MS or ion mobility studies. It is expressed in units of Townsend (1 Td=10^{-17} V cm^2). Usual value for PTR-MS is around 120 Td, corresponding to an kinetic energy of the ions of 0.25 eV. The time t the ion takes to traverse the drift tube, and, correspondingly, the reaction time, is given by

$$t = \frac{L}{\nu_d} = \frac{L}{\mu_0 N_0} \times (E/N)^{-1} \tag{3.14}$$

An effective ion temperature T_{eff}, related to the kinetic energy, can be defined as well [96]:

$$\frac{3}{2}\kappa_B T_{\text{eff}} = \frac{1}{2}m_b\nu_d^2 + \frac{3}{2}\kappa_B T \tag{3.15}$$

where κ_B is the Boltzmann constant ($1.3806503\times10^{-23}\,\text{m}^2\,\text{kg}\,\text{s}^{-2}\,\text{K}^{-1}$) and m_b is the molecular mass of the buffer gas.

This equation is a modified version of the Wannier expression [97]. T_{eff} is a useful parameter for the calculation of cluster formation and, along with E/N parameter, often used for characterizing the system.

Using Eqs. 3.6 (Page 22) and 3.14, the fraction of H_3O^+ ions converted to RH^+ ions can be expressed as

$$\begin{aligned}\frac{[RH^+]}{[H_3O^+]} &= [R]\times\frac{\kappa L}{\mu_0 N_0}\times\left(\frac{E}{N}\right)^{-1} \\ &= \text{VMR}\times\frac{\kappa L}{\mu_0 N_0}\times\frac{N^2}{E}\end{aligned} \tag{3.16}$$

where VMR is the volume mixing ratio of a trace gas R. From Eq. 3.16 the normalized sensitivity can be obtained, defined as the signal of RH^+ ions obtained at a VMR of 1 ppbv and normalized to a H_3O^+ signal of 10^6 counts per second:

$$\text{Sensitivity} = 10^{-3}\times\frac{kL}{\mu_0 N_0}\times\frac{N^2}{E}\times\frac{\text{T}(RH^+)}{\text{T}(H_3O^+)} \tag{3.17}$$

The sensitivity is expressed in units of normalized counts per second and ppbv (ncps ppbv^{-1}). Sensitivity can be given in absolute values, simply multiplying by primary counts (in MHz). The factors $\text{T}(RH^+)$ and $\text{T}(H_3O^+)$ are the detection efficiencies for RH^+ and H_3O^+ ions, respectively. The differences in these factors are determined by the mass-dependent transmission of the mass filter and, to a lesser extent, by the electrostatic lenses, which focus the ions into the detection system. Detection efficiency is discussed in Section 3.4.

As the ions traverse the drift tube, through Brownian motion, they diffuse away from the centre axis. If an ion has diffused a distance large enough, it will be lost to the wall.

This distance can be quantified using the root-mean-square displacement (RMSD) of a one-dimensional δ-function after being subject to diffusion for the residence time in the drift tube t,

$$\text{RMSD} = \sqrt{2Dt} \tag{3.18}$$

with D being the transverse diffusion coefficient of the ion. For SIFT-MS, at vanishingly small electrical fields, this relationship is well established. However, the drift tube of a PTR-MS is not operated at vanishingly electric field but rather at E/N of ∼120 Td. At such conditions, RMSD is expected to be much higher, and moreover, quite different for different ions [98]. The RMSD obtained through ion trajectory simulation is discussed in Chapter 5.

3.3.2 The drift tube

The standard PTR-MS reaction chamber, or drift tube, is depicted in Fig. 3.7. The ion source drift region (discussed in Section 3.2.1) is shown in yellow and the entrance of the drift tube, in blue. The drift tube is 8.8 cm long, constructed with circular stainless steel guide plates (shown in dark gray) separated by teflon cylinders (in white).

An air flow of usually 35 sccm sustains a pressure of 2.3 hPa, where air exchange time is ∼0.2 s. The partial pressure of water in the drift tube usually amounts to 0.3 hPa. A voltage of 600 V (for E/N=120 Td) is applied along the drift tube. A sequence of resistors provides a linear voltage drop. With such conditions, the drift time is ∼100 μs.

With an orifice of 1.4 mm diameter, the drift tube end piece is depicted in light blue. An intermediate piece, shown in green, is at the same potential as the drift tube end piece. In orange is the nose cone plate, the last PTR-MS electrode before the entrance of the quadrupole filter, shown in brown.

3.3.3 Alternative designs

Several variations of the PTR-MS drift tube have been proposed over the years. Whereas many of those systems do not share the same applications (e.g. field campaigns), their description provides an overview on state-of-the-art PTR-MS technology. In the following, a few selected designs are briefly discussed.

50 cm long drift tube

In 2000, de Gouw and colleagues reported measurement of VOCs emitted from crops using a home-made PTR-MS with a 50 cm long drift tube [99, 100]. A longer drift tube allows for longer reaction time, hence larger sensitivities (they reported 78 ncps/ppbv for acetone, in comparison to the standard ∼20 ncps/ppbv). However, such drift tube presents two drawbacks: (i) a higher accelerating voltage is required for maintaining the same E/N ratio (3.5 kV), and most importantly, (ii) in order to maintain a fast air exchange time, the air flow must be increased to 360 sccm. Therefore, much larger

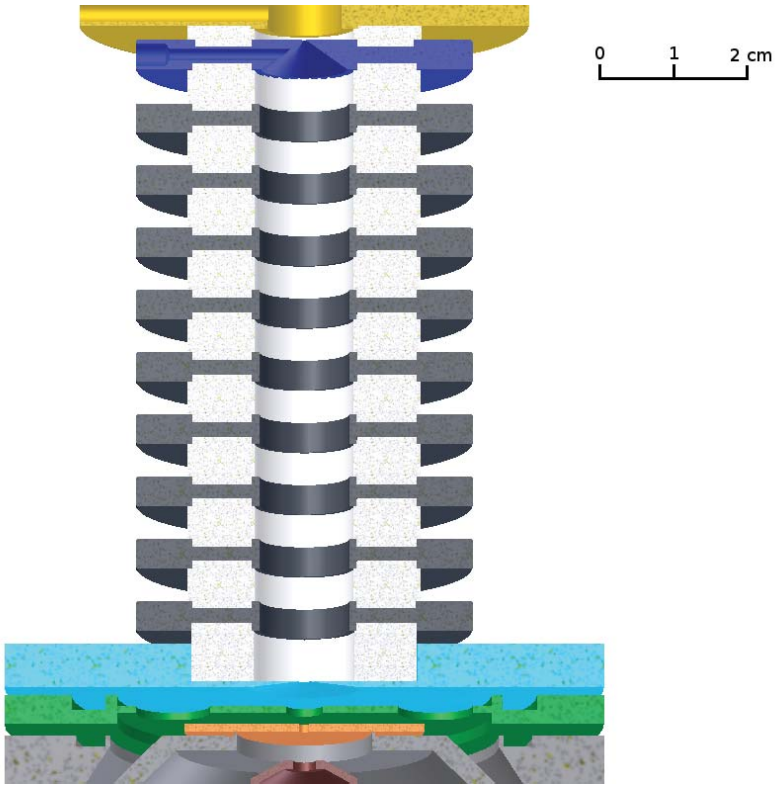

Figure 3.7: 8.8 cm long PTR-MS drift tube. In yellow: ion source drift region; blue: entrance of drift tube and sample air inlet; dark grey: stainless steel guide plates; white: Teflon cylinders; light blue: end plate of the drift tube; green: intermediate piece; orange: nose cone plate; brown: entrance of quadrupole; light grey: vacuum tubing. For details see text.

pumps are required, which decreases the system portability. With the usual PTR-MS drift tube flow (35 sccm), air exchange time would be above 5 s.

High pressure drift tube

Hanson and colleagues published a PTR-MS with a higher pressure drift tube [89, 91]. With an air flow of 80 sccm and end orifice diameter of ∼250 μm, the drift tube pressure is ∼11 hPa. Due to higher pressure, primary ions undergo higher number of collisions, therefore system sensitivity improves accordingly (e.g acetone is stated 240 ncps/ppbv).

Despite higher (normalized) sensitivity, a higher pressure drift tube presents some drawbacks: (i) The high pressure presents difficulties to cope with an ion source, and (ii) electrical discharge between the drift tube guide plates may occur due to the higher electrical field (∼370 V cm^{-1}) for E/N=110 Td.

High temperature drift tube

Two different groups have reported a high temperature drift tube. It has been used for aerosol measurements [101], or for measuring "sticky" or semi-volatile trace gases[93]. Both system are similar, however the latter will be described due to a more complete system description given on their publication.

This system has been previously mentioned (Section 3.2.2), due to its out-of-axis ion source. A high temperature (250°C) drift tube reduces strongly memory effect and allows measurement of compounds with vapour pressure as low as 7×10^{-7} hPa under ambient temperature. The system was operated under standard pressure and electrical field, 2.0-2.4 hPa and 80-130 Td, respectively.

Circular stainless steel guide plates and teflon spacers have been replaced by a 15 cm long resistive glass, which withstands temperatures of up to 400°C. The sealing materials (PEEK and Kalrez), however, lower the operating temperature to 250°C.

Memory effect has been quantified by removing abruptly the analyte from sampling air and measuring the $1/e^2$-signal decay. For pure hydrocarbons, no difference is seen between the PTR-MS operated at standard temperatures (∼50°C) and at 250°C, however for "sticky" compounds (e.g., dimethyl sulfoxide (DMSO), ammonia (NH_3), Monoethanolamine (MEA)), decrease time is usually orders of magnitude shorter.

Compounds with very low vapour pressure have been detected as well, such as Levoglucosan, a particle-bound marker for biomass burning with a vapour pressure of 7×10^{-5} hPa at 70°C (reponse time 8-54 s) and Cis-pinonic acid, a particle-bound oxidation product of α-pinene with an estimated vapour pressure of 7×10^{-7} hPa at

room temperature (response times between 1 and 6 min).

Drying of sample air with a cryogenic trap

In 2009, Jobson and McCoskey [102] proposed to use a cryogenic trap in the sample line. As such, sample air humidity is strongly decreased, facilitating measurement of compounds whose proton affinity are close to water (e.g. formaldehyde).

For cryogenic trap temperature of −30°C, drift tube voltage was such that E/N=80 Td, therefore even compounds that do not suffer so strongly with ionization back-reaction (as discussed in page 29) have usually a sensitivity improvement of 100%. Formaldehyde, even at 120 Td improved from 3.4 ncps/ppbv to 11.3 ncps/ppbv. At 80 Td, it was reported 25 ncps/ppbv.

Despite interesting results, discussion on possible memory effect or interference on air VOCs is not provided.

3.4 Detection system

The PTR-MS detection system consists of a quadrupole filter and a secondary electron-multiplier (SEM). The pressure in this region kept below 10^{-5} hPa to avoid electrical discharge in the SEM.

A CAD view of the detection system is shown in Fig. 3.8. In green and orange the lower pieces of the drift tube and the nose cone, respectively, are shown. The entrance of the quadrupole filter, shown in brown, consists of a set of lens design to tune the ion kinetic energy and ionic beam angle. The quadrupole rods are shown in copper and, in red, the 90° deflection plates. Ions are deflected 90° close to the electron multiplier in an effort to minimize spurious counts from ion source photons. The electron multiplier is schematically drawn in beige.

In the following, a closer view into quadrupole filtering is provided. Mathematical deduction of its operation is provided in Appendix B.

3.4.1 Quadrupole filter

The linear quadrupole, originally developed for mass spectrometry in the late 1950s by W. Paul and co-workers [103], is widely used as an ion filter, ion guide, or adapted as a linear ion trap. In this Section, the application of the quadrupole as an ion filter is presented.

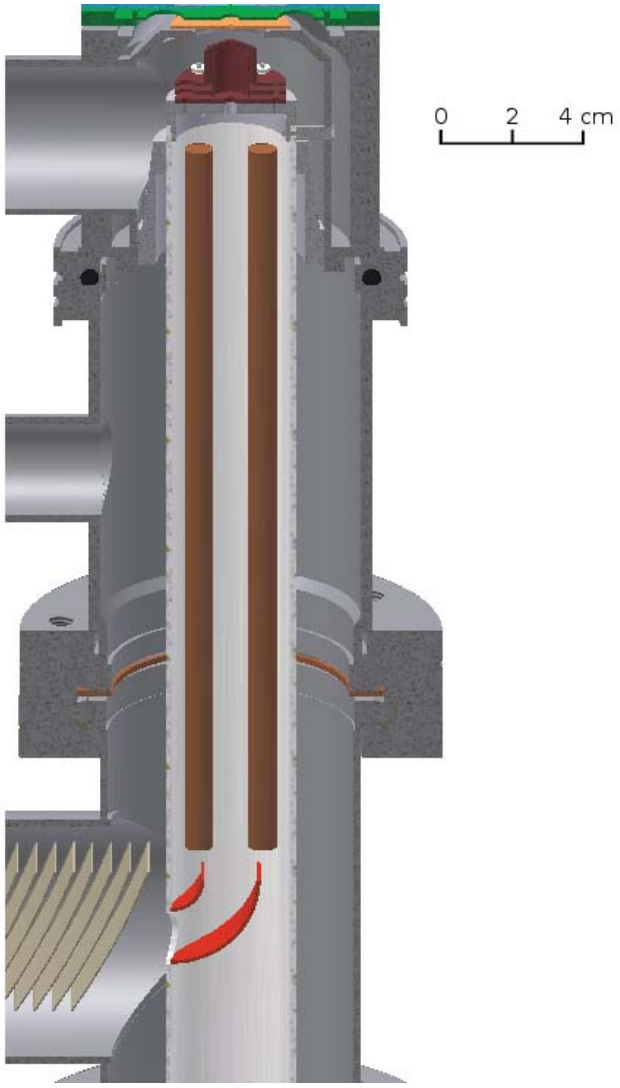

Figure 3.8: Cut view of detection system. In green: lower pieces of the drift tube; orange: the nose cone; brown: entrance of the quadrupole filter; copper: the quadrupole rods; red: 90° deflection plates; beige: electron multiplier. Details see text.

A quadrupole filter comprises four rods where ions travel along their axis. By combining a DC and RF field, only ions with certain m/z are allowed to pass through. Trajectory stability (deduced in Appendix B) is described considering variables a_x and q_x, in the x direction, defined as:

$$a_x = \frac{8z \cdot e \cdot U}{m \cdot r_0^2 \cdot \Omega^2} \tag{3.19}$$

$$q_x = \frac{4z \cdot e \cdot V_{\mathrm{RF}}}{m \cdot r_0^2 \cdot \Omega^2} \tag{3.20}$$

where z is the number of charges on the ion, e the electron charge in Coulomb, U the DC voltage applied pole to ground in volts, Ω, the angular frequency of the RF field in Hz, m the ion mass in kg, r_0 the distance from the centre to any rod in meters and V_{RF} the amplitude of RF field in volts.

Mass selectivity arises from combination of a_x and q_x values, referred as stability regions. Fig. 3.9 shows a quadrupole system simulated using SIMION (Scientific Instrument Services, Inc., USA) on mass filtering mode.

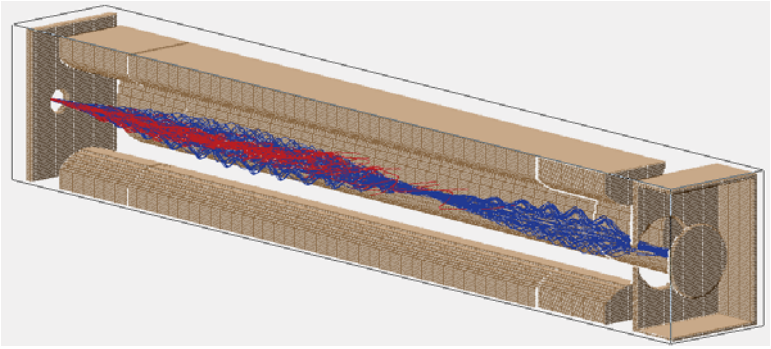

Figure 3.9: Simulation results of 120 ions of m/z=100 (in blue) and 120 ions of m/z=95 (in red) through a quadrupole filter. Parameters a_x and q_x (Eqs. 3.19 and 3.20) are chosen that only ions of 100 m/z are allowed through.

If no DC voltage is applied ($a_x = 0$), no filtering is performed by the quadrupole and it works as an ion guide (Fig 3.10).

Theoretical calculations (see Appendix B) indicate that a mass resolution ($\Delta M/M$, where ΔM is the width of the peak at the mass M) of 0.125 is attainable for standard quadrupole parameters. However, in practice, the resolution is close to unity.

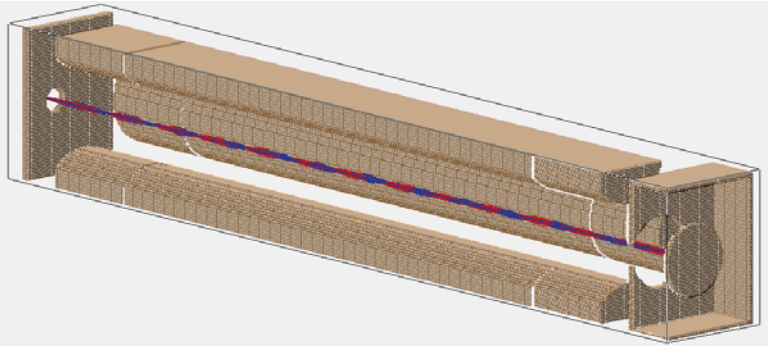

Figure 3.10: Simulation results of 120 ions of m/z=100 (in blue) and 120 ions of m/z=95 (in red) through a quadrupole filter. Parameter q_x is identical as simulation depicted in Fig. 3.9, however U=0 (Eq. 3.19, ion guide function).

3.4.2 Alternative mass analysers

Quadrupole filters represent many advantages within PTR-MS technology, namely: (i) high sensitivity, (ii) compact, (iii) operated under relative high pressure ($\sim 10^{-5}$ hPa, relative small pumps required). The downside of the system is its poor resolution, where isobaric compounds are not separated (e.g. acetone and propanal), and (potentially) poor duty cycle, consequence of filtering only one m/z while discarding the rest. The actual duty cycle depends on the amount of masses scanned.

In the following, three mass analysers that have replaced/complemented the quadrupole filter within the PTR-MS application are presented: the ion trap, the time-of-flight and gas chromatograph.

Ion Trap Systems

The ion trap is closely related to a quadrupole filter, however end caps will "trap" the ions within the volume of the quadrupole. Buffer gas, usually helium, is used to help trapping the ions and increase mass resolution (between 0.01 and unity). Once enough ions are trapped, they are ejected in a controlled manner by ramping the RF amplitude, and transferred to a detector, obtaining a mass spectrum. Because the ramp time can be very short relative to the accumulation time, a high duty cycle, in excess of 90%, is achievable.

Besides high duty cycle, the possibility to carry out tandem mass spectrometry (MS/MS) studies represents a large advantage. By application of tailored waveforms to the electrodes, all ions can be ejected from the trap except those of one particular mass. It is then possible to perform controlled fragmentation by increasing the kinetic

energy (collision-induced dissociation, CID) of the selected ions inside the trap to assist with additional species identification. This procedure has the potential to distinguish between isobaric molecules.

The first ion trap system in PTR-MS was reported in 2003 by Prazeller and co-workers [104]. This system consisted of a standard hollow-cathode discharge/drift tube arrangement that was interfaced to a commercial linear ion trap via an einzel lens. They were able to demonstrate the value of tandem MS/MS by successfully distinguishing between methyl vinylketone and methacrolein with their new ion trap system. However, the detection sensitivity was very poor, e.g. the limit of detection for benzene was 100 pbbV.

In 2005, Warneke and co-workers [105] presented a new PTR-MS with an ion trap detection system. With a strong sensitivity increase, this system had a detection sensitivity of benzene of 90 pptv for one-minute data accumulation. With same accumulation time, acetone could be measured up to 240 pptv. Despite relatively low sensitivity, its potential was demonstrated by using the different CID patterns of acetone and propanal to show unambiguously that the m/z=59 signal in air sampling experiments was predominantly due to acetone.

Mielke et al. have presented in 2008 [106] a modification of the quadrupole where it has been successfully adapted to a linear ion trap (Fig. 3.11). The instrument has a limit of detection of ∼100 pptv for Methyl vinyl ketone (MVK) and Methacrolein (MACR), enabling the distinction between these isobaric compounds in ambient measurements. The sensitivity is, nevertheless, orders of magnitude lower as state-of-art quadrupole PTR-MS systems.

Despite its clear advantages, use of ion traps as PTR-MS detection systems shows two disadvantages for trace gas measurements: (i) low sensitivity, and (ii) requirement of helium as buffer gas, which reduces the system portability due to addition of a pressurized bottle.

Time-of-Flight Systems

Another alternative to a quadrupole filter is the time-of-flight (TOF) mass analyser. In its most commonly used form, TOF mass spectrometry works by deflecting a batch of ions into a flight tube by an electric field and then separating them according to their flight times to a detector. Since the heavier ions travel more slowly than lighter ones, the time-of-flight spectrum can be converted into a mass spectrum.

A major advantage of TOF-MS over the previous described techniques consists

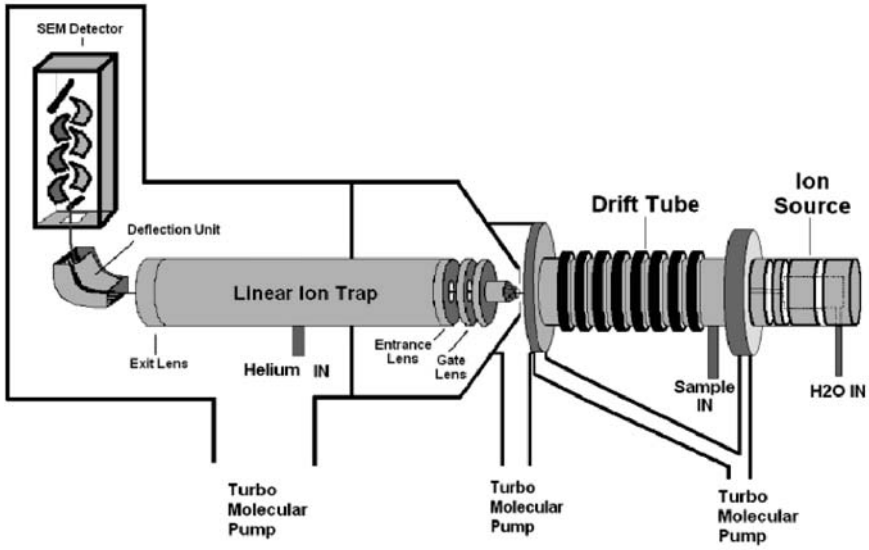

Figure 3.11: Schematic view of the proton transfer reaction linear ion trap mass spectrometer published by Mielke et al. [106]. Figure reproduced from the same reference.

of the attainable high resolution, which can be comfortably in excess of 0.001. In particular, a resolution better than $5E^{-4}$ opens up the possibility of distinguishing nominally isobaric compounds on the basis of accurate masses. For example, protonated methacrolein (m/z=71.0898) and 1-pentene (m/z=71.1329) can readily be distinguished with this resolution.

There are limitations due to the poor duty cycle of the standard TOF-MS technique. It originates from the orthogonal injection of a single pulse of ions into the flight tube from a continuous stream of incoming ions. Once these ions are in the flight tube, no further ions can be injected until the slowest ion has reached the detector. As a result, typically 1 or 2% of the ions entering the source region of the TOF-MS are deflected into the flight tube, which means that 98-99% of the potential ion signal available is, in effect, thrown away.

In 2004, Blake et al. [107] presented the first PTR-TOF-MS (Fig. 3.12). This instrument has been tested against gas standards and against other analytical techniques, and the limit of detection was estimated to be 10 ppbv for one-minute data accumulation, not high enough for trace gas measurements.

Ennis et al. published in 2005 a PTR-TOF-MS system which achieved limits of detection close to 1 ppbV in less than one minute [108] data accumulation. Two years later, Tanimoto and co-workers have constructed a system with detection sensitivities of <100 pptV for individual VOC components in one-minute integration time [109].

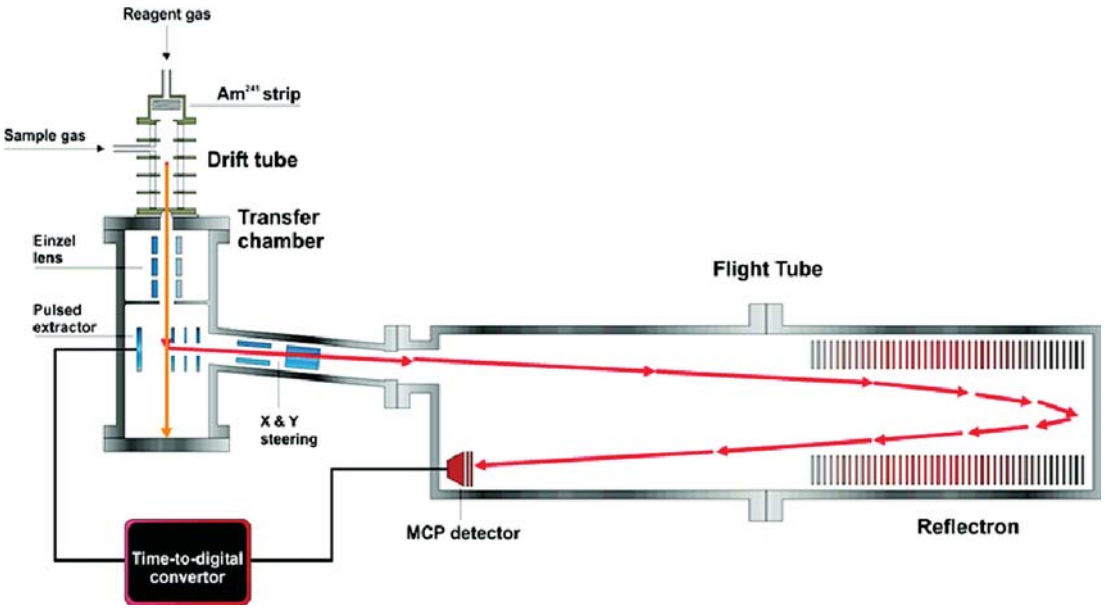

Figure 3.12: Schematic view of the proton transfer reaction time-of-flight mass spectrometer published by Blake et al. [107]. Figure reproduced from the same reference.

More recently Jordan et al. reported a PTR-TOF-MS [110] where sensitivity was improved to ∼15 cps ppbv^{-1}, with high resolution (<2E^{-4}). Such sensitivity yields a limit of detection of 600 pptv for 1 s measurement time and ∼80 pptv for 60 s integration time. Despite such achievement, state-of-the-art PTR-MS systems show roughly 2 orders of magnitude higher sensitivity.

Field (specially airborne) deployment of a PTR-TOF-MS faces some issues. Due to the requirement of a longer mean free path, the pressure in the reflectron must be much lower (10^{-7} hPa) in comparison with a quadrupole filter, requiring larger pumps. In addition, the reflectron itself is larger than the quadrupole system, resulting in a system 50 % heavier than the standard PTR-MS (∼170 kg compared to 120 kg). Moreover, stable environment (specially temperature) is crucial for the high mass resolution, condition hardly achievable in an aircraft.

Gas chromatography mass spectrometry

Gas chromatography (GC) is a method for separating complex mixtures. Separations are achieved by a series of partitions between a moving gas phase and a stationary (a liquid or polymer coating) held in a small diameter tube (the column) after a mixture is injected as a narrow band (Fig. 3.13). The gaseous compounds being analysed interact with the wall of the column causing each compound to elute at a different time, known

as the retention time of the compound. The different retention times is translated then into a compound separation.

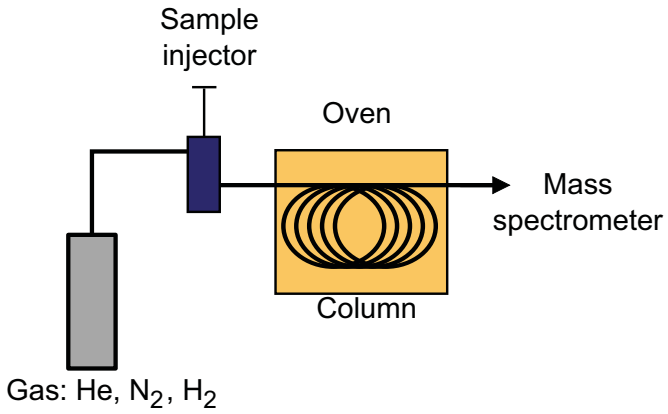

Figure 3.13: Schematic drawing of a gas chromatograph coupled with a mass spectrometer.

The specificity of PTR-MS has been studied by coupling a gas chromatographic column to the instrument. The column separates the isobaric VOCs in a sample prior to the injection into the PTR-MS. Karl et al. introduced the method [111] and it was further developed by Warneke, de Gouw et al. [35, 96], being applied in urban air measurements. The use of GC to separate compounds before injection in the PTR-MS has the advantage of separating isobaric compounds and allowing the study of sample specificity. This is achieved, however, at a great cost of increasing response time up to typically 30 minutes.

3.5 Reagent ions

Alternative proton donors to H_3O^+ were known in standard chemical ionization mass spectrometry long before the advent of PTR-MS [77]. In the PTR- MS, many alternative primary ions have been used, most notably $NH_4{}^+$[112], NO^+[113] and $O_2{}^+$[114]. Some of those reagent ions ionize as well through proton transfer (e.g. $NH_4{}^+$), in practice, shifting the minimum PA required for ionization to occur. Others, NO^+ for example, can ionize through several channels, mostly through charge transfer but as well by hydride ion transfer, or, depending on the reactor conditions, by termolecular association reaction [90].

Alternative reagent ions in PTR-MS have been mostly used for measuring: (i) compounds whose PA is lower that of H_2O, and (ii) compounds whose detection mass

overlaps with impurities from the ion source. 1,3-butadiene, an industrial chemical classified as possible carcinogen falls on the latter. Its detection mass is 55, the same as clustered primary $H_3O^+ \cdot (H_2O)_2$, which prevents low concentration measurements. However, Knighton et al.[113], using a HCD ion source fed with N_2, achieved the first real-time sub ppbv measurement of 1,3-butadiene. The ion source produced NO^+ with high purity, followed by charge transfer ionization reaction. For such reaction to be energetically allowed, the ionization energy (IE) of R must be higher than the IE of NO (see Table 3.3).

A similar problem is faced when measuring ammonia using H_3O^+. The HCD ion source produces typically large amounts of $NH_4{}^+$. It is presumed that NH_3 is generated in the plasma ion source from H_2O and N_2 (leaking from the drift tube into the ion source). Several attempts to reduce the $NH_4{}^+$ background failed and the lowest achievable background was equivalent to an ambient NH_3 mixing ratio of ∼100 ppbv.

Norman et al. [114] proposed the use of $O_2{}^+$ as primary and, equivalent as with NO^+, its ionization is mainly through charge transfer. Table 3.3 shows some compounds of interest and their mass of detection (if any) for $O_2{}^+$ and NO^+.

A commercially available PTR-MS with switchable ion source (H_3O^+, NO^+ and $O_2{}^+$) has been recently reported by Jordan et al.[84], increasing possibilities of applying different reagent ions in a routine basis. One disadvantage, however, is the requirement of high-pressurized cylinder of N_2 and of O_2 for producing NO^+ and $O_2{}^+$, respectively.

Despite the listed benefits of using different reagent ions, in practice, it still considered minimal compared to the use of H_3O^+ as proton sources, which explains why H_3O^+ is overwhelmingly the reagent of choice in PTR-MS work to date.

3.6 Calibration and background noise analysis

An important aim of many applications of PTR-MS is to determine the absolute mixing ratios of a variety of trace VOCs. In principle, according to reaction kinetics, knowledge of reaction time t, rate coefficient κ and the measured quantity of $[RH^+]$ and $[H_3O^+]$ would suffice to determine [R] as such:

$$[R] = \frac{[RH^+]}{[H_3O^+] \cdot \kappa \cdot t} \tag{3.21}$$

Table 3.3: Ionization energy and mass of detection (if any) of some compounds found in the air using NO^+ or $O_2{}^+$ as primary ion. *Ionization energy obtained from NIST Chemistry WebBook.*

Compound	Formula	Ioniz. energy (eV)	Detection mass (amu)
NO^+ or $O_2{}^+$			
Styrene	C_8H_8	8.46	104
Dimethyl sulphide	CH_3SCH_3	8.69	62
Toluene	C_7H_8	8.83	92
Isoprene	C_5H_8	8.86	68
1,2-butadiene	C_4H_6	9.03	54
1,3-butadiene	C_4H_6	9.07	54
Chlorobenzene	C_6H_5Cl	9.07	112
Benzene	C_6H_6	9.24	78
Nitric oxide	NO	9.26	30
$O_2{}^+$			
Nitrous oxide	NO_2	9.59	44
Acetone	CH_3COCH_3	9.70	58
Propanal	C_2H_5COH	9.96	58
Ammonia	NH_3	10.07	17
1-butyne	C_4H_6	10.18	54
Acetaldehyde	CH_3CHO	10.23	44
Methanol	CH_3OH	10.84	32
Formaldehyde	CH_2O	10.88	30
Formic acid	HCOOH	11.33	46
Oxygen	O_2	12.07	32
Not detected			
Acetonitrile	CH_3CN	12.20	-
Ozone	O_3	12.53	-
Methane	CH_4	12.61	-
Water	H_2O	12.62	-
Carbon dioxide	CO_2	13.77	-
Carbon monoxide	CO	14.01	-
Nitrogen	N_2	15.58	-

The bottom line is that, for accurate mixing ratio determination, calibration of the instrument against specific gas standards is essential. After extensive system characterization, de Gouw and co-workers have reached a conclusion where the maximum PTR-MS accuracy is in the region of 25%, with the aid of suitable calibration [96]. Improvements beyond this are difficult to achieve because of background signals from various impurities in the ion source and drift tube. The precision improves as the concentration increases but is rarely better than 10-15%.

As previously discussed (Section 3.3), the mixing ratio determination can be affected by humidity. The humidity effect derives from the change in the amount of water clustered primary ions, $H_3O^+(H_2O)_n$, depending on the humidity of the analyte gas. Many compounds will have a different reaction rates with water clustered primary ions when compared to reaction with H_3O^+, while some will not react at all.

An example of humidity effect has been published by de Gouw et al. [29]. With increase of relative humidity, sensitivity for acetone is not strongly affected, given it is ionized from both primary ion and its clustered version. Toluene, on the other hand, is not ionized by clustered primary ion (Fig. 3.14), therefore its sensitivity is strongly humidity dependent. A correction factor is proposed based on the relative signal of clustered primary ion but its application is limited.

As previously discussed, spurious counts in the PTR-MS can have several sources: ion source impurities, ion clustering and photons originated in the ion source. Outgassing of material, contamination and leakage will introduce uncertainties in the compound's volume mixing ratio. Therefore, besides performing regular calibration, background check is essential for accurate measurement.

The most commonly used technique is having inlet air though a platinum wool catalyst heated at 350 °C, that efficiently removes VOCs from the inlet flow. Volume mixing ratios are determined from the difference between the count rate of ions detected with the catalyst off ($I_{cc=off}$) and with the catalyst on ($I_{cc=on}$).

$$\mathrm{VMR} = \frac{1}{I_{H_3O^+} \times S}(I_{cc=off} - I_{cc=on}) \tag{3.22}$$

where $I_{H_3O^+}$ is the count rate of primary ions (in units of 10^6 counts s^{-1}, it might include clustered ions, depending on the compound analysed) and S the calibration factor (in ncps/ppbv). From Eq. 3.22, the error in the VMR, ΔVMR, can be estimated,

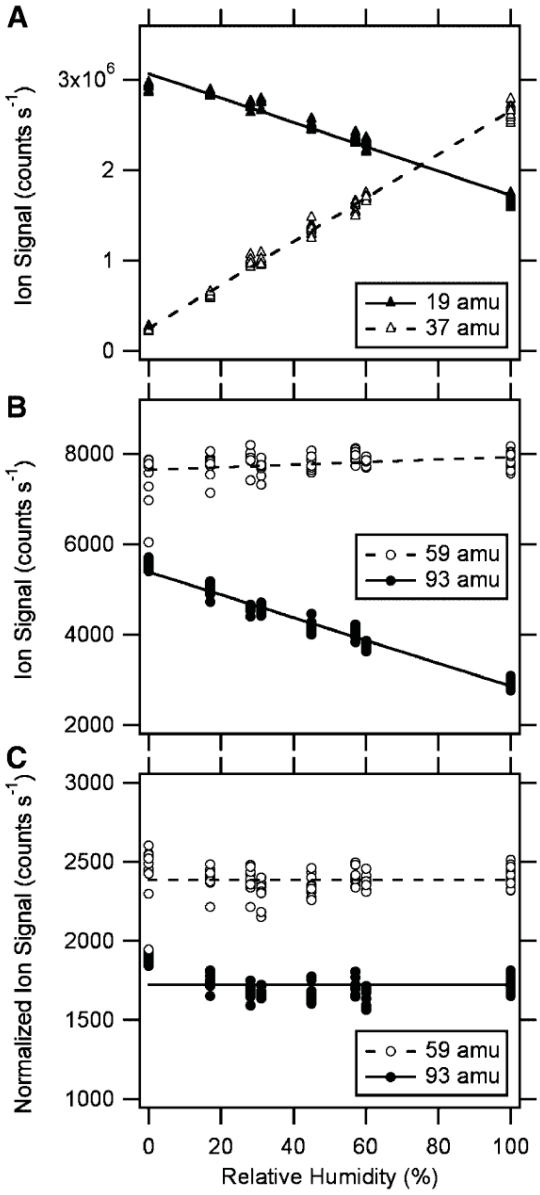

Figure 3.14: Influence of humidity on sensitivity published by de Gouw et al. [29]. Results obtained at 298 K and 120 Td. A:Ion signal of primary ion (H_3O^+, mass 19) and water clustered primary ion ($H_3O^+.(H_2O)$, mass 37). B: Signal of acetone at 59 amu and toluene at 93 amu. C: Normalized signal of acetone at 59 amu and toluene at 93 amu by a proportionality factor to clustered primary ion.

assuming that it is dominated by the statistical errors in ($I_{cc=off}$) and ($I_{cc=on}$) [115].

$$\Delta\text{VMR} = \frac{1}{I_{H_3O^+} \times S}\sqrt{\frac{I_{cc=off}}{\tau_{cc=off}} + \frac{I_{cc=on}}{\tau_{cc=on}}} \tag{3.23}$$

where $\tau_{cc=off}$ and $\tau_{cc=on}$ are the dwell times (in seconds) with the catalyst on and off (not necessarily the same). Equation 3.23 shows that (i) increasing the primary ion signal, (ii) increasing the calibration factor S (e.g. longer drift time), and (iii) increasing the dwell times will all improve the precision of a measurement.

The calibration factor S and the signal with the catalyst on $I_{cc=on}$ are usually only obtained through calibration cycles, since its own measurement prevents outside air to be measured. Between calibration cycles, interpolation of S and ($I_{cc=on}$) is made. The assumptions that $I_{cc=off}$ and $I_{cc=on}$ dominates the statistical errors can be flawed, since a fast humidity change, for example, may change S strongly, increasing measurement error.

Chapter 4 describes a newly developed calibration source. By using isotopically labelled compounds, on-line calibration can be performed, thus increasing measurement accuracy and duty cycle.

3.7 PTR-MS application on atmospheric chemistry

As discussed in Chapter 2, VOCs are important in the atmosphere due to their impact on photochemical ozone formation, particulate formation, stratospheric ozone depletion and climate. Many VOCs are also toxic and/or carcinogenic, therefore their concentration monitoring in a wide range of environments is vital for establishing their effect on human health.

Measurements of VOCs in the atmosphere have largely been made using gas chromatographic analyses of air samples that were either collected in canisters, on adsorbents or in cryostats. Such technique provides highly detailed snapshots (tens of VOCs with volume mixing ration down to 0.1 pptv) of the atmospheric VOC composition, but are generally too slow to follow rapid changes in air mass composition.

The PTR-MS capability as a real time, highly sensitive monitoring tool for a whole range of VOCs has been extensively applied in the past decade on a range of atmospheric-measurement platforms including ground-based measurement stations [13, 116–120], vehicle [121], train [122], ships [48, 101, 115, 123, 124], tethered balloon [125], research aircraft [14, 61, 126, 127] and operational aircraft [34]. Table 3.4 provides

a list of published VOCs measured in ambient air by the PTR-MS.

Research aircraft campaigns have been carried out in several locations such as Surinam[128], Indian ocean[33, 129], Mediterranean sea[130, 131], Eastern pacific[132], West Africa [127], and Amazonian rainforest [61, 126]. Different air masses have being analized for its VOC contents, such as clean marine air, pollution plumes from large cities, biomass burning and tropical rainforest biogenic VOCs emissions.

Operational aircraft deployment is carried out within the CARIBIC project[36]. A PTR-MS, along with many other instruments, measures regularly (four flights per month) in the upper troposphere and lowermost stratosphere (9-12 km) between Germany and a number of alternating destinations, including South America, North America, South Asia, and East Asia, providing valuable data along with seasonal variability [34]. In Chapter 7, CARIBIC project is further described, where acetone and carbon monoxide correlation results in the upper troposphere are presented.

Table 3.4: Published identifications of masses detected by PTR-MS in ambient air.

Detection mass (amu)	Compound	Formula	Reference
17	Ammonia[a]	NH_3	[114]
28	Hydrogen cyanide	HCN	[133]
31	Formaldehyde	CH_2O	[134–136]
33	Methanol	CH_3OH	[55, 115, 137]
42	Acetonitrile	CH_3CN	[33, 55, 115]
45	Acetaldehyde	CH_3CHO	[117, 138, 139]
47	Formic acid	HCOOH	[140]
47	Ethanol	C_2H_5OH	[14, 117]
54	Acrylonitrile	CH_2CHCN	[133]
55	1,3-Butadiene	C_4H_6	[113]
59	Acetone	CH_3COCH_3	[34, 124, 127]
59	Propanal	C_2H_5COH	[14, 141]
61	Acetic acid	CH_3COOH	[14, 139]
63	Dimethyl sulfide	CH_3SCH_3	[124]

continued on next page

continued from previous page

Detection mass	Compound	Formula	Reference
69	Isoprene	C_5H_8	[117, 122, 127]
69	Furan	C_4H_4O	[122]
71	Methacrolein (MACR)	H_2CCCH_3CHO	[106, 122]
71	Methyl vinyl ketone (MVK)	$CH_3COCHCH_2$	[106, 122, 127]
73	Methyl ethyl ketone (MEK)	$CH_3COCH_2CH_3$	[138, 139]
75	Hydroxy acetone	CH_3COCH_2OH	[140]
77	Peroxyacetyl nitrate (PAN)[b]	$CH_3C(O)O_2NO_2$	[142]
79	Benzene	C_6H_6	[117, 127]
81	Monoterpenes[b]	$C_{10}H_{16}$	[29]
81	(Z)-3-hexenal[b]	$C_6H_{10}O$	[140, 143]
83	(Z)-3-hexenol[b]	$C_6H_{11}OH$	[140, 143]
83	Methyl furan	C_5H_6O	[143]
85	Ethyl vinyl ketone	$C_2H_5COCHCH_2$	[143]
91	Peroxypropionyl nitrate (PPN)[b]	$C_2H_5C(O)O_2NO_2$	[142]
93	Toluene	$C_6H_5CH_3$	[117, 139]
103	Peroxymethacryloyl nitrate (MPAN)[b]	$CH_2C(CH_3)C(O)O_2NO_2$	[142]
105	Styrene	$C_6H_5CHCH_2$	[29]
107	C_8-aromatics	C_8H_{10}	[29]
115	Heptanal	$C_7H_{14}O$	[143]
137	Monoterpenes	$C_{10}H_{16}$	[29]
151	Pinonaldehyde	$HOC_{10}H_{15}O$	[144]

[a] O_2^+ as primary.

[b] Component fragmented.

3.8 Conclusion

The PTR-MS system is capable of performing real-time measurement of many VOCs with high sensitivity. Being a relatively portable system (120 kg), the PTR-MS has been deployed in many different platforms including ground-based stations, ships, and

aircraft, gathering valuable data. The description of the "standard" system, i.e. the design proposed by Lindinger et al. and of alternative designs published up-to-date provides a broad overview of the PTR-MS technology. Such overview serves as a base for the following instrumental Chapters where the unheated calibration source, the ion funnel enhanced drift tube and the novel PTR-IF-MS are described.

Chapter 4

An unheated permeation device for calibrating atmospheric VOC measurements

Volatile organic compounds (VOCs) such as carbonyls, alcohols, organic nitrates, organic pernitrates and peroxides are extremely relevant for the chemical processing in the atmosphere (see Chapter 2). Reliable analytical tools for their accurate measurement in the atmosphere are a prerequisite for a better quantitative understanding of the controlling processes. That is, an accurate and reliable calibration system is an essential requirement for state-of-the-art instruments.

This Chapter describes a new permeation-based calibration system for airborne applications. The system is integrated into the newly developed Proton-Transfer-Reaction mass spectrometer (PTR-MS) described in Chapter 6. In combination of a fast-stabilizing membrane with a slow changing temperature, we have devised a calibration system that has the portability and robustness of regular permeation sources, without the requirement for temperature stabilization prior its use. As such, the permeation rate is solely a function of the (uncontrolled) temperature that can be accurately measured.

4.1 Calibration devices for VOC measurements

Calibration systems for in-situ instruments rely either on static or dynamical methods [145]. Static methods are based on mixtures of calibration gases stored in closed housings. Nowadays, the most used static method for calibration are high-pressurized

gas cylinders with previous wall treatment [146–148]. Despite the robustness of the technique and the large number of considered species, these systems are bulky and may suffer, in particular after long storage times, from possible adsorption and chemical reactions of the analyte on the cylinder wall [149].

In dynamical methods a continuous flow of the relevant analyte is diluted into a carrier gas stream. Dynamical methods most commonly used are, but not limited to, mixing of gas streams, diffusion methods, capillary injection, syringe injection and permeation devices [145, 150]. Diffusion methods and permeation devices are extensively used for the calibration of instruments measuring VOCs in low concentrations, i.e. in the ppbv (ppbv = 10^{-9} mol/mol) range [151–156].

A crucial requirement for accurate and reliable atmospheric in-situ VOC measurements is the generation of known and reproducible gaseous standards at typical ambient mixing ratios. These gaseous standards are essential for calibrating and characterizing either sampling methods, multistep analytical procedures, or online instruments. An overview of calibration devices is given by Barratt [149] and Naganowska-Nowak et al. [157]. Below, the two most widely used calibration standard generation techniques for VOC in-situ measurements are described, i.e. calibration gas cylinders and permeation devices.

4.1.1 Calibration gas cylinders

Certified gas standards are produced by making use of calibrated syringes. The analyte filled in the syringe is injected into a flow of zero air which runs into a previously evacuated cylinder. Once the syringe is emptied, the cylinder is filled with a diluent (e.g. synthetic air), and the amount of syringe and the pressure will define the analyte concentration [149, 150].

With usually several compounds of interest in the same gas cylinder, pressurized cylinders are extensively used as in-situ calibration source in ground-based studies [158–160] as well as during airborne VOC measurements [34, 126, 129]. Uncertainties of concentration in the bottle ranges usually between 5% and 15% depending on compound and preparation method [148, 161, 162]. As the VOC concentrations in the cylinder are typically around $\sim$1 ppmv (ppmv = 10^{-6} mol/mol), further uncertainty may be generated owing to dilution to the desired concentrations, which is mostly done using mass flow controllers, pressure controllers, and/or critical orifices.

4.1.2 Permeation devices

Permeation methods have been developed in the 1960s [163] as standard for trace gas analysis and have been used extensively since. Permeation devices usually comprise a short polymer tube filled with the analyte of interest sealed at both ends by glass plugs. The analyte vapour dissolutes into the polymer, diffuses through its wall and mixes into the sample gas stream. The permeation rate (amount of analyte per unit of time) is usually strongly dependent on temperature. Thus, in order to maintain quantified and constant permeation rates, permeation devices are kept in temperature controlled conditions before and during their use. Note that the time until a permeation device reaches an equilibrated state, the so-called stabilization time, typically ranges from hours to days [151].

For atmospheric in-situ measurements onboard aircraft, permeation devices have several advantages over high-pressurized gas cylinders such as light weight, small volume, and the easiness to meet safety clearance, due to the lack of overpressure and the use of only very small amounts of chemicals. However, power loss during transport to the aircraft or before take off due to fuelling can push the permeation system from equilibrium and thus prevent accurate calibration until such equilibrium is once again reached.

As previously outlined, the permeation rate is strongly dependent on temperature, because of which permeation devices are usually permanently temperature controlled. A common rule of thumb states that for every degree Celsius of temperature increase, the permeation rate increases by 10 % [164]. Such relationship arises from the assumption that the permeation rate (P) shows an Arrhenius-like behaviour [153, 165, 166]:

$$P = P_0 \cdot \exp\left(\frac{-E}{R \cdot T}\right) \tag{4.1}$$

where P_0 is a constant usually having the unit of $\mathrm{ng\,s^{-1}}$, E the activation energy, R the gas constant and T the absolute temperature.

Given the new approach of unheated permeation devices presented here, a deeper insight in the transport of gases through polymers is required. In the following, permeation through polymers is shortly discussed, allowing a later comparison with instrumental results.

4.2 Gas transport through polymers

As initially described by Graham, the transport of small molecules through a polymer membrane occurs due to random molecular motion of individual molecules [167]. The driving force behind the transport is the concentration difference across the polymer membrane.

At steady state, this transport can be described in terms of Fick's first law of diffusion, according to which the flux J (in direction of the concentration gradient) is proportional to the concentration gradient $\partial c/\partial x$ and the diffusion coefficient D (unit: $\mathrm{m^2\,s^{-1}}$):

$$J = -D \cdot \frac{\partial c}{\partial x} \tag{4.2}$$

and in the integrated form:

$$J = D \cdot \frac{(c_2 - c_1)}{l} \tag{4.3}$$

with l the membrane thickness, and c_1, c_2 the concentrations below and above the membrane. In an ideal case, the analyte concentration c dissolved in the polymer will be given according to Henry's law:

$$c = S \cdot p \tag{4.4}$$

with S the solubility and p the pressure. Combining equation 4.3 with 4.4 gives the well-known permeation equation [168]:

$$J = D \cdot S \cdot \frac{(p_2 - p_1)}{l} \tag{4.5}$$

where p_1 and p_2 are the ambient partial pressures on the two sides of the membrane. The product $D \cdot S$ is intrinsic to the membrane material and is defined as the permeability coefficient B:

$$J = B \cdot \frac{(p_2 - p_1)}{l} \tag{4.6}$$

This approach, usually known as solution diffusion model [169, 170], only works for special membrane materials, namely homogeneous non-porous polymers. However, polymers typically used in permeation devices (see below) are porous. Here adsorption in the polymer and hopping of molecules from pore to pore occurs as well. Indeed, on porous polymers, molecule hopping usually largely dominates over permeation due to solution-diffusion transport.

The most prominent polymer used in permeation devices is polytetrafluoroethylene

(PTFE). PTFE is a porous semicrystalline material [171–173], i.e., it is formed of amorphous and crystalline regions. Already 50 years ago, it was shown that the sorption and diffusion in semicrystalline polymers take place exclusively in the amorphous regions [174–176]. The crystalline zones however act as impermeable barriers for diffusion.

To describe the transport in porous materials, the gas transport is parameterized either as viscous (or Poiseuille) flow or/and as Knudsen flow [177, 178], see Figure 4.1.

What flow regime is applicable to the actual material depends on the ratio between its pore diameter d and the mean free path of the gas molecule in the pores λ, called Knudsen number:

$$K_n = \frac{\lambda}{d} \tag{4.7}$$

For $K_n \gg 1$ (small pores), Knudsen flow dominates where the number of molecule-wall collisions exceed the one of intermolecular collisions. For $K_n \ll 1$ (large pores), permeation follows a viscous flow where intermolecular collisions dominate. For $K_n \sim 1$, the so-called transition flow applies where a combination of both regimes occurs.

According to [179], λ can be approximated to:

$$\lambda = \frac{\kappa \cdot T}{\sqrt{2}\pi \cdot p \cdot d_m^2} \tag{4.8}$$

being κ, T, p, and d_m the Boltzmann constant, absolute temperature, pressure, and the diameter of the gas molecule, respectively.

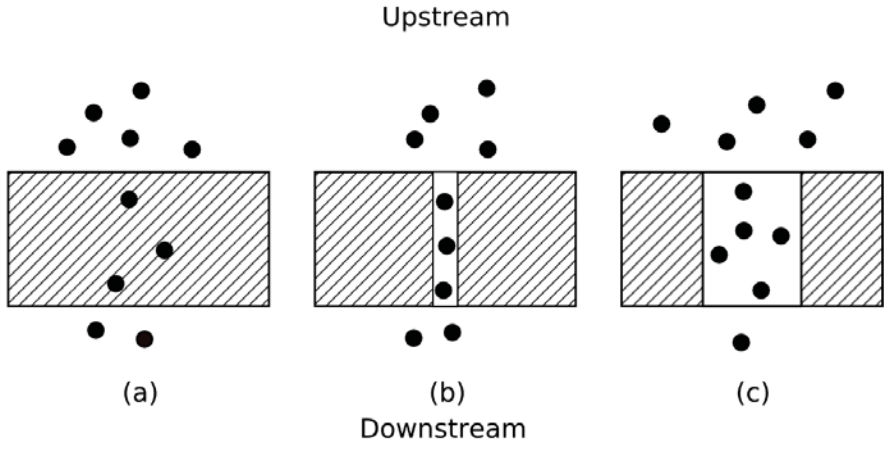

Figure 4.1: Permeation mechanisms: (a) solution-diffusion based on Fick's law (eq. 4.2), (b) Knudsen flow prevailing at small pores, (c) viscous or Poiseuille flow occurring at large pores.

In the following the basic equations describing Knudsen flow and viscous flow are

outlined, based on a review by Rutherford and Do [177] and Choi et al. [178]. The objective is to describe the prominent temperature dependence of both flow regimes and finally compare our experimental results with the theory.

4.2.1 Knudsen flow

In Knudsen diffusion the pore sizes are small ($K_n \gg 1$). In this case, the analyte flow depends on the concentration difference and hence on the partial vapour pressure difference. In practice, where the permeation device is flushed by an analyte-free carrier, the diffusion coefficient depends only on the vapour pressure p_v of the analyte within the permeation device. The diffusion constant for Knudsen flow is [177]:

$$D_K = \frac{d_m}{3}\sqrt{\frac{8 \cdot R \cdot T}{\pi M}} \tag{4.9}$$

where M is the molecular weight. The steady state flow is described as [178]:

$$J_K = D_K \cdot \frac{\epsilon \cdot p_v}{\tau \cdot R \cdot T \cdot l} \tag{4.10}$$

where ϵ is the porosity, p_v the analyte vapour pressure, and τ the tortuosity factor [180].

Most of the parameters in equations 4.9 and 4.10 are material constants, parameters, or physical constants. Therefore, combining those (temperature independent) parameters to a given constant J_K^0, it becomes evident that Knudsen flow has the following temperature dependence:

$$J_K = J_K^0 \cdot \frac{p_v(T)}{\sqrt{T}} \tag{4.11}$$

with

$$J_K^0 = \frac{d_m \cdot \epsilon}{3\tau \cdot l}\sqrt{\frac{8}{\pi \cdot M \cdot R}} \tag{4.12}$$

4.2.2 Viscous flow

If the pore sizes are large ($K_n \ll 1$), the number of intermolecular collisions dominate and the flow is governed by viscous flow in the gaseous phase. Such transport is driven by the total pressure gradient (different to Knudsen flow). The diffusion coefficient is defined as [177]:

$$D_V = \frac{d_m^2 \cdot \bar{p}}{32\mu} \tag{4.13}$$

where μ is the gas viscosity and $\bar{p}$ the mean pressure (see below). At steady state the flux is [178]:

$$J_V = \frac{D_V \cdot \epsilon}{\tau \cdot R \cdot T \cdot l} \Delta p \tag{4.14}$$

where Δp is the pressure difference below/above the membrane or inside/outside the permeation device. Therefore Δp can be written as $\Delta p = p_v - p_{\text{air}}$ and $\bar{p} = (p_v + p_{\text{air}})/2$, with p_{air} as the total pressure in the carrier gas.

The gas viscosity μ shows the following temperature dependence:

$$\mu = \mu_0(T_0) \cdot \frac{T_0 + C_S}{T + C_S} \cdot \left(\frac{T}{T_0}\right)^{3/2} \tag{4.15}$$

with $\mu_0(T_0)$ the gas viscosity at the reference temperature $T_0 = 298\,\text{K}$ and C_S the Sutherland's constant. Considering that C_S of acetone is 542 K[181], around room temperature μ roughly scales with $T^{3/2}$. Therefore, the viscous flow can be rewritten as:

$$J_V = J_V^0 \cdot \frac{(p_v(T) + p_{\text{air}}) \cdot (p_v(T) - p_{\text{air}})}{(T/T_0)^{5/2}} \tag{4.16}$$

with

$$J_V^0 = \frac{d_m^2 \cdot \epsilon}{16\mu_0(T_0) \cdot \tau \cdot R \cdot l} \tag{4.17}$$

4.2.3 The stabilization time

As outlined in the introduction, one drawback of permeation sources used during field measurements is the long stabilization time, i.e. the time lag between the stabilization of temperature and permeation rate. According to [177], this stabilization time for Knudsen and viscous regime, θ_K and θ_V, are:

$$\theta_K = \frac{l^2}{6D_K} \tag{4.18}$$

and

$$\theta_V = \frac{l^2}{3D_V} \tag{4.19}$$

Being the reduction of the stabilization time one of the goals of this new calibration source, equations 4.18 and 4.19 were taken in account during the system development. More is discussed in the next Section.

4.2.4 The permeation mechanism through PTFE

As previously discussed, PTFE is widely used as permeating membrane in calibration sources. In PTFE, pore sizes between 0.3 and 0.7 μm have been measured [171], although a broad distribution of pore sizes is expected. The mean free path at room temperature and 500 hPa is $\sim 0.05\,\mu$m for acetone (calculated using Eq. 4.8), therefore, $K_n \approx 6 - 14$. With such value of K_n, the permeation is expected to be dominated by the viscous regime, nevertheless, due to large distribution of pore sizes, transition flow may play an important role.

Unfortunately, to our knowledge no consensus has been found on how to combine Knudsen transport and viscous transport in the transition regime [178, 182]. Moreover, hysteresis effects can occur in systems where adsorbed molecules are strongly bound in the polymer, a process that is not expected in PTFE [183]. In the next Section, experimental results are compared with flow regimes described previously.

4.3 The unheated permeation device

As outlined in the introduction, permeation sources are usually controlled to a defined temperature to which the permeation rate is well defined. However, the usually long stabilization time associated with permeation through polymers prevents the use of the calibration source for many hours after the temperature is controlled. In aircraft applications, lack of power prior to take-off (e.g. during aircraft fuelling) can lead to temperature change, and thus the lost of valuable data during flight.

Here, we detail an unheated permeation device, i.e. its temperature and thus permeation rate floats in dependence of the temperature gradient between outside and inside the device. The possible pressure dependence of the permeation rate (see Eq. 4.16) can be discarded considering that downstream of the membrane (i.e. the carrier gas) is always kept at a constant pressure.

The only way to accurately derive the permeation rate is to guarantee that the influence of the temperature change (and thus stabilization time) is minimal. This can be achieved by strongly reducing the temperature drift of the system dT/dt. Such condition is achieved due to the following two technical features of the presented permeation system: (i) by using a thin membrane (having a surface of only some mm^2) instead of the usually applied much larger permeation tubes with significantly larger wall thickness. Such a membrane strongly reduces the stabilization time θ (Eqs. 4.18 and 4.19). (ii) Strongly reducing the temperature drift of the system by a combination

of an extremely efficient insulation and a large heat capacity of the system. The design of the system, taking in account points (i) and (ii), is presented in the following.

4.3.1 Description of the new calibration source

The calibration source consists of a stainless-steel (SS) cube filled with ∼0.7 l water which has (after ammonia) the largest specific heat capacity c_v of 4.2 kJ/(kg K) of any substance. Five recipients (filled with up to five different analytes and sealed with PTFE membranes) are immersed into the water bath and thus have exactly the same temperature as the SS cube and the water bath. Fig. 4.2 is a schematic drawing of the presented calibration source.

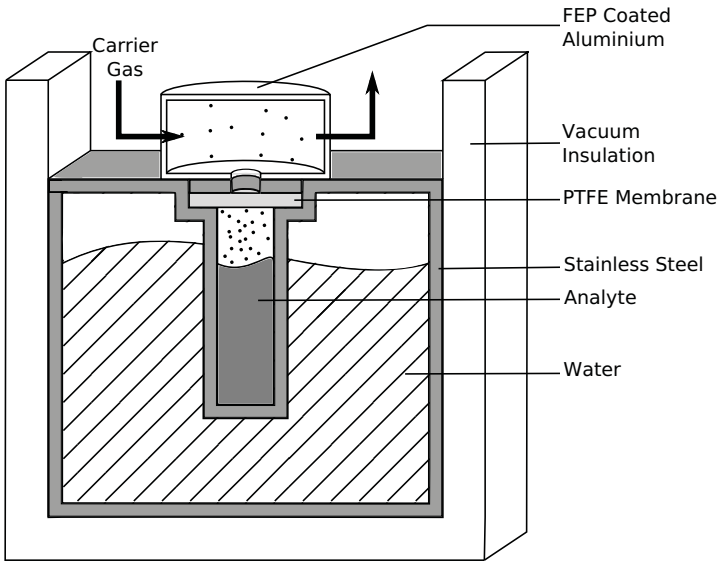

Figure 4.2: Schematic view of the calibration system. Five 0.35 ml cylindrical recipients (here, only one is shown) filled with different liquid analytes are surrounded by a water bath. The 0.4 mm thick PTFE membrane works as permeating polymer and provides sealing for the liquid analyte. The "active" area, through which permeation occurs, is 6 mm^2. A fluorinated ethylene propylene (FEP) coated aluminium cap sealed with viton O-rings encloses the five permeation membranes. Sample gas enters and leaves the system via perfluoroalkoxy (PFA) fittings located in the cap.

The entire system is enclosed with six 4 cm thick vacuum insulation bricks (va-Q-tec, Germany) that have an extremely low thermal conductivity of less than 0.005 W/(m K), corresponding to an insulation of 30 - 40 cm with typical insulation foam.

The presented calibration source is filled with isotopically labelled acetone, namely D-6 acetone (Aldrich Chemical Co., USA) having a mass of 64 amu, in contrast to nat-

ural (atmospheric) acetone with mass 58 amu. This isotope labelling of the calibration gas is an often applied technique in mass spectrometry. In this case the calibration gas can permanently be added to the sample flow. Besides negligible isotope fractionation effects, it behaves chemically identical as the gas in the sample gas, but is detected at another mass [184, 185]. Moreover, it allows higher measurement accuracy due to the (almost) continuous calibration (in contrast to performing calibration cycles). This advantage is of particular importance during aircraft observations where the air mass composition and thus parameters affecting the instrument sensitivity (e.g. humidity) may change quickly.

When the instrument is turned off, a venting system was developed to avoid contamination of the FEP-coated aluminium cap (Fig. 4.2) and the inlet and outlet line of the calibration device. The venting system consists of a micro diaphragm pump (Gardner Denver Thomas, USA) that only consumes ∼35 mW at a flow of 150 sccm (standard cubic centimetre per minute). It is powered by two extremely high-power goldcap capacitors each storing a capacity of 1500 Farad at 2.5 V (BOOSTCAP, Maxwell Technologies, USA). An extremely small electronic circuit switches the micro pump on and off for 20 s each. The energy stored by the goldcaps of 2.6 Wh is sufficient to power the pump for about ten days and thus easily bridges possible transportation time to and from the airport or times in the laboratory when the system is switched off.

The entire calibration system, along with the venting system, weights less than 3 kg.

4.3.2 Assessing the temperature drift

A key parameter of the unheated permeation device is the temperature drift dT/dt, which influences directly the permeation rate estimation. The heat flow into the system P is due to two heat sources: (i) heat transport across the insulation P_{ins} and (ii) heating/cooling due to the inflowing sample air P_{air}:

$$Pow = P_{ins} + P_{air} \tag{4.20}$$

P_{ins} is the product of the heat conductance of the vacuum insulation box given by the manufacturer of $U_{ins} = 0.015$ W/K and the temperature gradient across the insulation ΔT. P_{air} is the product of the heat capacity of the inflowing sample air $c_{v,air}$, its flow through the device j_{air} and the temperature gradient between the inflowing sample air and the inner temperature, again ΔT:

$$Pow = U \cdot \Delta T + c_{v,\,air} \cdot j_{air} \cdot \Delta T \tag{4.21}$$

This heating power Pow results in a temperature drift of the device dT/dt which is solely determined by the heat capacity of the device:

$$\begin{aligned} Pow &= dQ/dT \\ &= C_v \cdot dT/dt \end{aligned} \tag{4.22}$$

The heat capacity of the device C_v is the sum of the heat capacity of the water and the stainless steel (SS):

$$\begin{aligned} C_v &= 0.7\text{kg} \cdot 4.2\text{kJ/(kg K)} + 0.6\text{kg} \cdot 0.5\text{kJ/(kg K)} \\ &= 3.24\text{kJ/K} \end{aligned} \tag{4.23}$$

Combing Eqs. 4.21, 4.22, and 4.23, resolving it to dT/dt, and inserting all physical constants ($c_{v,\,air} = 28.97$ J/(mol K)) and parameters ($j_{air} = 35\,\text{sccm} = 1.4\,\text{mmol/min}$), leads to:

$$\begin{aligned} dT/dt &= (U + c_{v,\,air} \cdot j_{air}) \cdot \Delta T/C_v \\ &= 17\text{mK/h} \cdot \Delta T \quad (\Delta T \text{ in K}) \end{aligned} \tag{4.24}$$

Therefore, even at an extreme temperature gradient between inside and outside of ΔT = 20 K, results in a temperature drift of only ∼340 mK/h.

4.4 Experimental results

The results depicted in this Section have been obtained according to the experimental setup shown in Fig. 4.3. The system was calibrated once each 100 minutes, using natural acetone from a gas cylinder for 10 minutes. The background signal was measured for another 10 min by guiding the sample air through the VOC-scrubber.

4.4.1 Determination of the stabilization time

Firstly, the stabilization time θ of the calibration source was measured. For this test, the insulation around the calibration device was removed and, using a heating wire wrapped around the device, its temperature was controlled to 43 °C. To guarantee system stabilization the calibration source was kept at this temperature for some hours. Thereafter, the temperature control was switched to 30 °C, leading to a "fast" temperature change (-7 K/h). Once the desired temperature was reached, a further 16 hours measurement was carried out for stability test. The time difference between the system

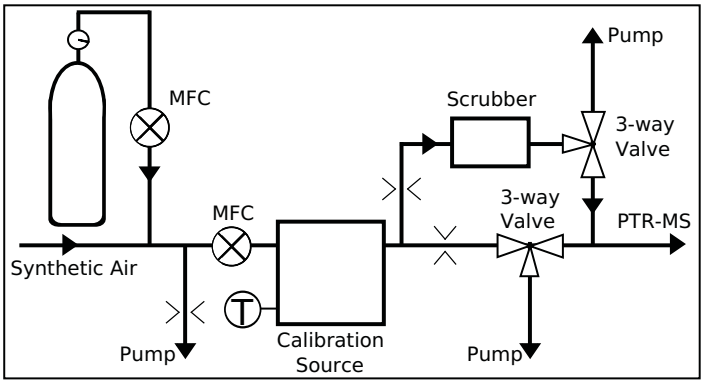

Figure 4.3: Sketch of the experimental setup. On the left side, sample air having a well-defined mixing ratio of acetone is generated. For that, air from a cylinder filled with standard gas (Apel-Reimer Environmental, USA) having an acetone mixing ratio of 500 ppbv is mixed with synthetic air. Two mass flow controllers (MFC) lead to a sample gas flow of 35 sccm with an acetone mixing ratio of ∼16.1 ppbv. This air flow is guided through the calibration gas source filled with isotopically labelled acetone, referred as D6-acetone. Thereafter, the air goes either directly into the PTR-MS or before through a VOC scrubber (Pt-catalyst controlled to 350 °C) for measuring the background signal.

reaching 30 °C and the stabilization of the permeation rate is the stabilization time, as seen in Fig. 4.4.

After temperature stabilization (at ∼120 min), it took ∼18 min for the permeation rate to stabilize. The stabilization time can be compared with permeation due to Knudsen and viscous flow (Eqs. 4.18 and 4.19), using the parameters depicted in Table 4.1.

Table 4.1: Calibration source parameters for stabilization time calculation.

Parameter	Value	Unit
Membrane thickness l	0.4	mm
Mean temperature T	309	K
Diameter acetone molecule d_m	0.63	nm
molecular weight of D6-acetone M	64.1	$\mathrm{g\,mol^{-1}}$
Gas viscosity μ	7.9	$\mu\mathrm{Pa\,s}$
Vapour pressure of acetone p_v	467.7	hPa
Air pressure p_{air}	40	hPa

The stabilization time calculated for the Knudsen flow yields $\theta_K = 13\,\mathrm{s}$ and for viscous flow $\theta_V = 21.6\,\mathrm{min}$. The latter agrees with experimental result, indicating that

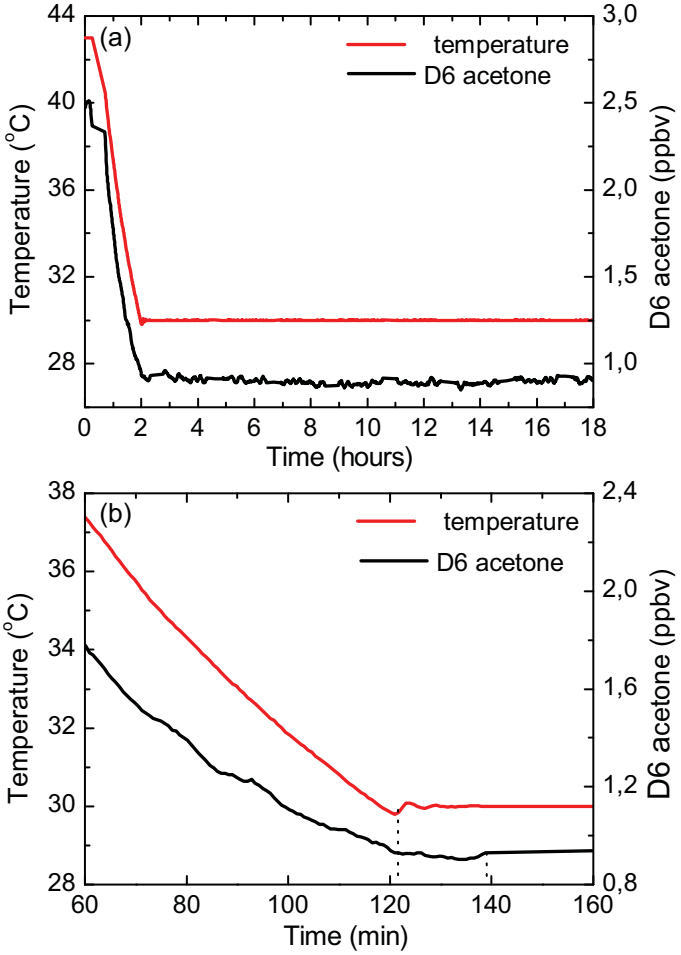

Figure 4.4: Temperature of the permeation device (red line) and D6-acetone mixing ratio (black line) during the entire test period of 18 hours (graph a) and during 100 minutes around the stabilization point (graph b)

the dominating regime is the viscous flow, i.e. the pores in the used PTFE membrane are considerably small so that the permeation through it may be described by the viscous flow approach detailed in Section 4.2.2.

4.4.2 Temperature dependence of the permeation rate

In order to characterise the calibration source in the desired temperature range, the permeation rate was repeatedly measured at various temperatures between 22 and 42°C, with results shown in Fig. 4.5. Such measurement results shows that the permeation rate is well defined simply by the temperature measurement, without hysteresis or memory effects. Moreover, the temperature dependence fits extremely well an Arrhenius function (Eq. 4.1), with the following equation:

$$P = 3.34 \cdot 10^{10} \cdot \exp\left(\frac{-6023.66}{T}\right) \tag{4.25}$$

in pg/min and with T in Kelvin and a correlation coefficient R^2 of 0.999. Moreover, the permeation rate measured can be directly compared adjusting to both permeation regimes, Knudsen and viscous flow (Eqs. 4.11 and 4.16), depicted in Fig. 4.6. The comparison of experimental findings with models agrees extremely well with the measured stabilization time, i.e. the permeation mechanism of the calibration source is indeed between Knudsen and viscous flow, however clearly dominated by the latter.

With the values obtained here, it is possible to calculate the influence of the stabilization time in the calibration of a given system. Using the measured permeation rate (Eq. 4.25), the stabilization time at 30°C (18 min) and the temperature drift (maximum of 340 mK h^{-1}) one can calculate the induced error due to stabilization time.

Consider the system stabilized at 30°C, according to Eq. 4.25, with a permeation rate of 77.61 pg/min. Following a sudden change in outside temperature to 50°C, the calibration source shows a temperature drift of 340 mK h^{-1}. After the stabilization time (18 min), the measured temperature has increased to 30.10 K. However, the permeation rate corresponds still to the previous temperature. By assuming the permeation-temperature relationship from Eq. 4.25, one would calibrate a given system using the permeation rate of 78.13 pg/min. Therefore, the difference between the actual and the estimated permeation rates is the induced error due the stabilization time, calculated as:

$$\sigma = 100 \times \frac{|77.61 - 78.13|}{78.13} = 0.7\,\% \tag{4.26}$$

Given that the maximum precision in a PTR-MS system is estimated ∼10-15 %

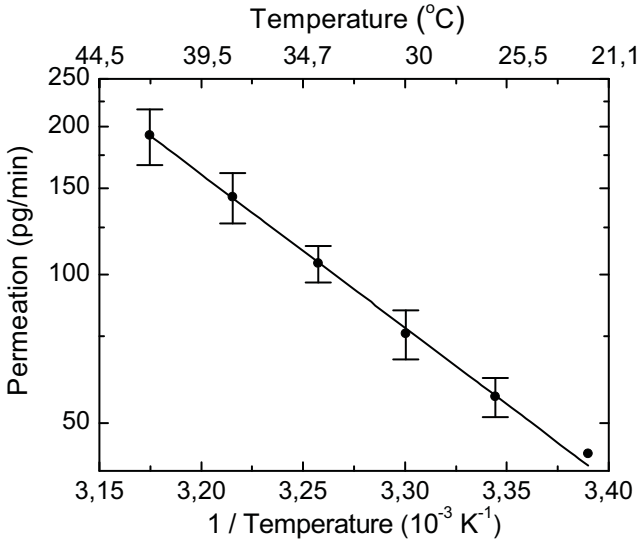

Figure 4.5: Experimental results from calibration source. Dots: Average permeation rate from six measurements. The error bars indicate the variability of the typically six measurement sequences at a certain temperature. At the lowest temperature (22°C) only one measurement was performed, limited by laboratory temperature. Line: Exponential fit. See text for details.

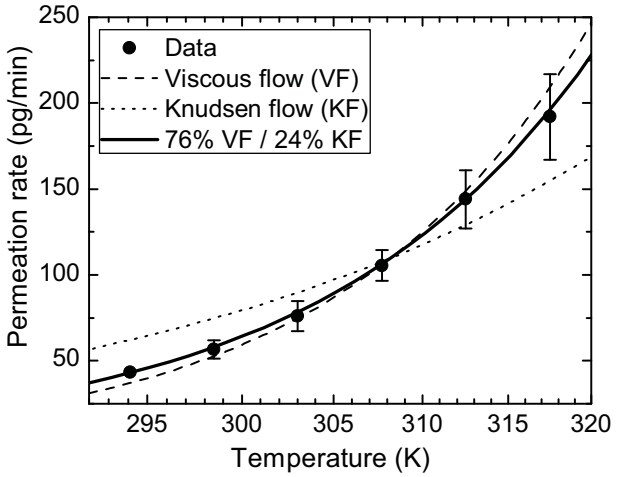

Figure 4.6: Comparison of experimental result of permeation regimes. Dots: Experimental results. Dashed lines: fit from Eqs. 4.11 and 4.16. Full line: Linear combination of Eqs. 4.11 and 4.16 to fit experimental data.

(see Section 3.6), the σ value is considered negligible and therefore the stabilization time does not influence the measurement accuracy.

4.5 Conclusion

This Chapter is adapted from a manuscript submitted to publication in a peer-reviewed journal. The unheated permeation device exploits permeation of gases through polymers in a new manner. By making use of a thin (and small) membrane, we developed a small and lightweight calibrating system for field (especially airborne) campaigns. Besides being installed at the new PTR-MS described in this work (Chapter 6), a second version is installed since mid 2010 in the PTR-MS deployed once a month for four consecutive flights within the passenger aircraft project CARIBIC (Chapter 7).

The permeation rate (and ultimately analyte concentration) of the calibration source is well within aimed values (0.5 - 2.5 ppbv), achieved adjusting the permeating surface with desired carrier gas flow. A long term stability test (months long) is considered unnecessary for two reasons: (i) The described system makes use of a PTFE membrane as permeating material, which is used in many standard permeating sources. (ii) The system is intended for field and airborne campaigns, where portability and short term robustness play an important role. Cross-calibration between campaigns is highly recommendable to account for permeability change over time, such as ageing effects.

As shown in the arguments leading to Eq. 4.26, the system temperature drift (hence, its heat capacity) must compensate a given stabilization time. Therefore, an even lighter calibration system could be constructed with a faster stabilization time. This could be achieved considering the following points: (i) Making use of a thinner (and smaller) PTFE membrane, or (ii) pushing the flow regime towards the Knudsen flow. As the former may present mechanical issues, such as withstand the pressure difference, the latter might be achievable with specially manufactured PTFE membranes [186].

The following Chapter presents the ion funnel enhance drift tube, an important new feature of the PTR-IF-MS as well, designed to increase the sensitivity of PTR-MS systems.

Chapter 5

The ion funnel enhanced drift tube

State-of-the-art Proton-Transfer-Reaction mass spectrometers (PTR-MS) have a high-sensitivity which ensures high-precision measurements in most of its applications. Exceptions include compounds with low proton affinity and fast (e.g. airborne) measurements at very low mixing ratios. Moreover, PTR-MS systems integrated with alternative detectors (ion trap or time-of-flight) still yield sensitivity orders of magnitude lower, still quite limiting its application. A review on PTR-MS technology is given in Chapter 3.

The drift tube (also called the reaction chamber) is a key region concerning PTR-MS sensitivity. Given the large number of collisions with neutral molecules, ions traversing the drift tube will tend to drift away from the centre line following a brownian motion and may be lost to the wall. According to our knowledge, a systematic study of the drift tube geometry on the ion transmission, as performed on ion mobility systems (e.g. by Soppart and Baumbach [187] and by Gillig et al. [188]), was never carried out in PTR-MS systems. Consequently, the increase of the ion transmission could lead to a notable system sensitivity increase.

Using ion trajectory simulations, we quantify the ion loss in the standard drift tube and several variations (Section 5.1). The result of such study motivates the use of Ion Funnel technology (Section 5.2), for the first time implemented in a PTR-MS system (Section 5.3).

5.1 Ion transport in the drift tube

The PTR-MS drift tube (reviewed in Section 3.3) is where primary ions (usually H_3O^+) ionize compounds of interest through proton transfer reactions. The drift tube has nowadays essentially the same design as originally proposed by Lindinger et al. [72].

Gillig et al. [188], working on ion mobility mass spectrometers, published in 2004 important results where geometrical considerations in the drift tube sufficed to increase manyfold the ion transmission, reaching nearly 100 %. The effect of the PTR-MS drift tube geometry on the transmission has been seldom investigated, relying solely on experimental results [35]. This Section details an effort to better understand the ion transport in the drift tube, especially the influence of the geometry in the ion transmission.

5.1.1 Ion trajectory simulation

In a nutshell, SIMION (Scientific Instrument Services, Inc., USA) solves Laplace equations for a given set of electrodes and determines the resulting ion path. Such method reaches results bearing perfection in high-vacuum without field distortions. Once molecular collisions are considered (mean free path smaller than the tracked length) the accuracy relies strongly on appropriate considerations of the interaction of ions with neutrals.

In many ion trajectory simulations, a viscous model is applied resulting generally in satisfactory results [189–191]. In such model, collisions with buffer gas are considered as a fluid where an equivalent drag force due to the buffer gas "viscosity" is applied. Such approximation is valid only if the ions are much heavier than the buffer gas and their kinetic energy does not largely exceeds thermal energy. However, in the drift tube of a PTR-MS, both assumptions are false, i.e. the mass of the ion is comparable with the mass of the buffer gas and the kinetic energy of the ions is much higher than the thermal energy (roughly an order of magnitude). As such, the scattering angle resulting from every collision has to be taken into account by means of a Monte Carlo simulation [192]. For the work presented here, a hard-sphere Monte Carlo model has been used.

Along the drift tube, the air velocity is three orders of magnitude lower than the ion velocity ($\sim$1 m/s compared to 1 000 m/s). Consequently, the buffer gas can be approximated as being stationary. However, close to the exit orifice gas velocity increases up to 100 m/s. To quantify the gas dynamics based on the solution of time-dependent Navier-Stokes equations [193, 194] and to implement in the ion trajectory simulation

is extremely time consuming and beyond the scope of this work.

5.1.2 Optimization of the drift tube geometry

Using the simulation tool described above, ion trajectories within different drift tubes have been simulated. A drift tube based on periodic focusing proposed by Gillig et al. [188], which strongly increased ion transmission in ion mobility system, has been simulated as well. The standard drift tube and five variations are depicted in Fig. 5.1 and 5.2, shown with only 20 ions for a better visualization.

The simulations were performed at the same E/N parameter, namely 115 Td (1 Td = 10^{-17} V cm^2, see Section 3.3.1), at a pressure of 2.3 hPa. Ions were considered to be transmitted if their position at the last plate was within the diameter of the exit orifice (1.2 mm). Results of the ion transmission and the time-of-flight are presented in Table 5.1.

Table 5.1: Results from drift tube simulations for 600 ions of m/z = 19, at 115 Td with a pressure of 2.3 hPa. Different drift tubes are shown in Fig. 5.1 and 5.2.

Drift tube	Transmission (%)	Time-of-flight (μs)	Sensitivity[a] (%)
Standard	7.0	103	-
Periodic focusing	4.1	183	+4
Uniform field	5.6	100	-22
Focusing piece	12.8	103	+82
Decreasing i.d.	7.2	103	+2
10 cm long	6.3	126	+10

[a] The sensitivity is relative to the standard drift tube. For the value depicted here, the sensitivity is approximated as directly proportional to the ion transmission and the reaction time (i.e. time-of-flight).

The ion mobility retrieved from ion simulations (resulting on a given time-of-flight) agrees extremely well with experimental results (Section 3.3.1). No strong increase in ion transmission has been observed for alternative geometries, except for the model implemented with a focusing piece.

Differently as reported in the work of Gillig et al., a periodic focusing PTR-MS drift

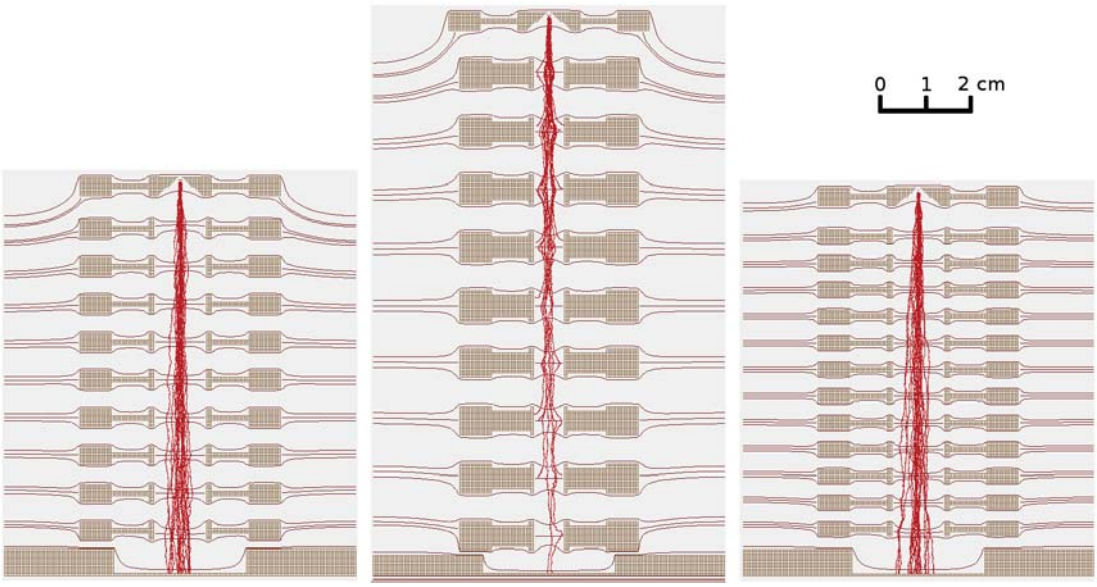

Figure 5.1: Different drift tube configuration simulations. Left: Standard drift tube. Centre: Periodic focusing drift tube based on the work of Gillig et al. [188]. Right: Uniform field drift tube.

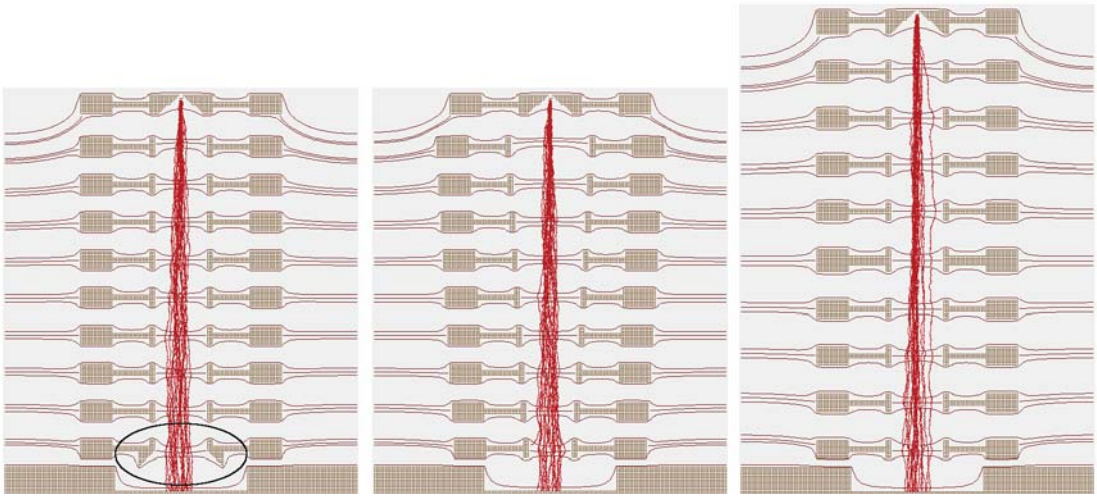

Figure 5.2: Different drift tube configuration simulations. Left: Standard drift tube implemented with a focusing piece, indicated in the figure. Centre: Decreasing diameter drift tube. Right: 10 cm long drift tube. The scale is the same as shown in Fig. 5.1.

tube does not show an increase in ion transmission (only 4.1% instead of 7%). This strongly different outcome is assumed to be due to the larger scattering of the ions in the PTR-MS drift tube in comparison to an ion mobility instrument[1]. Due to an increase in time-of-flight, it shows nevertheless comparable sensitivity as the standard drift tube.

The drift tube with decreasing inner diameter represents a larger group with many similar variations, including a drift tube with increasing inner diameter, alternating electrode diameters (10 / 13 mm), and increasing and decreasing spacing between electrodes along the drift tube. For all different geometries results very close to the standard drift tube were obtained.

A longer drift tube (10 cm) was tested as well resulting in 10 % sensitivity increase. Such sensitivity is the result of a decrease of ion transmission compensated by a higher increase in drift time. Such result agrees with publications of long PTR-MS drift tubes, with an overall result of higher sensitivity. As discussed in Section 3.3.3, despite leading to higher sensitivity measurements, longer drift tubes show disadvantages such as longer exchange times and (relatively) high voltage.

The focusing piece depicted in Fig. 5.2 has been manufactured and experimentally tested, however, without noticeable sensitivity improvement. Such result is related to uncertainties in simulations by assuming a stationary gas, as previously discussed. This assumption is specially problematic close to the exit orifice, where the focusing piece is located.

The study presented here yields two important results: (i) The ion transmission is around 10 % using the standard drift tube, and (ii) differently as reported for ion mobility instruments, variation in geometry do not show remarkable improvement in the ion transmission. Therefore, a more robust technique is required, i.e. the electrodynamic ion funnel.

5.2 Implementation of ion funnel in PTR-MS technology

Under high vacuum, ions can be manipulated with extreme precision and in a well understood fashion using magnetic and electric fields. As the pressure increases, collisions with gas molecules increasingly dominate the behaviour of ion motion. Particularly in the presence of strong gas dynamic effects, conventional ion optics become ineffective.

Most of the mass spectrometry techniques have their ionization regions operated at

[1]Ion mobility instruments usually have a much lighter buffer gas (e.g. He) in comparison to the travelling ions.

elevated (even atmospheric) pressures. Conversely, ion detectors are usually operated under high vacuum (pressures of $\sim 10^{-5}$ hPa and lower). Therefore, efficient transport between distinct pressure regions (usually via small radii orifices) is fundamental for a high-sensitivity system.

At pressures up to $\sim 10^{-2}$ hPa, efficient ion transport to high vacuum regions is achieved with ion guides (multipoles with radio frequency voltage only, see Section 3.4.1). However, at pressures of ~ 1 hPa and above (as in the PTR-MS drift tube), RF-only multipoles exhibit either an acceptance area that is too small to efficiently capture the ions from an expanding gas jet or an effective potential that is too weak to focus the ions into a narrow conductance-limiting aperture [195].

An efficient ion focusing technology for pressures above ~ 1 hPa was first published in 1997 by Shaffer et al. [196], i.e. the electrodynamic ion funnel. Ion funnel technology has been applied up-to-date mostly on ion mobility mass spectrometer systems applied to biological research (proteins and other large molecules with molecular weight, MW, higher than 500) [195, 197, 198]. However, successful implementation of the ion funnel into the PTR-MS system (with light, energetic ions) relies on overcoming a strong low mass cut-off. The focusing of light ions proposed in this work is, to our knowledge, the first ion funnel application in this mass range.

In the following, the ion funnel is described. Results from theoretical description are later applied to the construction of an ion funnel enhanced drift tube.

5.2.1 The electrodynamic ion funnel

The ion funnel is based on the stacked ring radio-frequency (RF) ion guide [199], which consists of a series of cylindrical ring electrodes of fixed inner diameter. Radio frequency potentials of opposite polarity are applied to adjacent electrodes. The arrangement creates an effective potential (also called pseudo-potential) that radially confines ions inside the ion guide. The effective potential, V^*, is proportional to the squared amplitude of the local RF electric field E_{RF}:

$$V^*(r,z) = \frac{z_i \cdot e \mid E_{\mathrm{RF}}(r,z) \mid^2}{16 \cdot m \cdot \pi^2 \cdot f^2} \tag{5.1}$$

Here z_i is the ion charge state, e the elementary charge, m the ion mass, and f is the frequency. The radial and axial positions are represented by r and z, respectively (Fig. 5.3). The stacked ring geometry generates the electric-field configuration that

corresponds to the following effective potential spatial distribution:

$$V^*(r,z) = V_{\text{trap}} \left[I_1^2 \left(\frac{r}{\delta}\right) \cos^2 \left(\frac{z}{\delta}\right) + I_0^2 \left(\frac{r}{\delta}\right) \sin^2 \left(\frac{z}{\delta}\right) \right] \tag{5.2}$$

where $\delta = d/\pi$, d is the spacing between the ring electrodes; I_0 , I_1 are zero and first order modified Bessel functions, respectively. V_{trap}, the axial effective potential well depth, is defined as:

$$V_{\text{trap}} = \frac{V_{\text{max}}}{I_0^2(\rho/\delta)} \tag{5.3}$$

where V_{max} is the maximum value of the effective potential at $r = \rho$, $z = d(i + 1/2)$, $i = 0, 1, ...$, defined as:

$$V_{\text{max}} = \frac{z_i \cdot e \cdot V_{\text{pp}}^2}{4 \cdot m \cdot \pi^2 \cdot f^2 \cdot \delta^2} \tag{5.4}$$

V_{pp} is the peak-to-peak amplitude. The stacked ring RF ion guide creates an effective potential distribution that corresponds to a steep potential gradient near the electrodes and a near field free region over most of the internal volume.

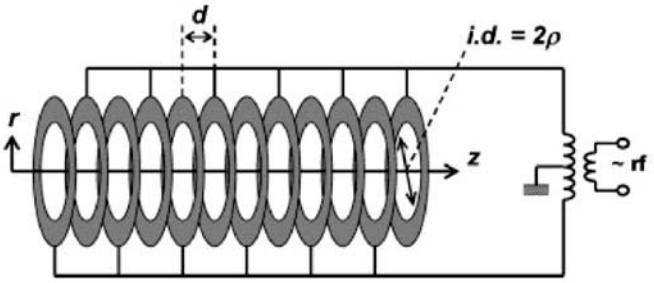

Figure 5.3: Schematic view of a stacked rings RF ion guide. *Obtained from Gerlich et al.* [199].

The ion funnel presents two main differences in comparison with stacked ring RF ion guides: (i) progressively smaller ring inner diameter, and (ii) a DC potential gradient applied to the ring electrodes. The former enables the spatially dispersed ion cloud entering the ion funnel to be efficiently focused to a much smaller radial size, while the latter, as in a drift tube, adds kinetic control on the ions instead of relying solely on gas dynamic effects [196, 200]. This feature takes advantage of the fact that the stacked ring ion guide geometry is naturally "segmented" in the axial direction, in contrast to the axial continuity of standard multipoles. Fig. 5.4 shows a schematic view of the ion funnel. Using the simulation tool described in Section 5.1.1, the ion funnel was modelled. The usual ion funnel is shown in Fig. 5.5.

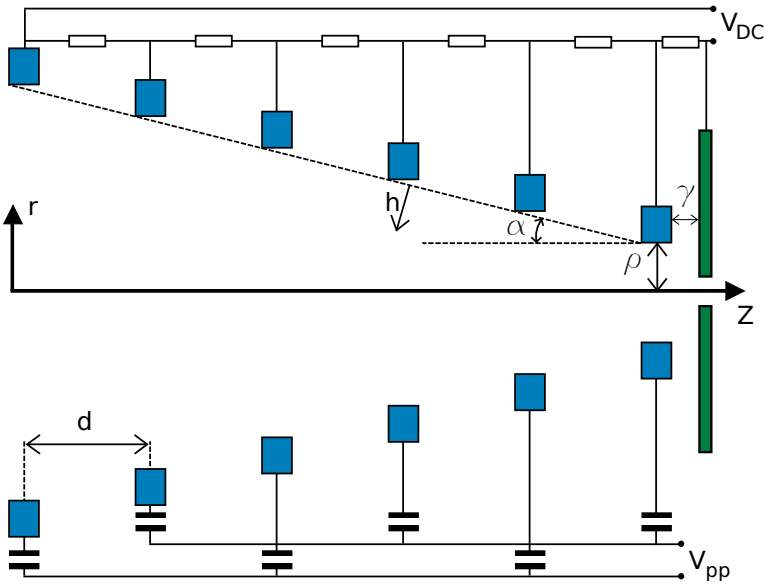

Figure 5.4: Schematic view of an ion funnel. In blue: Electrodes with decreasing inner diameter by an angle α, aperture radius ρ and electrode spacing d and spacing of the last electrode γ. In green: DC only plate with end orifice.

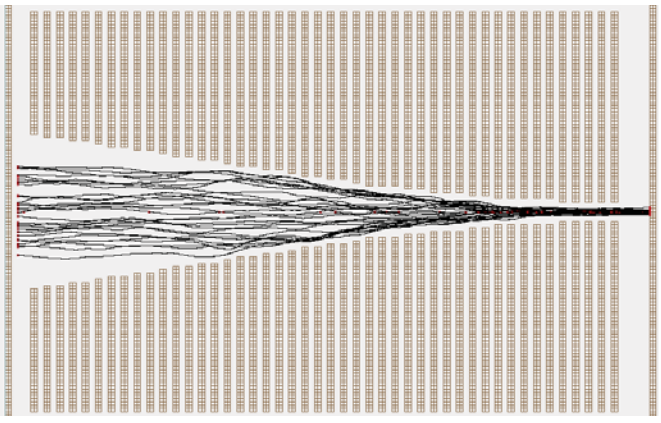

Figure 5.5: Example of ion focusing using an ion funnel. Shown is a simulation of 30 ions of m/z=500 at 2 hPa and buffer gas MW=4. The 50-electrodes IF is operated with V_{pp}=100 V, f=1.5 MHz and V_{DC}=50 V. Here, ρ=2.5 mm, d=2 mm, and α=12°.

Tolmachev et al. derived a set of useful relationships for the ion funnel [190]. The effective potential (V^*, Eq. 5.2) dependence on radius r can be approximated for $d > r > \rho$ as follows:

$$V^*(r) \approx \frac{V_{\max} \cdot \rho}{r} \exp\left(\frac{r-\rho}{\delta/2}\right) \tag{5.5}$$

and the axial well depth V_{trap} is given by:

$$V_{\text{trap}} \approx \frac{V_{\max} \cdot 2\pi \cdot \rho}{\delta} \exp\left(-\frac{2\rho}{\delta}\right) \tag{5.6}$$

Eq. 5.6 is extremely important when designing a new ion funnel. If $V_{\text{trap}} \approx V_{\max}$, ion transmission is strongly reduced, given that ions are trapped (and lost) within the ion funnel instead of successfully transmitted to the next vacuum chamber. Early ion funnel designs suffered from this trapping effect, limiting focusing efficiency.

As previously discussed, the focusing efficiency of an ion funnel is limited to a certain mass range. High mass cut-off can be derived considering that the focusing field ($E^* = -\nabla(V^*)$) must counterbalance the DC gradient force $E_n = E_{\text{DC}} \sin(\alpha)$, resulting in [201]:

$$E^*(h) = \frac{z_i \cdot e \cdot V_{\text{pp}}^2}{8 \cdot m \cdot \pi^2 \cdot f^2 \cdot \delta^3} \exp\left(\frac{-2h}{\delta}\right) \tag{5.7}$$

where h is the distance relative to the funnel's inner surface (see Fig. 5.4). Ions with higher m/z are trapped closer to the wall, i.e., at smaller h values. Therefore, if h is small enough, the ions will be lost. Assuming a balance of E_n and $E^*(0)$, the following estimation for the high m/z limit is found:

$$(m/z)_{high} = \frac{0.07 \cdot e \cdot V_{\text{pp}}^2}{4 \cdot m_u \cdot \pi^2 \cdot f^2 \cdot \delta^3 \cdot E_n} \tag{5.8}$$

where $m_u = 1.6605 \times 10^{-27}\,\text{kg}$ is the atomic mass unit.

Conversely, Page et al. [202] found a relationship for low mass cut-off by using an adiabaticity parameter [203], defined as:

$$\eta(h) = \frac{z_i \cdot e \cdot V_{\text{pp}}}{2 \cdot m_u \cdot \pi^2 \cdot f^2 \cdot \delta^2} \exp\left(\frac{-h}{\delta}\right) \tag{5.9}$$

The effective focusing occurs if the adiabaticity parameter is smaller than a certain threshold value $\eta(h) < \beta \leq 1$. Substitution of this condition into Eq. 5.7, using Eqs. 5.9,

leads to the following low m/z cut-off relationship:

$$(m/z)_{low} = \frac{2 \cdot e \cdot E_{\mathrm{DC}} \cdot \sin(\alpha)}{m_u \cdot \pi^2 \cdot f^2 \cdot \delta \cdot \beta} \tag{5.10}$$

For calculations of low mass cut-off presented here β is assumed to be 1.

5.2.2 Ion funnel optimization via ion simulation

Given the large number of parameters influencing focusing efficiency in an ion funnel, a program was written to automatically range all possible geometries and perform the simulation described in Section 5.1.1. Due to the large number of combinations, the optimization process was separated in two steps. In step I, the ion transmission of each given geometry is obtained at a fixed "kinetic" configuration (i.e. $E/N = 90\,\mathrm{Td}$, $V_{\mathrm{pp}} = 70\,\mathrm{V}$, and $f = 6\,\mathrm{MHz}$). The ion transmission was obtained via ion trajectory simulation of 20 ions of $m/z = 19$.

In step II, 20 geometries are selected according transmission results from step I. Thereafter, the ion transmission of each funnel is characterise for E/N, V_{pp} and frequency via ion simulation of 60 ions of $m/z = 19$. Table 5.2 depicts parameters ranged throughout ion funnel optimization.

Table 5.2: Parameters selected for ion funnel optimization.

Parameter	Values	Unit
Step I		
Number of electrodes	15, 20, 25	
Electrode thickness	0.2, 0.3, 0.4, 0.5	mm
Spacing d	0.5, 0.6, 0.7, 0.8, 0.9, 1	mm
Angle α	6, 8, 10, 12, 14	degrees
Last plate inner diameter ρ	1.6, 2, 2.4, 2.8, 3.2, 3.6	mm
Spacing of the last electrode γ	0.4, 0.6, 0.8, 1	mm
Step II		
Frequency f	2, 4, 6, 8, 10, 12	MHz
V_{pp}	10, 30, 50, 70, 90, 110	V
E/N	70, 100	Td

The ion funnel optimization simulated nearly 260 000 ion trajectories and took ~750 h. Fig. 5.6 shows result of a given ion funnel during step I of the optimization process. Example of the ion funnel characterisation is shown in Fig. 5.7.

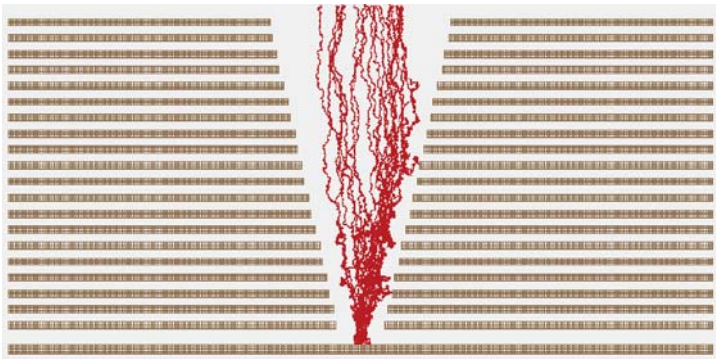

Figure 5.6: View of ion trajectory simulation performed in step I of ion funnel optimization. Results depicted here are with the following parameters: Number of electrodes: 20, electrode thickness: 0.2 mm, d: 0.7 mm, α: 12°, ρ: 2 mm and γ: 1 mm.

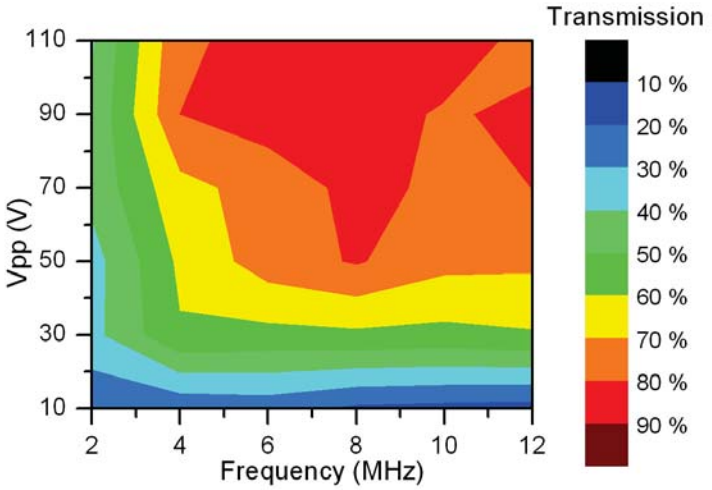

Figure 5.7: Ion transmission results obtained from simulation performed in step II. Results obtained using the ion funnel depicted in Fig. 5.6 and $E/N = 100$ Td. Low mass cut-off can be observed at lower frequencies and lower voltages.

Several ion funnel geometries showed similar results as shown in Fig. 5.7, indicating an optimum at a frequency of 6-8 MHz and $V_{pp} > 70$ V. Moreover, the selection of an ion funnel for construction must take in account experimental constraints (e.g. power supply). Analysis of experimental constraints and description of the geometry selected for construction is given in Section 5.3.

As previously discussed, the focusing effect achieved with an ion funnel is expected to increase ion transmission, thus increasing the system sensitivity. However, the electrodynamic drift tube has a large potential beyond ion focusing. In the following, one key aspect developed here, the ion declustering via RF excitation, is presented.

5.2.3 Declustering via electrodynamic excitation

In the PTR-MS drift tube, ion clustering may occur forming $H_3O^+ \cdot (H_2O)_n$ or $RH^+ \cdot (H_2O)_n$, RH^+ being the ionized organic. Besides complicating mass spectra interpretation, clustering might even decrease the ionization efficiency (see Section 3.6). To minimize the amount of clustered ions in the drift tube, the kinetic energy of the ion is kept high (0.2 eV $\approx$ 1000 K ion effective temperature) due to strong accelerating voltage E_{DC} (roughly 75 V cm^{-1}). As such, declustering is achieved via energetic collisions with neutrals.

Within an ion funnel enhanced drift tube, the oscillating electrical field considerably increases the kinetic energy of the ions. Consequently, the drift tube voltage gradient (therefore the axial velocity of the ions) can be decreased, while water clustering is kept at low levels. Fig. 5.8 depicts the ion energy depending on RF voltage amplitude obtained from simulation.

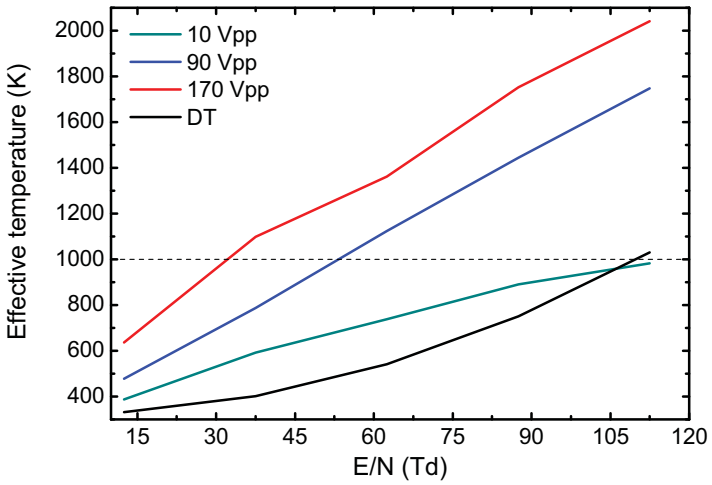

Figure 5.8: Ion effective temperature dependence of RF voltage in a electrodynamic drift tube. Solid black line: Theoretical calculation for DC voltage only (Eq. 3.15 in Section 3.3.1). Other solid lines: Average ion effective temperature from simulation of 600 ions m/z=19 (primary) and 600 ions m/z=59 (ionized acetone) within ion funnel depicted in Fig. 5.6 at 8 MHz. Dashed line: Ion effective temperature for ion declustering.

Fig. 5.8 indicates that low clustering levels could be achieved at much lower DC

voltage acceleration (E/N ratios). This increase in drift (or reaction) time corresponds to a potentially strong increase in system sensitivity. Moreover, an efficient focusing would allow to decouple the length of the electrodynamic drift tube and the reaction time, i.e. a small volume (with fast air exchange) drift tube would allow much longer reaction times.

In the following, the ion funnel enhanced drift tube is described.

5.3 Instrumental

Effective focusing achieved in the simulation described here might be not be straightforward to achieve in a real system. Resonance and signal reflection at such radio-frequency are often problematic. Moreover, capacitance of an ion funnel might strongly limit the voltage amplitude V_{pp}. In the following, a brief analysis of the application of ion funnel in PTR-MS systems is provided.

5.3.1 Application analysis

The following points summarize important aspects of the implementation of an ion funnel in a PTR-MS system:

- The voltage gradient that pushes the ions across the funnel, E_{DC}, works against the focusing field E^*. As previously discussed, in a PTR-MS system E_{DC} must be considerably high to keep water clustering low. Therefore, in order to achieve efficient focusing in PTR-MS systems, the parameter E^* (or ultimately the voltage amplitude V_{pp}, see Eq. 5.7) must be considerably high.

- As previously discussed, the ion funnel application described here is intended to focus light ions ($19 < m/z < 150$), differently than any previous published application. Furthermore, the low mass cut-off (Eq. 5.10) is proportional to E_{DC}. To overcome such cut-off, the electrode spacing δ needs to be smaller and/or the the voltage frequency (f), higher. Considering that a decrease in the electrode spacing usually has mechanical limitations, the low mass cut-off is must be overcome using a higher frequency f.

Up-to-date, most of ion funnel applications have shown efficient focusing with a frequency between 0.3 and 2 MHz and voltage amplitude between 40 and 200 V [197, 198, 204–206], usually achieved with a resonant circuit for (reasonably) low-power signal amplification. This solution, however, is limited to a single voltage frequency and is

not practical for system characterisation, specially in a new range of ion masses. To be able to test the electrodynamic drift tube in a frequency range (e.g. between 3 and 15 MHz), a high power solution is required.

When applied with an RF voltage, the parallel plates of an ion funnel will have a capacitance C (inversely proportional to δ), consequently, an impedance defined as:

$$Z = \frac{1}{2 \cdot j \cdot \pi \cdot f \cdot C} \tag{5.11}$$

where j denotes the imaginary number. Therefore, in a simple analysis, the necessary power to achieve a given voltage amplitude is:

$$Pow = \frac{V_{\mathrm{pp}}^2}{2Z} = V_{\mathrm{pp}}^2 \cdot \pi \cdot f \cdot C \tag{5.12}$$

Considering Eq. 5.12 and the points discussed above, an ion funnel implemented into a PTR-MS will clearly require higher power to achieve efficient focusing than any previous application. The experimental setup and results are presented in the following.

5.3.2 Results

Taking in account theoretical analysis (Section 5.2.1), simulation results (Section 5.2.2) and power requirement calculation (Section 5.3.1), two electrodynamic drift tubes (E-DT) have been selected for construction (see Table 5.3). E-DT I is based on a work published by Julian et al. [191] which describes an efficient ion funnel with a large electrode spacing (δ). Such ion funnel is easier to be constructed and requires less power to be driven. E-DT II is the result of the extensive ion funnel optimization described in Section 5.2.2. Nevertheless, its use at such high frequency range leads to a large capacitance, which translates into a possible limitation in focusing capabilities due to power requirements.

The voltage supply for the ion funnel is composed of a sine function generator and a 200 W signal amplifier, shown in Fig. 5.11. Due to the large influence of the reflecting signal, a 3 dB attenuator was placed in the output of the signal amplifier, limiting the output power to 100 W. As previously discussed (Section 5.2.1), the RF signal must be separated in two 180° out-of-phase voltages for adjacent electrodes. Such signal separation is performed here using a home-built transformer with a toroidal ferrite core.

Table 5.3: Ion funnel enhanced drift tubes chosen for experimental test. Fig. 5.9 and 5.10 depicts ion funnel I.

Parameter	E-DT I	E-DT II	Unit
Number of electrodes	14	20	
Acceptance diameter	11.9	8.0	mm
Electrode outer diameter	35.0	35.0	mm
Electrode thickness	0.2	0.2	mm
Spacing d	2.2	0.7	mm
Angle α	8.0	12.0	degrees
Last plate inner diameter ρ	3.2	2.0	mm
Length of the ion funnel	3.1	1.4	cm
Length	5.6	5.5	cm
Capacitance[a]	0.23	1.33	nF
Power required[b]	40	220	W

[a] With f=8 MHz.

[b] Calculated using the Eq. 5.12 considering V_{pp}=80 V.

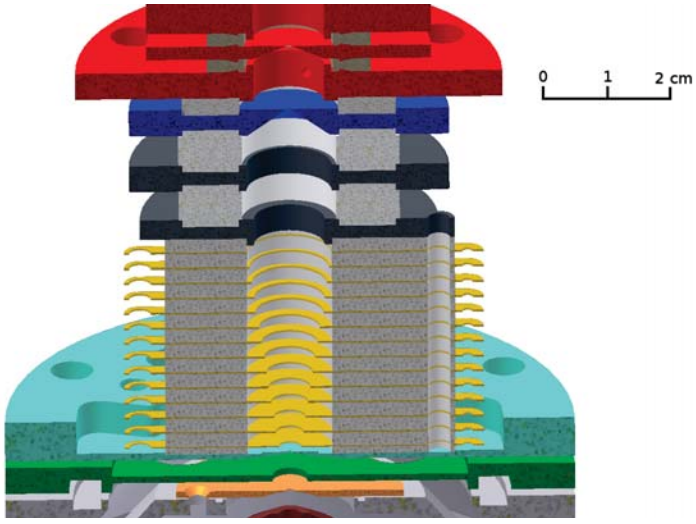

Figure 5.9: CAD cut view of the E-DT I. In red: Ion source; dark blue: entrance of ion funnel drift tube and air injection; in dark grey: drift tube guide plates; yellow: ion funnel electrodes; light grey: PTFE spacers; light blue: end plate of ion funnel drift tube; green: intermediate piece; orange: nose cone; brown: entrance of quadrupole. For details see text.

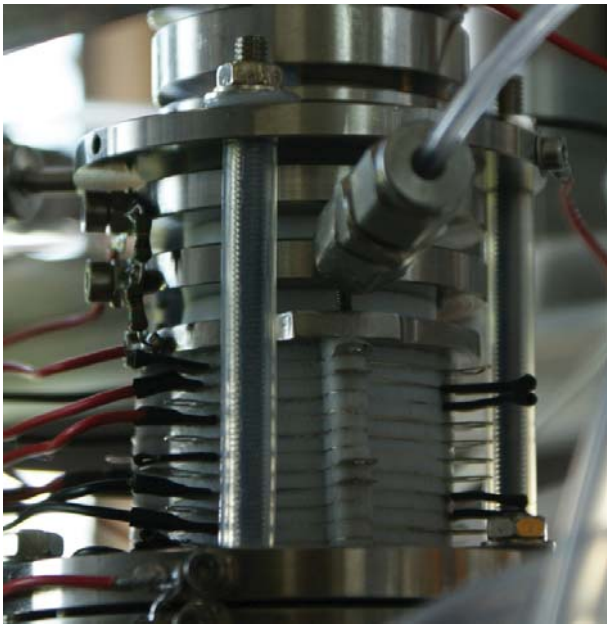

Figure 5.10: Photograph of the E-DT I installed in the PTR-MS.

Despite the high output power of the signal amplifier, the maximum value of V_{pp} was 70 V and 15 V for E-DT I and II, respectively, yielding an optimum frequency around 7-8 MHz. Lower frequencies (below 5 MHz) showed strong signal deformation. Conversely, at higher frequencies the signal amplitude decreased sharply.

As previously discussed, the ion funnel in E-DT I was based on a publication by Julian et al. [191] which claims to achieve high ion transmission using an ion funnel with large electrode spacing. Designed to focus "heavy" ions, the ion funnel described in the publication was operated at 0.65 MHz. Whereas focusing effect was not observed using the E-DT I, the relatively high voltage amplitude leads to a marked declustering effect, shown in Fig. 5.12. Such effect allows to decrease the ion drift velocity and, correspondingly, leads to an increase in 30 % of the system sensitivity.

Following the sensitivity increase due to the electrodynamic drift tube, a resonant-based signal amplifier is currently being constructed to the operate at 8 MHz. This new design shall strongly increase the RF voltage amplitude enabling focusing with E-DT II and leading to further enhancement of the system sensitivity.

5.4 Conclusion

The ion trajectory simulation accounting for a more accurate ion/molecule interaction allows for a systematic study of the influence of the drift tube geometry in the ion

Figure 5.11: View of function generator (Agilent Technologies, USA, model 33220A) and signal amplifier (BEKO Elektronik, Germany).

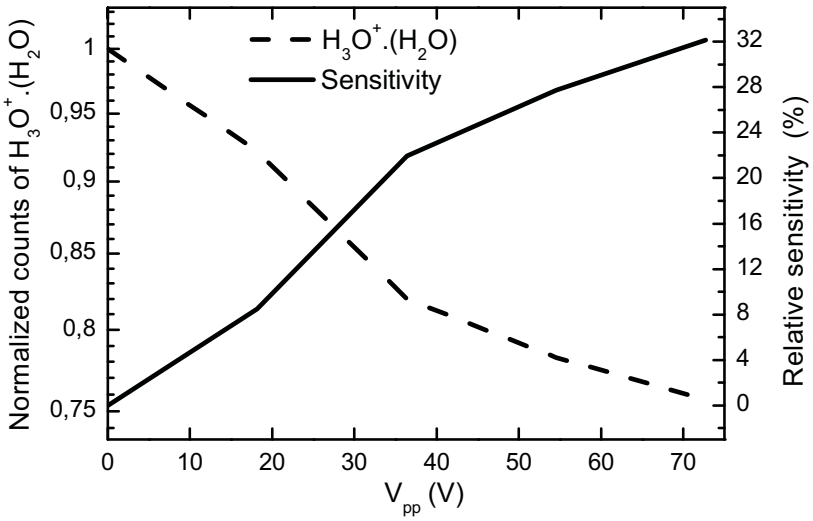

Figure 5.12: Experimental results using the electrodynamic drift tube I. Dashed line: Normalized primary cluster ($H_3O^+ \cdot H_2O$) experimentally observed. Full line: Relative sensitivity due to increase in drift time (not simultaneously measured). The ion funnel was operated at 8 MHz and the pressure was 2.3 hPa. Test performed sampling air from outside the laboratory.

transmission. With a maximal transmission of roughly 10 %, a more robust technique (the electrodynamic ion funnel) is required, here applied for the first time in a PTR-MS system.

According to our knowledge, all previous applications of ion funnel technology are limited to "heavy" ions ($m/z > 500$), in contrast to the application described here ($19 < m/z < 150$). Given the use of the ion funnel in a new mass range, we used a power supply which allows multiple frequencies to be tested. Such supply is composed of a sine function generator and high power signal amplifier, instead of the usual solution based on a resonant (low power) circuit.

Two electrodynamic drift tubes have been chosen for construction, entitled E-DT I and II. With the broad range signal amplifier used in this work best result was achieved using E-DT I, with an increase of over 30 % in sensitivity. A matched amplifier is being currently developed and will soon be ready for testing, further enhancing system sensitivity.

The following Chapter presents the novel PTR-IF-MS, including 10-days long air analysis using the electrodynamic drift tube described here.

Chapter 6

The novel PTR-IF-MS

This Chapter presents a new lightweight, high sensitivity Proton-Transfer-Reaction mass spectrometer (PTR-MS). In short, PTR-MS is a chemical ionization mass spectrometer capable of performing real-time measurements of many Volatile Organic Compounds (VOCs) in air with mixing ratios as low as pptv (pptv = 10^{-12} mol/mol). An overview of the PTR-MS technology is given in Chapter 3.

The PTR-MS described here has been developed focusing airborne deployment, specifically onboard the new German research aircraft HALO (**H**igh **A**ltitude and **LO**ng Range Research Aircraft, described in Section 6.1). The system presents two important innovations, the unheated permeation-based calibration source (Chapter 4) and the ion funnel enhanced drift tube (Chapter 5) .

Fully automated, the new ion funnel enhanced PTR-MS, shortened to PTR-IF-MS, has been almost completely built in-house. Key components towards the lightweight construction of this new system are discussed in Section 6.2.

A description of the PTR-IF-MS, measurement results and a brief discussion on the HALO certification process is given in Section 6.3.

6.1 The HALO research aircraft

The HALO aircraft (shown in Fig. 6.1) is based on a modified Gulfstream G550 - a large business jet. It has a payload of 2 tons for scientific instrumentation, maximum endurance of over 12 000 km and a flight ceiling altitude of 15 km. As of 2012, up to 5 scientific campaigns per year are expected to take place. One of the first scientific campaigns is entitled Oxidation Mechanisms Observations (OMO), during which the PTR-IF-MS is expected to be deployed, as well as during missions thereafter.

Figure 6.1: The HALO research aircraft.

6.1.1 The Oxidation Mechanisms Observation scientific mission

The extra-tropical free troposphere is a sensitive region of the atmosphere in terms of the climate response to chemical composition changes. In the northern hemisphere, the free troposphere is substantially impacted by the long-distance transport of air pollution, supplied by episodic pollution uplift in convection and more gradual upward transfer in the warm conveyor belts of cyclonic disturbances [10–12].

As discussed in Chapter 2, the removal rates of biogenic and anthropogenic gases, as well as the formation of tropospheric Ozone, are strongly controlled by oxidation reaction with HO_x radicals ($OH + HO_2$). Since only very few extra-tropical free troposphere measurements of radicals and precursor gases have been performed [207, 208], present assessments of atmospheric composition and climate change are strongly dependent on simulations with inadequately tested chemistry and general circulation models.

The OMO campaign aims to determine the rates at which natural and human-made compounds are converted by oxidation processes in the upper troposphere, which in turn affect the lifetime and the global distribution of air pollutants and several greenhouse gases, including tropospheric ozone. HO_x radicals shall be measured, along with the major sources and sinks to test model calculations.

The campaign will encompass about 6-7 measurement flights of about 8-hour duration during a 2-week intensive field phase. Roughly 15 instruments are considered for the campaign in order to measure, besides non-methane VOCs, aerosols, H_2O, CH_4, PAN, CO_2, NO_x, OH/HO_2, among others.

6.2 Airborne-oriented construction

Throughout system development, many new components have been constructed focusing field (especially aircraft) deployment. In the following, a description of important components/developments for the lightweight construction of the PTR-IF-MS are given. One of the most notable developments towards a lightweight system is the new calibration source, presented in Chapter 4.

6.2.1 The new gas flow design

A stable pressure in the drift tube is crucial for operating the PTR-MS. In the laboratory, a manual Teflon bodied needle valve in the inlet line suffices to stabilize the pressure in the drift tube [29]. However, fast changes in the outside pressure, especially during aircraft deployments (1 000 hPa at ground level down to ∼150 hPa in the low stratosphere), require an automated solution. In such pressure range, pressure stability can be easily achieved with a commercial mass flow controller. However, there are no controllers suitable for high-sensitivity VOC measurement readily available, specially due to their sealing material, e.g. rubber.

An alternative to commercial mass flow controllers, adopted by several groups, exploits the fact that the gas flow through a critical orifice is (usually) only defined by its back-pressure [55, 61, 126]. Therefore, the flow can be accurately controlled with a commercial back-pressure controller. Such gas flow design, as depicted in Fig. 6.2, was applied to the strongly adapted commercial PTR-MS from our group [34], prior to the integration of the developments described here. Despite accurate pressure regulation, the main drawback consists of the large amount of air discarded under higher outside pressure. Consequently, such design requires a large (and heavy) pumping system.

To minimize the amount of discarded air, a new mass flow controller suitable for VOC measurement has been developed. Combining the coil and shaft of a commercial controller (Sensortechnics GmbH, Germany) with a custom-made body made of PEEK[1] and sealing of PTFE[2], the controller (Fig. 6.3 and 6.4) efficiently regulates the pressure without discarding air. The use of this new mass flow controller (combined with the novel calibration source) allows to simplify the gas inlet system as depicted in Fig. 6.5. Furthermore, such design allowed to replace the back-pressure pump by a much lighter model[3].

[1] Polyether ether ketone
[2] Polytetrafluoroethylene
[3] Vacuubrand GmbH, Germany. Model MD 4 (16.4 kg) replaced by MD 1 (6.5 kg).

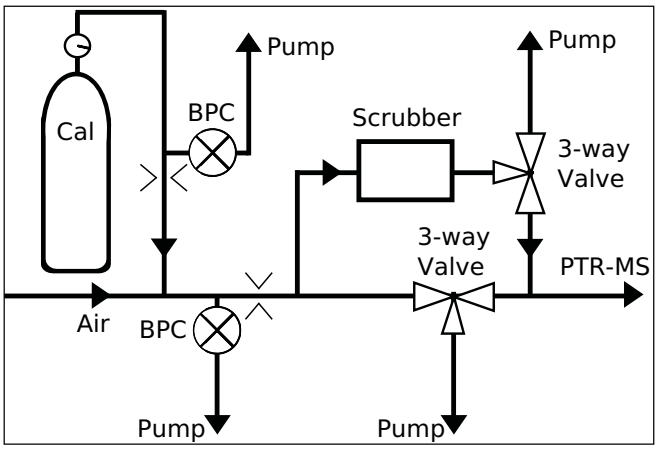

Figure 6.2: Sketch of the old gas flow design using a critical orifice and a back-pressure controller (BPC) for flow regulation. Calibration is performed by addition of calibration gas into air stream, regulated by BPC as well. Zero air is obtained via a VOC scrubber (Pt-catalyst at 350°C). Zero air measurement is performed by alternating both 3-way valve, introducing whether sample air or scrubbed air into the PTR-MS, discarding the other.

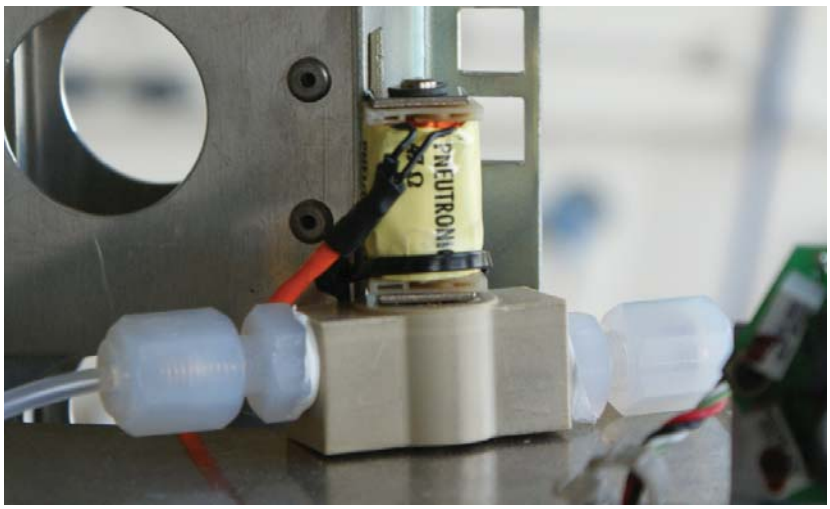

Figure 6.3: Photo of the new PEEK-bodied mass flow controller adapted for VOC measurement.

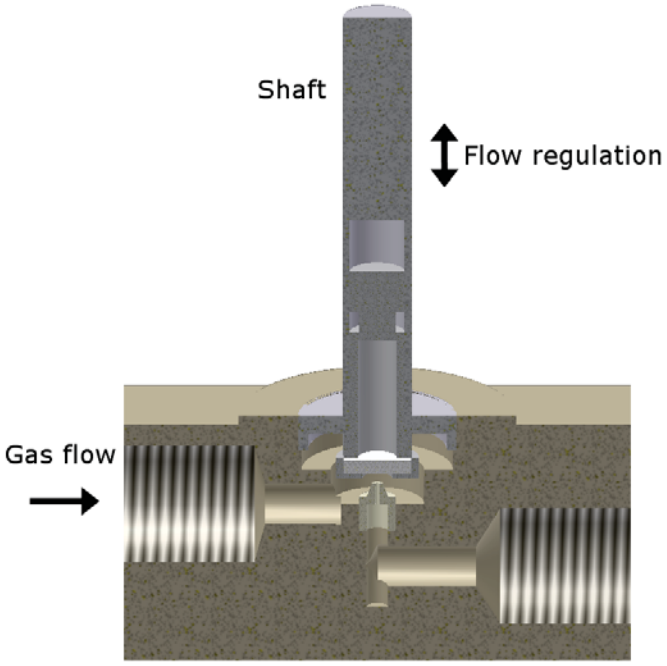

Figure 6.4: CAD cut view of the mass flow controller shown in Fig. 6.3. The component is depicted without the shaft-controlling coil adapted from the commercial controller.

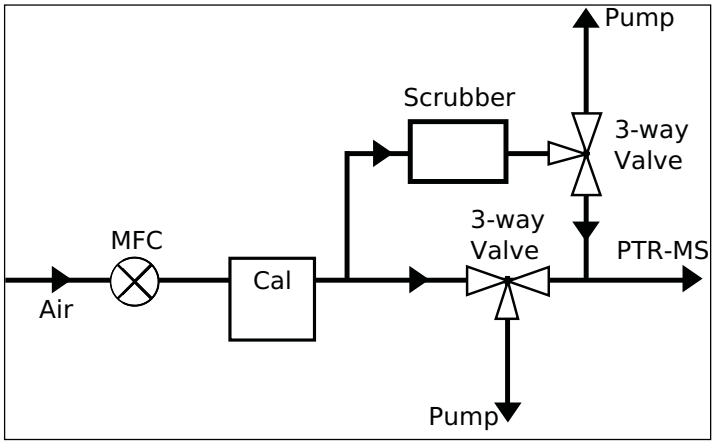

Figure 6.5: Sketch of the new gas flow design using a PEEK-bodied mass flow controller (MFC) shown in Fig. 6.3. Calibration is performed using the newly developed calibration source described in Chapter 4. Zero air measurement is performed as described in Fig. 6.2.

6.2.2 Controlling electronics

The electronics and components for power conversion/distribution are located in two 19" sub-racks, entitled electronic module I and II (EM-I and II, Fig. 6.6). In the EM I, the V-25 computer, developed at the Max Planck Institute for Chemistry in Mainz, is located. Due to its compact size and robustness, this embedded computer is largely used in in-situ scientific instruments for atmospheric measurements. Normally responsible for instrumental housekeeping, the V-25 computer implemented in the PTR-IF-MS has been expanded to drive the mass spectrometer and record spectra, replacing the bulky, Windows-based commercial electronics.

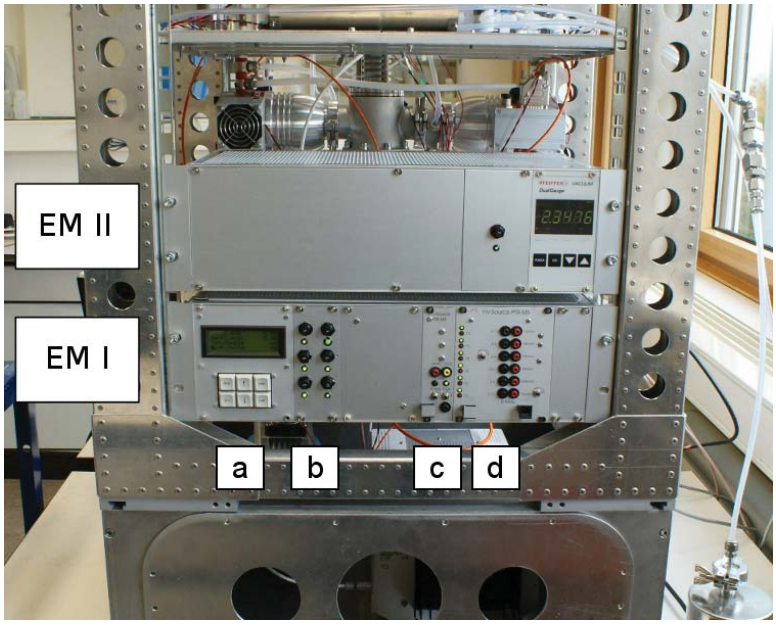

Figure 6.6: Front view of the PTR-IF-MS. EM-I: (a) the V-25 computer, (b) circuit breakers and power indicating LEDs, (c) current supply for the ion source and (d) voltage supply for the drift tube. EM-II: Dual gauge pressure sensor and its circuit breaker and power indicator LED.

6.2.3 Lightweight vacuum tubing system

The standard PTR-MS quadrupole vacuum housing is made of two heavy stainless steel flanges. In the PTR-IF-MS, this housing has been replaced by a single custom-made piece made of wealdable aluminium EN AW-7020, shown in Fig. 6.7. An intermediate vacuum chamber (also visible in Fig. 6.7) has been manufactured as well using the same material. The inner surfaces of the aluminium pieces have been carefully polished

to minimize out-gassing effects. Feed-through flanges were manufactured and sent to Pfeiffer Vacuum GmbH, Germany, for integration with the quadrupole system.

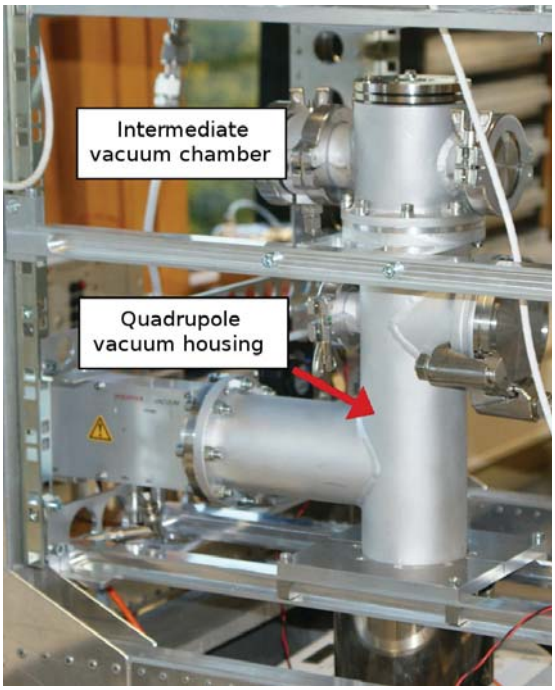

Figure 6.7: Photo of the custom-made intermediate vacuum chamber and quadrupole vacuum housing made of wealdable aluminium EN AW-7020.

6.3 The system

The system presented here is the worldwide lightest high-sensitivity PTR-MS, result of a strongly airborne-oriented development. With calibration, the PTR-IF-MS weights only 57 kg (the standard system weights ∼120 kg and more). The instrument presented here is (excepting the quadrupole system) completely built in-house. The peak power consumption is 400 W, designed for aircraft voltage (115 V at 400 Hz), however easily switchable to 24 V DC.

Detection sensitivity of the PTR-IF-MS is comparable with state-of-the-art systems. For example, acetone (CH_3COCH_3) is measured with 320 Hz ppbv^{-1} and shows a limit of detection of 12 pptv for 5 s integration time or ∼4 pptv for one minute integration time (shown in Section 6.3.2). Moreover, the system has been constructed according to the German Aerospace Centre (DLR) guidelines for aircraft scientific instrumentation. All materials/components are aircraft certified, minimizing posterior efforts for instru-

mental certification on aircraft deployment. The PTR-IF-MS is completely automated, therefore no operator is required. A CAD view of the instrument is presented in Fig. 6.8 and a photograph in Fig. 6.9.

6.3.1 Overview

In the following, a brief overview of the system and its main components, indicated in Fig. 6.10, is given:

Electronic module I. Power conversion from 115 V/400 Hz to 24 V DC (Vicor Corporation, USA) and distribution throughout the system. It houses as well a V-25 computer, discussed in Section 6.2.2 and the current supply for the ion source and DC voltage supply for drift tube/ion funnel (Hoffmann Messtechnik GmbH, Germany).

Electronic module II. Houses dual gauge control unit (Pfeiffer Vacuum GmbH, Germany, model TPG 262). The dual gauge controller interfaces two pressure sensors: at the drift tube and at the quadrupole region. This module will house an aircraft suitable ion funnel RF supply, currently driven with a laboratory version.

MS-Analyser. Actual spectrometer. Combination of a HCD ion source (Section 3.2.1), electrodynamic drift tube I (Section 5.3.2) and a quadrupole detector (Section 3.4). The vacuum is achieved with three turbomolecular pumps (Pfeiffer Vacuum GmbH, Germany, model HiPace 80). The quadrupole detector is composed of quadrupole filter and ion counter (models QMA 400 and CP400, respectively, from Pfeiffer Vacuum GmbH, Germany).

Flow control plate. Here, the gas flow system discussed in Section 6.2.1 is located. It includes the unheated permeation source described in Chapter 4.

Radio frequency generator. Provides RF signal for quadrupole operation (Pfeiffer Vacuum GmbH, Germany, model QMH 400-5).

Diaphragm pump. The model MD 1 (from Vacuubrand GmbH, Germany) ensures a back-pressure of (at maximum) 10 hPa for the three turbomolecular pumps of the analyser.

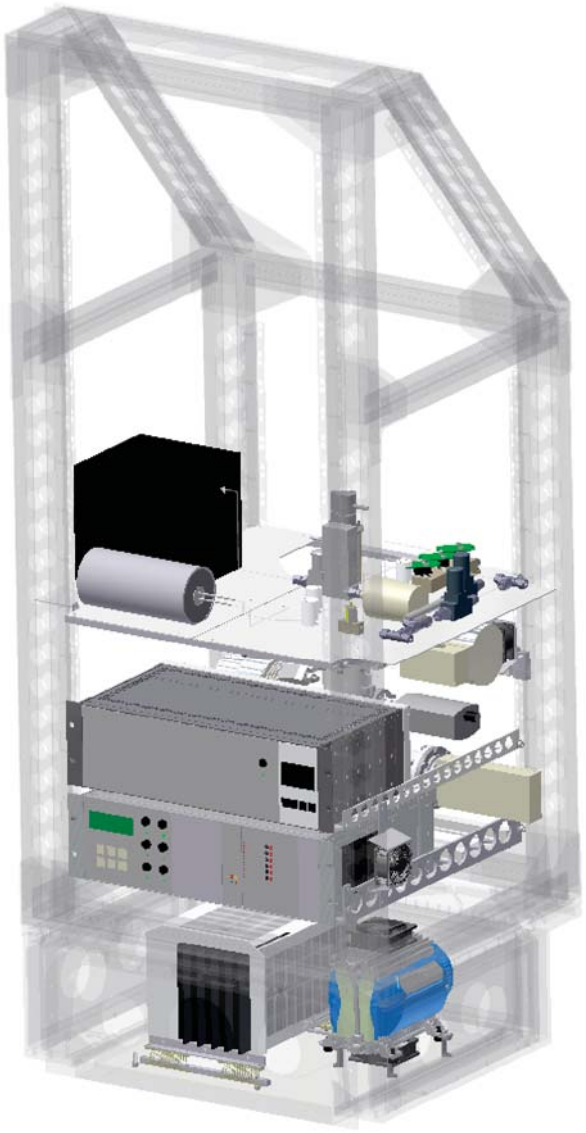

Figure 6.8: CAD view of PTR-IF-MS installed on the HALO rack (164 x 65 x 54 cm^3, height x side x depth). The system is 91 cm high and its centre of gravity (57 kg) is ~31 cm high. During OMO, the rack is planned to be shared with a high-precision 10 kg O_3 measuring instrument also developed in our group.

Figure 6.9: HALO rack with the PTR-IF-MS and the O_3 instrument. Picture taken during a electro-magnetic compatibility test.

Figure 6.10: Black: radio frequency generator; cyan: diaphragm pump; brown & green: electronic module I & II; violet: MS-Analyser; yellow: flow control plate. For details see text.

6.3.2 Instrumental results

Since it was first published [71], PTR-MS technology has been extensively characterised [29, 72, 90, 96, 115, 134, 209]. Throughout this work (specially in Chapter 3 and Appendices A and B) many of those results are discussed and therefore repetition of such tests is not presented here. Furthermore, innovations included in the PTR-IF-MS, namely the unheated calibration source and the electrodynamic drift tube, are described in Chapter 4 and 5, respectively.

The capability of the PTR-IF-MS as a fast, high-sensitivity VOC measuring system is demonstrated by analysing air sampled from outside the laboratory in Karlsruhe, Germany. Three VOCs were selected to be depicted here: acetone (CH_3COCH_3), isoprene (C_5H_8) and dimethyl sulphide (DMS – CH_3SCH_3).

The role of acetone in the atmosphere is shortly discussed in Section 2.3.1. It originates mainly from terrestrial vegetation and photochemical degradation of dissolved organic matter in oceans. Despite globally quite small (1 %), its anthropogenic emission can be very important locally. Mostly emitted/produced at ground level, due to its relatively long lifetime (∼1 month) it can be transported to the upper troposphere and lower stratosphere.

Isoprene is the most abundant biogenic VOC, emitted from many temperate and tropical forests [210]. For many plant species, a positive correlation between maximum diurnal change in isoprene emission and photosynthesis has been measured, leading to a well pronounced diurnal emission variation [211]. Furthermore, only recently the large role of isoprene on secondary aerosol formation has been identified [20].

DMS is the largest natural contributor to the global sulphur budget [212]. DMS is almost exclusively emitted from oceans by phytoplankton, however its emission from fresh water, e.g. formation by bacterial degradation of dimethylsulphoniopropionate (DMSP, $C_5H_{10}O_2S$), is not negligible [213, 214]. The main removal processes of DMS consists in oxidation by OH to various sulphur-containing compounds including sulphuric acid, a key component in atmospheric aerosol formation [215]. The reaction with OH results in a lifetime on the order of one to several days. Because of the photochemical source of OH, often DMS removal occurs only during daytime, leading to a pronounced diurnal mixing ratio variation close to the source [214].

The observations shown here were performed with the Ion Funnel I, with a RF voltage of 70 V_{pp} at 8 MHz (see Chapter 5). Furthermore, declustering due to oscillatory motion allowed the funnel to be operated at 70 Td, maintaining ion clustering below 10 % relative to the primary ion. Comparable result has been reported only by Jobson

and McCoskey using a cryogenic trap to remove water in the inlet line (Section 3.3.3). During the laboratory measurement described here, calibration was performed using a high-pressure gas bottle with well-defined mixing ratio of several VOCs. Result and description of the calibration process is given in Fig. 6.11. The sensitivity for acetone (Fig. 6.11) yields ∼320 cps/ppbv (LOD of 12 pptv), for isoprene 150 cps/ppbv (LOD of 26 pptv) and for DMS 210 cps/ppbv (LOD of 19 pptv). LOD is obtained for 5 s integration time and a limit of signal-to-noise ratio of 3.

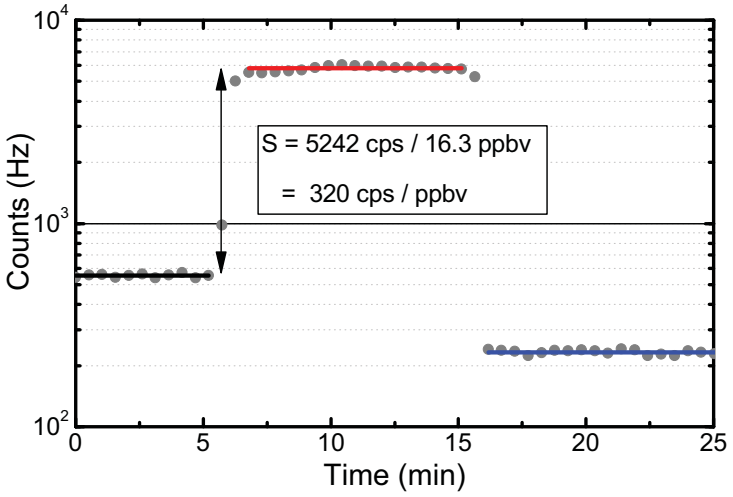

Figure 6.11: Results of instrumental sensitivity for acetone (m/z=59). Calibration was performed using a well-defined gas standard (Apel-Reimer Environmental, USA) having a mixing ratio of 500 ppbv. The calibration system is detailed in Fig. 6.2. 5 sccm (standard cubic centimetre per minute) of calibration gas was diluted in the main line of 153 sccm, leading to a known VMR of 16.3 ppbv. The system was calibrated every 120 min. Dots: Measurement. Black line: Averaged counts during measurement. Red line: Averaged counts during calibration. Blue line: Averaged counts during zero-air measurement.

Fig. 6.12 depicts results from 10-days long measurements. The data yields strong diurnal variation in isoprene due to its plant emission cycle, in combination with a relatively short lifetime (∼1 h).

Acetone measurement depicts mixing ratios of 1–2 ppbv, except for clear interference from nearby laboratories, given it is often used as cleaning agent. Background variation of acetone is estimated to be from variation in direct emission/wind direction.

DMS shows decreasing mixing ratios from ∼200 pptv at the beginning and below 100 pptv at the end. The variation in mixing ratio (including a peak at roughly 6.5 days) is possibly originated from bacterial degradation of DMSP in the Rhine river [213, 214].

Despite HALO being strongly delayed, the PTR-IF-MS has already taken part on

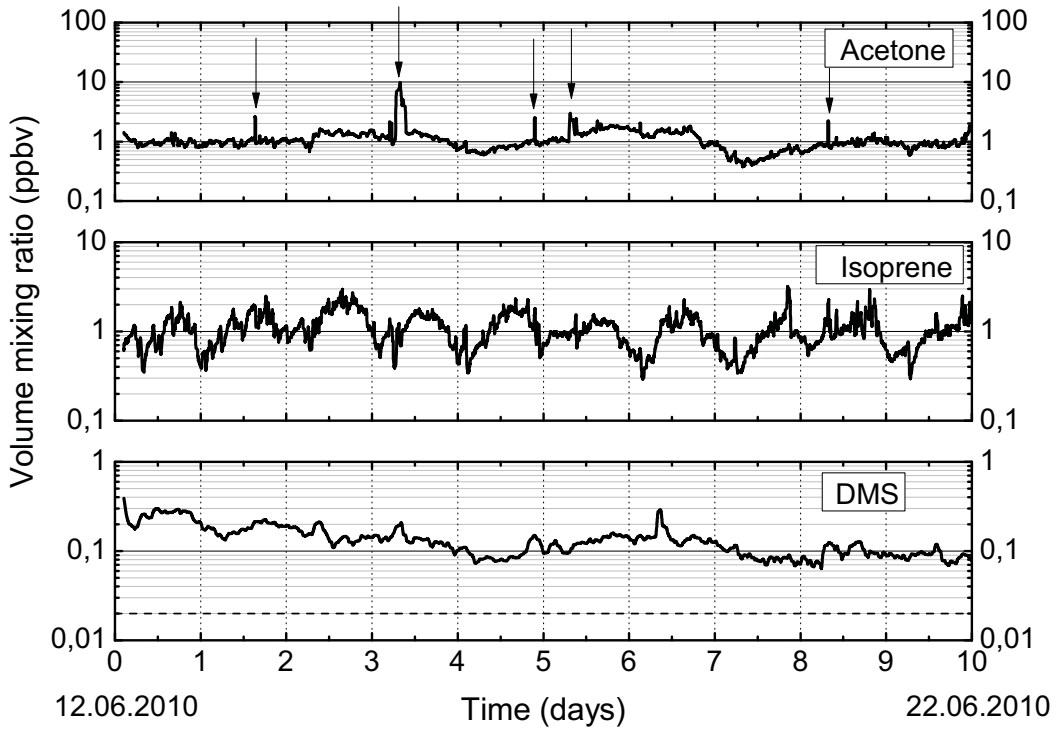

Figure 6.12: Result of 10-days measurements sampling air from outside the laboratory located at the KIT Campus north, surrounded by relatively dense woods, located 10 km north of the city of Karlsruhe and ∼6 km east of the Rhine river. Arrows in the acetone measurement indicates probable interference from nearby laboratories. Dashed line in DMS measurement indicates LOD for 5 s integration time (19 pptv). LOD for acetone and isoprene are below the scale (12 and 26 pptv, respectively). See text for details.

an extensive certification process, shortly described in the next Section.

6.3.3 HALO certification process

All scientific instruments intended to be deployed onboard HALO must succeed a strict certification process. During the certification process for the PTR-IF-MS, an extensive system description has been submitted (adding up to 15 documents), including a list all cables with information on connectors, length, material for each cable and pin assignment of each connector. Description on system construction and finite-element method mechanical stress calculations has been included as well.

Constructed focusing on airborne deployment, the PTR-IF-MS does not contain pressurized gas cylinders nor toxic gases, radio-active materials or other dangerous goods. Moreover, the system contains only negligible amounts of organic liquids, i.e. below 0.5 ml of acetone, acetonitrile, and methanol. The system description (see an example in Fig. 6.13) is readily obtained, given the system has been almost entirely built in-house.

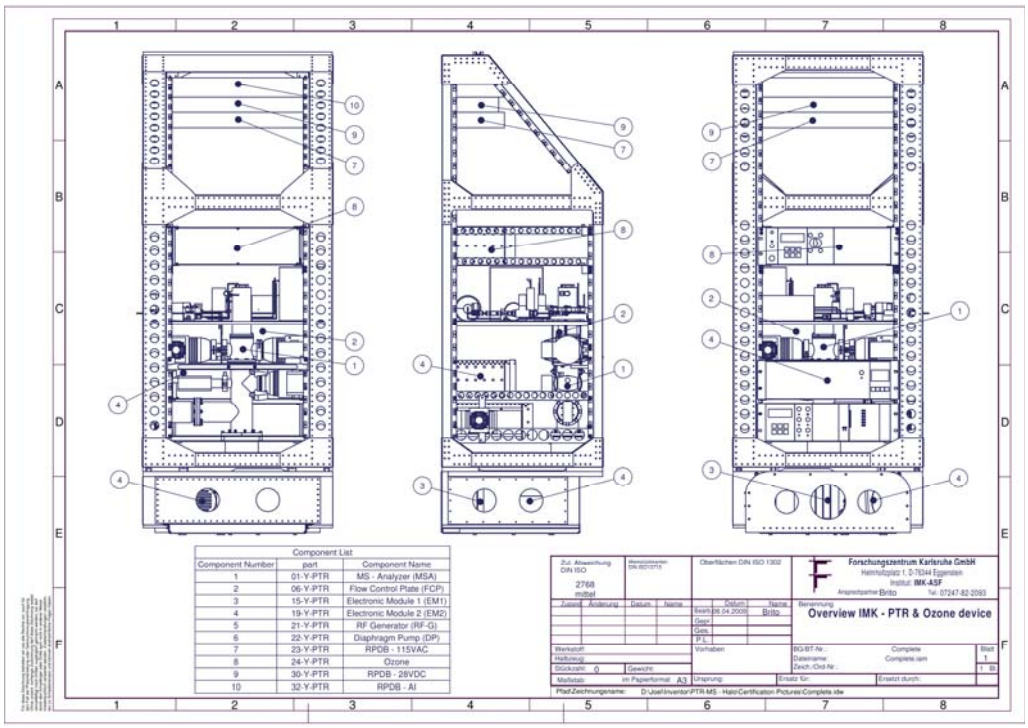

Figure 6.13: Example of system description for the HALO certification process.

6.3.4 Future improvements

While the PTR-IF-MS exceeds original expectations as a lightweight high-sensitivity system, the application of the ion funnel enhanced drift tube presented here is only a first step towards a new path. In the following, possible applications of the new electrodynamic drift tube are discussed.

Weight/size reduction. The first versions of PTR-MS systems had a drift tube exit orifice of 0.6 mm. Due to amount of ion lost to the wall, this orifice was increased to 1.4 mm, strongly increasing system sensitivity [90]. This came, nevertheless, at the expense of a new vacuum stage and a third turbomolecular pump, leading to the system as known today. The ion funnel enhanced drift tube has the potential of a high transmission at the original (and even smaller) exit orifice diameter. Such achievement could potentially lead the system to, besides a higher sensitivity, a further (remarkable) weight/size reduction.

Separation of isobaric compounds. PTR-MS systems implemented with an ion trap (see Section 3.4.2) are able to separate between some isobaric species through collisional induced dissociation (CID). This arises assuming different compounds show different fragmentation patterns. Such technique has been only briefly exploited using the standard PTR-MS drift tube [72]. The declustering effect via RF voltage demonstrated here is expected to strongly increase with the next RF voltage supply (under development), which could lead to the separation of isobaric compounds through CID.

Mass filtering. The low mass cut-off, shown as an issue to be tackled on the application described here, has an interesting potential within PTR-IF-MS. Page et al. has published low mass filtering in ion funnel systems by applying a given voltage to the exit plate [216]. However, such filtering could be achievable in different regions of the electrodynamic drift tube by varying the distance between electrodes, thus having a low mass cut-off prior to the end plate. As such, low masses could be filtered previous to CID analysis, e.g. on acetone/propanal analysis, all ions with m/z <50 could be previously filtered, leading to more accurate results. When measuring compounds not calibrated on-line, primary count could be assessed by removing the cut-off (i.e. increasing the frequency of RF voltage).

6.4 Conclusion

The PTR-IF-MS is a high-sensitivity, lightweight instrument for airborne deployment. The system is a result of lightweight construction achieving the unprecedented weight of 57 kg for chemical ionization (and PTR) mass spectrometers, usually above 120 kg. Furthermore, the system achieves limits of detection in the low pptv range, e.g. acetone has a LOD of 12 pptv for 5 s integration time and 4 pptv for 1 min.

The system is implemented with an unheated permeation device for continuous calibration (Chapter 4). Such calibration source is specially suitable for aircraft deployment. Furthermore, the system is implemented with an electrodynamic drift tube (Chapter 5), which led to an increase in system sensitivity of 30 %. Moreover, the implementation of a electrodynamic technique with the PTR-MS drift tube (here for the first time) shows a large potential, such as further weight reduction, separation of isobaric compounds and mass filtering. A resonant-based signal amplifier currently been manufactured shall enhance further the system sensitivity and allow to fully test the capabilities of this new technology. The description of the PTR-IF-MS in combination with Chapter 5 is currently being prepared for submission on a peer-reviewed journal.

Due to strong delay in the schedule of the HALO aircraft, the atmospheric analysis presented in the following Chapter has been performed with a strongly modified commercial PTR-MS deployed regularly in CARIBIC. This system, also from the TOP group at the IMK, has been recently implemented with developments part of the PTR-IF-MS system, e.g. the unheated permeation source.

Chapter 7

The correlation of acetone and CO in the upper troposphere

In this Chapter the correlation between two atmospheric pollutants is analysed, i.e. acetone (CH_3COCH_3) and carbon monoxide (CO). Both species are emitted at ground due to similar sources, including biomass burning and anthropogenic pollution (e.g. incomplete combustion) [45, 46, 217]. Consequently, depending on the source, both pollutants will have a certain emission rate (or enhancement ratio, $ER_{acet-CO}$), e.g. typically 4.6 pptv (pptv = 10^{-12} mol/mol) acetone / ppbv (ppbv = 10^{-9} mol/mol) carbon monoxide for biomass burning [218]. However, in the atmosphere, the $ER_{acet-CO}$ is expected to change from, firstly, different lifetimes and secondly, atmospheric in-situ production of both species, e.g. CH_3COCH_3 by oxidation of C_3-C_5 isoalkanes [46] and CO by oxidation of methane [219]. Therefore, the correlation of CH_3COCH_3 and CO contains information on their (largely common) sources as well as on their fate in the atmosphere or the chemical processing on their way to the sampling location (here, the upper troposphere). For a review on the role of VOCs in the atmosphere see Chapter 2.

Although a quite powerful parameter, only a few studies on the correlation of CH_3COCH_3 and CO have been published. This is primarily due to the difficulty of measuring acetone with high accuracy and at small scales, which is essentially only possible using chemical ionisation mass spectrometry, e.g. PTR-MS (Chapter 3).

The CARIBIC project (discussed next) measures regularly acetone and carbon monoxide in the upper troposphere, resulting in an extensive and powerful dataset. The PTR-MS regularly deployed in the CARIBIC passenger aircraft project is also from the TOP group at the IMK and, moreover, has been implemented recently with some of new features described in this work such as the peek-bodied proportional valve

and the unheated permeation source.

The study presented here is firstly performed in a case study, followed by the whole CARIBIC dataset, allowing a seasonal and latitudinal correlation variation study.

7.1 The CARIBIC project

The CARIBIC (**C**ivil **A**ircraft for the **R**egular **I**nvestigation of the atmosphere **B**ased on an **I**nstrument **C**ontainer) project uses an airfreight container, which is equipped with automated instruments for the measurement of trace gases and aerosol particles onboard a passenger aircraft (Fig. 7.1).

The CARIBIC is a European project with 12 partners from 6 countries. It is largely financed by the participant institutes and is/was embedded in various nationals and European projects (e.g. AFO 2000 from the German Federal Ministry of Education and Research, CARIBIC I-III and GEOMON from the EU). It is a unique project worldwide, one of the three existing projects using passenger aircraft for atmospheric research [220–223].

In contrast to short-term research aircraft campaigns (typically 2–6 weeks), CARIBIC measures regularly since 1997, which allows to collect representative data and to infer seasonal and for some species, even inter-annual variations and long-term trends. Moreover, by using a long-endurance, large aircraft, CARIBIC covers large parts of the globe at a cost-effective manner (typically 300 € per measurement hour in comparison to, currently estimated, 12 500 € for HALO).

As of May 2005, the CARIBIC container is installed once a month for four consecutive long-distance flights, shown in Fig. 7.2. The container (Fig. 7.3) weights 1.6 ton and currently contains 15 instruments (5 from TOP-IMK), measuring altogether ∼100 trace gases and aerosol particles. The container approach allows to deploy state-of-the-art instruments with high measurement accuracy and to exchange/improve/add instruments on time periods of 1–5 years.

7.1.1 Experimental

Acetone (as well as many other VOCs) are detected using a strongly modified PTR-MS instrument purchased in 2002 from Ionicon Analytik (Innsbruck, Austria – see Chapter 3). The modifications include automation for on-line measurement and a calibration system with high-pressurized bottles. More recently, developments described in Chapter 4 (calibration source) and Chapter 6 (e.g. gas flow design) have been integrated in

Figure 7.1: Lufthansa Airbus A340-600 and CARIBIC air inlet in closer view.

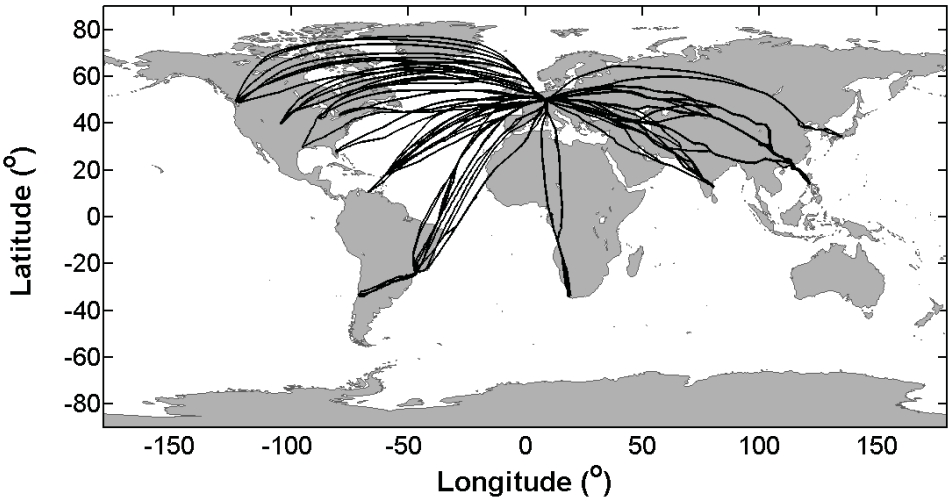

Figure 7.2: 210 CARIBIC flights from the studied period (2005 - 2010).

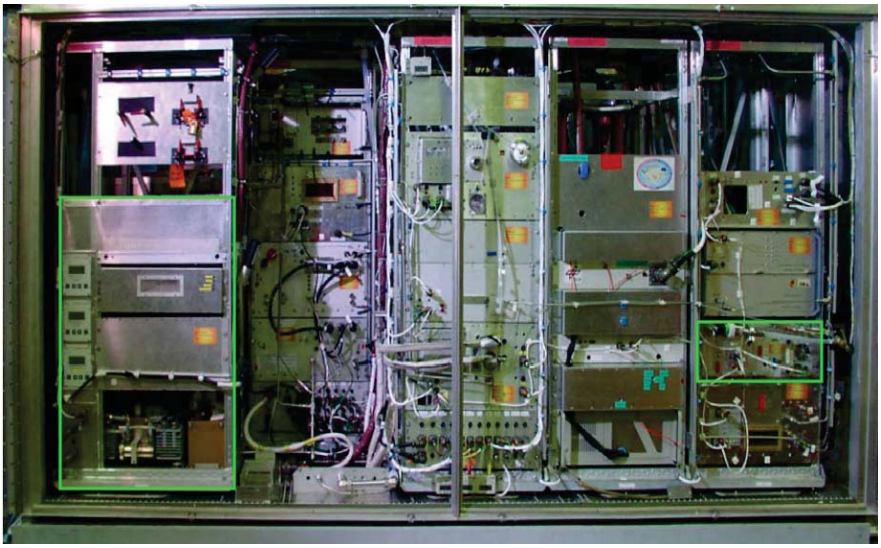

Figure 7.3: 1.6 ton container with, currently, 15 instruments for in-situ measurement. PTR-MS location is indicated by the box on the left side. The CO instrument is on the right side.

the CARIBIC PTR-MS, decreasing its weight to 90 kg + 20 kg rack. The system yields a detection limit with 5 s resolution of 25 pptv for acetone

The CO analyser is based on a commercial instrument (Model AL 5002, Aero-Laser, Garmisch-Partenkirchen, Germany). The system has a time resolution of 5 s and an uncertainty typically of 1.9 % or 1 ppbv, whichever is greater [36].

7.2 Dataset description

The correlation study presented here is limited to tropospheric air. Stratospheric air data is identified according to a chemical tropopause definition proposed by Zahn and Brenninkmeijer [224]. Such definition arises from 5-year measurements onboard the CARIBIC aircraft (during phase I - prior inclusion of the PTR-MS) and states that all air masses showing an ozone mixing ratio above the threshold value (O_3^{TP}) are identified as stratospheric:

$$O_3^{TP} = 97 + 26 \sin\left(2\pi \frac{doy - 30}{365}\right) \tag{7.1}$$

where the O_3^{TP} is given in ppbv and *doy* is day of year.

A typical flight is depicted in Fig. 7.4, indicating that the tropopause is crossed a few times. A closer view of the acetone and carbon monoxide sampled during this flight indicates a strong correlation between them, shown in Fig. 7.5. There, two distinct

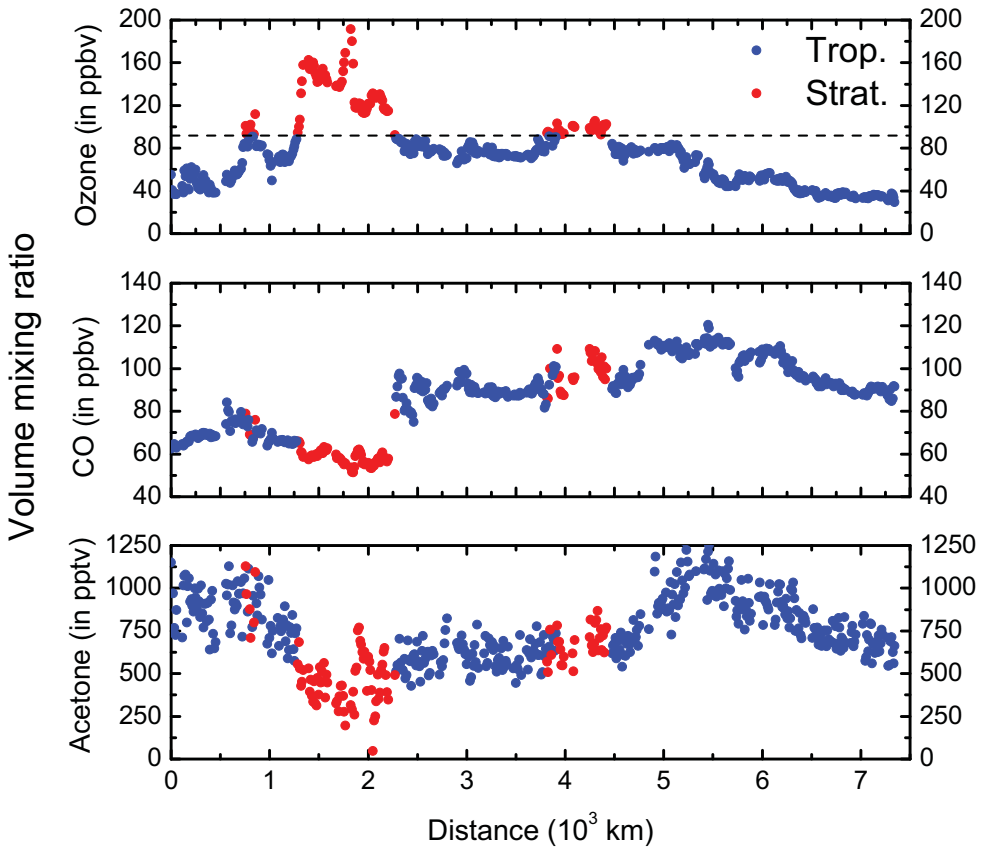

Figure 7.4: Flight 244 from August 13$^{\text{th}}$, 2008 from Frankfurt to Chennai. In blue: Measurement in tropospheric air. In red: Measurement in stratospheric air. Dashed line: Ozone threshold for tropospheric air according to the chemical definition of the tropopause (Eq. 7.1).

patterns can be observed identified with a circle and a line. The former, characterised by a weak correlation, was sampled over Europe but was originated in the gulf of Mexico, confirming the weak correlation for biogenic emissions [130]. The latter originates from China and Russia, strongly influenced by anthropogenic emissions. The correlation slope of 22.5 pptv acetone / ppbv carbon monoxide matches previous observations in the free-troposphere [130]. As indicated in Fig. 7.5, care must be taken to separate among different air masses for a meaningful analysis. Therefore we propose the following analysis for measurements sampling through long distances.

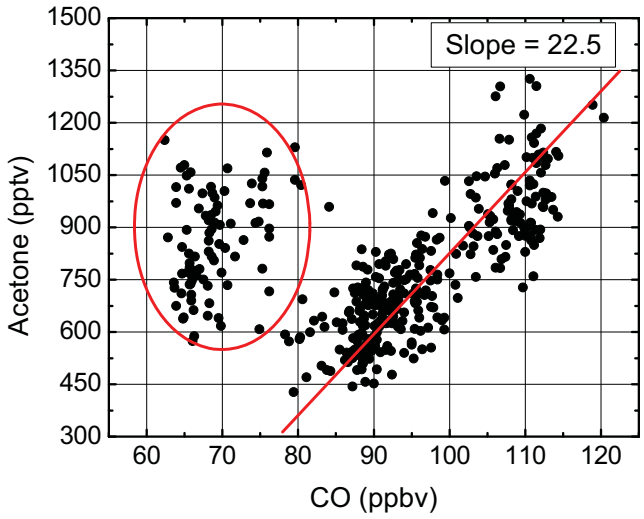

Figure 7.5: Acetone and carbon monoxide measured during the flight 244 from Frankfurt to Chennai, depicted in Fig. 7.4. Red circle indicates possible air sampled with strong biogenic influence. Line indicates measured correlation between acetone and carbon monoxide with a slope (or enhancement ratio, $ER_{acet-CO}$) of 22.5 pptv acetone / ppbv carbon monoxide.

Firstly, the flight track is split in defined length sections. For every flight section, a linear fit on the correlation data is performed. Then, data from a given flight section is analysed relative to its correlation R^2 (among others, more below), ensuring only confirmed correlations are considered. Finally, a $ER_{acet-CO}$ distribution analysis according to season and sampling latitude is performed. As such, this method readily yields an overview on upper tropospheric correlation variability.

Four criteria have been devised to include a given $ER_{acet-CO}$ in the distribution analysis: (i) The flight section data must have at least five points. (ii) The R^2 of a linear fit must be higher than 0.15. (iii) The CO mixing ratio span of at least 10 ppbv.

(iv) The distance between first and last measurement position is limited to 300 km. The latter limits the amount of data in a single correlation to roughly 20 points, at usual flight velocity of 1 000 km h^{-1}.

The maximal section distance for long-range measurements is a trade-off between number of points (more reliable linear fit) and the focus into single air masses. The standard deviation of set of $ER_{acet-CO}$ for latitude/season was minimized for section lengths between 75 and 2000 km, yielding 300 km as optimum.

7.2.1 Airmass characterisation

Due to possibly large differences between sampled air latitude origin and sampled latitude, the 5-day back-trajectory of sampled air masses has been considered. The trajectories are available for each CARIBIC flight, calculated with the KNMI (Royal Netherlands Meteorological Institute) trajectory model TRAJKS [225].

For every 3 minutes of flight a 5-day backward trajectory is calculated using the horizontal and vertical wind components from the ECMWF (European Centre for Medium-Range Weather Forecasts) model. The wind fields are given on the hybrid sigma-pressure ECMWF model levels at a 1×1 degree horizontal resolution. Fig. 7.6 shows an example of flight track latitude and air mass 5-day backwards trajectory latitude.

Besides backward trajectory latitude, air masses have been categorized as well according to its potential temperature. It has been previously proposed that potential temperature could serve as indicator for air mass original latitude [226]. Such relationship is expanded based on 5-days backward trajectories. Fig. 7.7 shows correlation of the dataset potential temperature with sampling latitude and the potential temperature with 5-day backward trajectory latitude.

A seasonal/latitudinal correction factor has been considered for potential temperature (θ in K) [226]:

$$\theta_{cor} = \theta + \alpha \cdot \sin\left(2\pi \frac{doy - 105}{365}\right) \tag{7.2}$$

where α is a term dependent of latitude Φ in degrees:

$$\alpha = \begin{cases} 5 - \Phi/2 & \text{if } \Phi < 50° \\ -20 & \text{if } \Phi > 50° \end{cases}$$

Using linear fit results shown in Fig. 7.7, the following correlation between potential

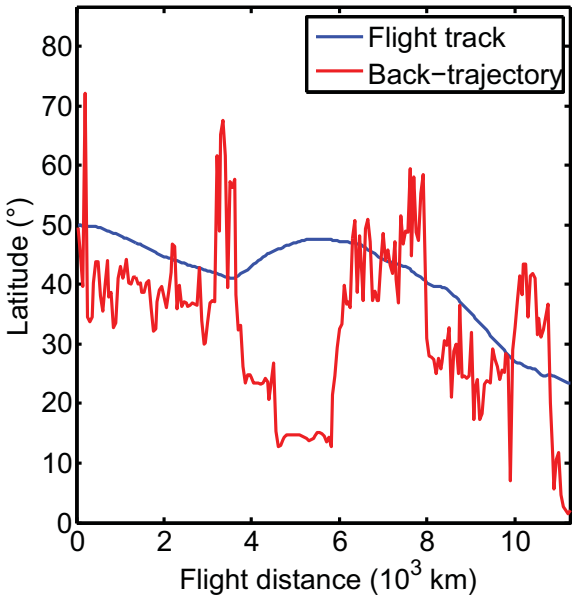

Figure 7.6: Sampling and air mass 5-day backwards trajectory latitude of flight 244 from Frankfurt, Germany to Chennai, India. Strong difference between sampling latitude and 5-days backwards trajectory motivates the inclusion of the latter in the analysis.

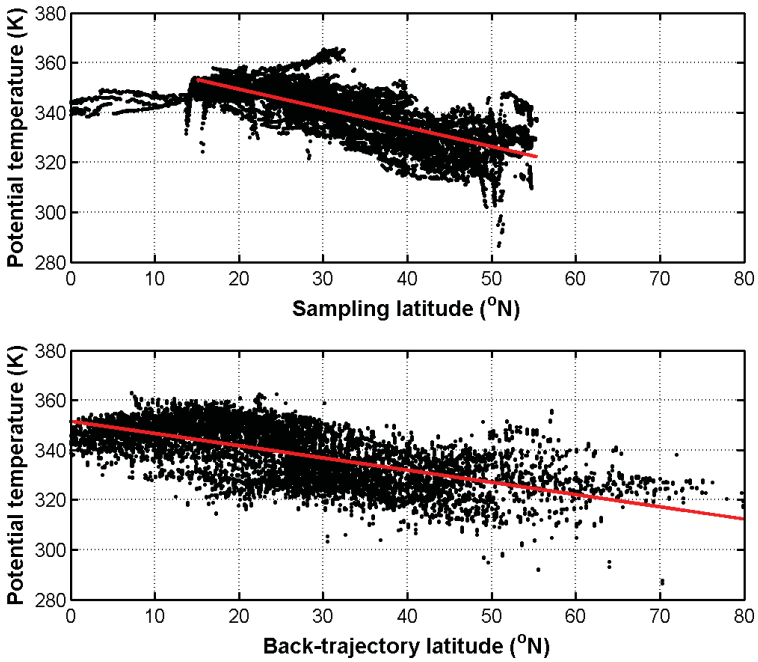

Figure 7.7: Top: Correlation between potential temperature and sampling latitude. Linear fit between 15 ° and 55° north. Bottom: Correlation between potential temperature and 5-day backwards trajectory latitude based on the ECMWF model.

temperature and air mass latitude has been used in this work:

Table 7.1: Potential temperature and corresponding latitude obtained from 5-days back-trajectory.

θ (K)	352	345	337	330	322
Φ (°)	0	15	30	45	60

7.3 Results

The analysis tool presented here is intended to enhance analysis capabilities of data within CARIBIC. Firstly, correlation results have been obtained in a case study, thereafter expanded to the whole CARIBIC dataset.

7.3.1 Case study

The flight 238, from June 2008, has been chosen for the case study due to high amounts of acetonitrile (CH_3CN) and well-pronounced peaks in the CO mixing ratios. As previously discussed, the former is a well-known marker for biomass burning and the latter for anthropogenic emissions (incomplete combustion and biomass burning). The region sampled with tropospheric air spans from Chennai, India to the border of Iran and Turkey, shown in Fig. 7.8.

The measurement and correlation results are shown in Fig. 7.9, indicating a decrease in the correlation slope ($ER_{acet-CO}$) with increasing sampling latitude. Three events (marked with a number in Fig. 7.9) were chosen to be analysed with respect to the 5-days backwards trajectory, depicted in Fig. 7.10. The selected events are the following: (I) A pronounced valley in acetone and CO mixing ratios with back trajectories shown in green. (II) A peak in acetone, acetonitrile and CO mixing ratios with back-trajectories shown in red. (III) A pronounced peak in acetone mixing ratio, not followed by CO, with back-trajectories shown in blue.

According to results presented in Fig. 7.10, event (I), shown in green, was obtained while crossing an air mass originated from Saudi Arabia and crossing the north of Iran and the Iranian border with Afghanistan. Despite the strong change in the mixing ratios of the three species, the $ER_{acet-CO}$ parameter is roughly the same as in event (II). The air mass crossed during event (II), shown in red, is originated close to Bangladesh and China, crossing India prior sampling above Pakistan.

Event (III) was measured above India and most of the air mass originated from the northern part of India and Pakistan. The strong increase in acetone is not followed by

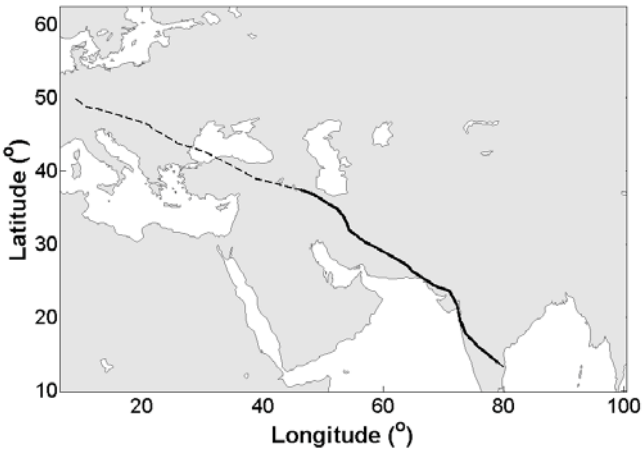

Figure 7.8: Flight 238 between Frankfurt, Germany and Chennai, India. Solid line indicates measurement of tropospheric air considered for this analysis. Dashed line: Measurement through stratospheric air or not considered.

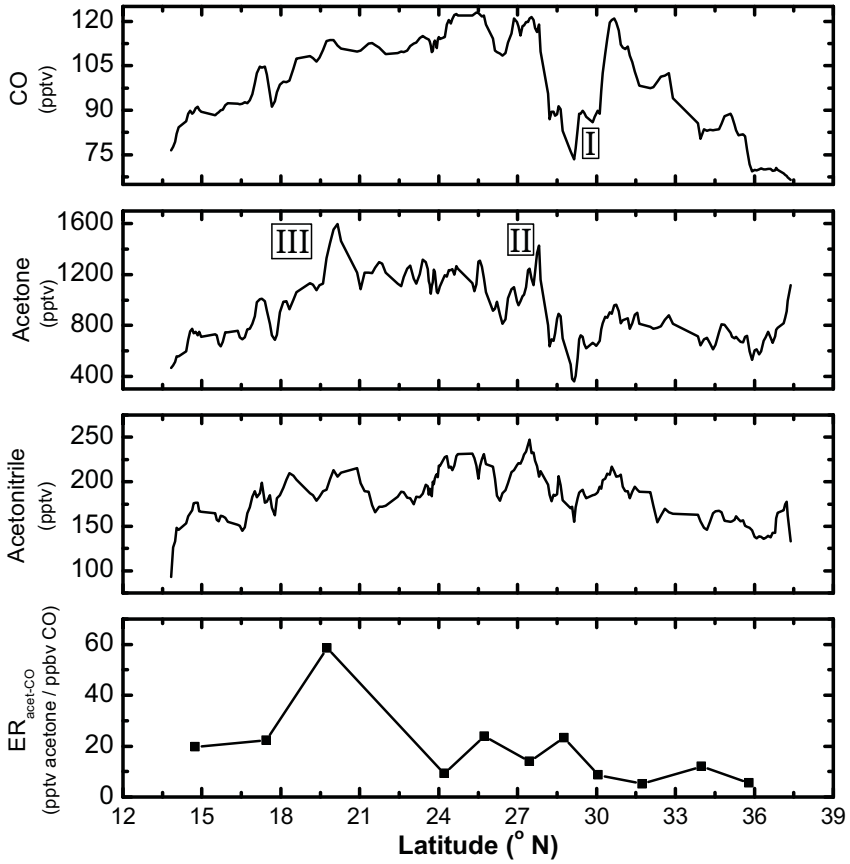

Figure 7.9: Correlation results for flight 238 between Frankfurt, Germany and Chennai, India. See text for analysis.

CO, leading to a $ER_{acet-CO}$ peak of 60 pptv acetone / ppbv carbon monoxide, possibly indicates biogenic source of acetone or in-situ production.

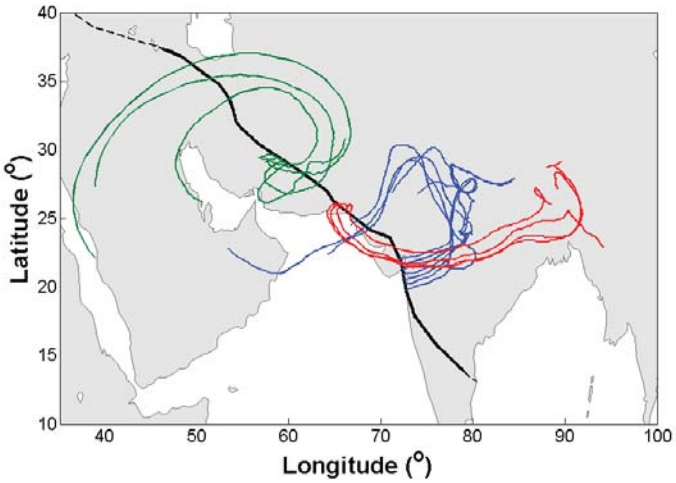

Figure 7.10: Track of flight 238 shown in Fig. 7.8 combined with 5-days backwards trajectory for selected events. Green line: back-trajectory for event I. Red line: back-trajectory for event II. Blue line: back-trajectory for event III. See text for details.

7.3.2 Full dataset

During the studied period, 99 flights were performed where acetone and carbon monoxide have been measured. Following findings from Köppe et al. [227], seasonal study has been limited to summer/winter, where many of the spring/fall lights could be assigned to "end" seasons, increasing statistics. As a result, 281 000 km of summer/winter data at the upper troposphere / lower stratosphere (static pressure between 400 and 175 hPa) have been sampled in 69 flights. Flight set is listed at Table 7.2 and corresponding flight tracks are depicted in Fig. 7.11. In the flight set, the aircraft has sampled tropospheric air for 153 000 km, 72 000 km during summer flights and 81 000 km during winter flights.

A distribution analysis of the $ER_{acet-CO}$ from data gathered in the flights listed in Table 7.2 is depicted in Fig. 7.12. It includes data from 30° to 60° north 5-days back-trajectory latitude. Fig. 7.12 depicts the large standard deviation of the $ER_{acet-CO}$ value in the upper troposphere, specially for summertime measurements. This indicates a potentially large error if using carbon monoxide mixing ratios to retrieve the mixing ratio of acetone, as previously performed [228].

The $ER_{acet-CO}$ for the entire dataset is shown in Table 7.3. The data is separated in latitudes bins between 0° and 60°, with 15° intervals and season. Moreover, the

Table 7.2: Flight list with assigned season (S for summer and W for winter). Airport codes are Frankfurt(FRA), Sao Paulo (GRU), Santiago (SCL), Guagzhou (CAN), Manila (MNL), and Chennai (MAA).

#	Track	Date	Season	#	Track	Date	Season
138	FRA-GRU	20-02-06	W	194	FRA-CAN	21-06-07	S
140	SCL-GRU	21-02-06	W	196	MNL-CAN	22-06-07	S
141	GRU-FRA	21-02-06	W	197	CAN-FRA	22-06-07	S
150	FRA-CAN	29-05-06	S	198	FRA-CAN	17-07-07	S
151	CAN-MNL	30-05-06	S	199	CAN-MNL	18-07-07	S
152	MNL-CAN	30-05-06	S	202	FRA-CAN	14-08-07	S
153	CAN-FRA	30-05-06	S	203	CAN-MNL	15-08-07	S
154	FRA-CAN	05-07-06	S	204	MNL-CAN	15-08-07	S
157	CAN-FRA	06-07-06	S	205	CAN-FRA	15-08-07	S
158	FRA-CAN	31-07-06	S	210	FRA-CAN	24-10-07	W
159	CAN-MNL	01-08-06	S	211	CAN-MNL	25-10-07	W
160	MNL-CAN	01-08-06	S	212	MNL-CAN	25-10-07	W
161	CAN-FRA	01-08-06	S	213	CAN-FRA	25-10-07	W
166	FRA-CAN	19-10-06	W	214	FRA-CAN	13-11-07	W
167	CAN-MNL	20-10-06	W	215	CAN-MNL	14-11-07	W
168	MNL-CAN	20-10-06	W	216	MNL-CAN	14-11-07	W
169	CAN-FRA	20-10-06	W	220	FRA-CAN	25-02-08	W
170	FRA-CAN	14-11-06	W	221	CAN-MNL	26-02-08	W
171	CAN-MNL	15-11-06	W	222	MNL-CAN	26-02-08	W
172	MNL-CAN	15-11-06	W	223	CAN-FRA	26-02-08	W
173	CAN-FRA	15-11-06	W	224	FRA-CAN	26-03-08	W
174	FRA-CAN	13-12-06	W	225	CAN-MNL	27-03-08	W
175	CAN-MNL	14-12-06	W	226	MNL-CAN	27-03-08	W
176	MNL-CAN	14-12-06	W	227	CAN-FRA	27-03-08	W
177	CAN-FRA	14-12-06	W	237	MAA-FRA	18-06-08	S
179	CAN-MNL	06-02-07	W	238	FRA-MAA	19-06-08	S
181	CAN-FRA	06-02-07	W	239	MAA-FRA	19-06-08	S
182	FRA-CAN	06-03-07	W	244	FRA-MAA	13-08-08	S
183	CAN-MNL	07-03-07	W	245	MAA-FRA	13-08-08	S
184	MNL-CAN	07-03-07	W	246	FRA-MAA	14-08-08	S
185	CAN-FRA	07-03-07	W	247	MAA-FRA	14-08-08	S
190	FRA-CAN	22-05-07	S	258	FRA-MAA	11-12-08	W
191	CAN-MNL	23-05-07	S	259	MAA-FRA	11-12-08	W
192	MNL-CAN	23-05-07	S	260	MAA-FRA	21-12-08	W
193	CAN-FRA	23-05-07	S				

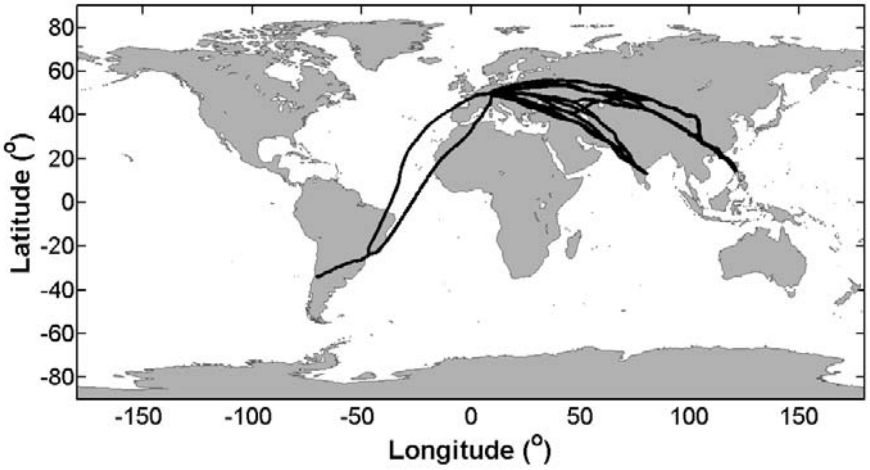

Figure 7.11: 69 CARIBIC flights where data used on this study was sampled. Flights between Frankfurt (Germany) and: São Paulo (Brazil), Santiago (Chile), Chennai (India), Manila (Philippines) with stop in Guangzhou (China).

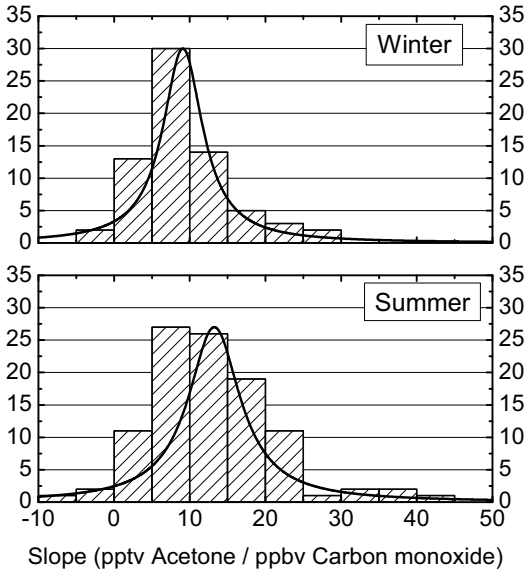

Figure 7.12: Distribution of $ER_{acet-CO}$ values for 5 days backwards trajectory latitude from 30° to 60° north. Results indicate relatively large variability, only observable with such long-term observation.

data is shown based on sampling latitude, 5-days backward trajectory and potential temperature.

Table 7.3: $ER_{acet-CO}$ in units of pptv acetone / ppbv carbon monoxide. Reported values are means from several slopes from same latitude and season. Standard deviation is indicated as error and number of slopes are indicated in parentheses.

		$ER_{acet-CO}$		
Season	Latitude (°)	Sampling	Back-traj	Pot. Temp.
Summer	0	12.7 ± 7.3 (4)	12.2 ± 7.2 (5)	12.8 ± 5.4 (73)
	15	14.0 ± 4.0 (16)	13.0 ± 4.8 (40)	11.2 ± 5.0 (29)
	30	11.6 ± 5.4 (72)	13.9 ± 6.9 (67)	18.8 ± 9.2 (8)
	45	20.2 ± 8.7 (36)	17.9 ± 10.9 (14)	22.8 ± 9.2 (17)
	60	–	33.9 ± – (1)	33.9 ± – (1)
Winter	0	–	7.6 ± 2.9 (17)	8.1 ± 2.5 (6)
	15	6.6 ± 2.7 (17)	6.8 ± 3.8 (27)	7.5 ± 2.8 (26)
	30	8.2 ± 3.3 (38)	11.3 ± 6.9 (28)	5.0 ± 2.0 (10)
	45	13.7 ± 8.0 (31)	11.5 ± 7.2 (9)	12.3 ± 6.5 (10)
	60	5.8 ± 1.4 (4)	16.5 ± 6.9 (7)	11.8 ± 8.1 (28)

Wintertime measurements show markedly lower correlation slopes as during summertime. Slopes grouped according the 5-days back-trajectory show an increase with latitude from (summer/winter) 12.2/7.6 pptv acetone / ppbv CO at the equator to 33.9/16.5 at 60°N. Using potential temperature based representative latitude yields (with a few exceptions) similar results, indicating the potential of such parameter applied to statistically significant datasets.

Considering ground sources and the shorter lifetime of acetone, the higher slope observed during summertime can be assumed to be the result of stronger convection. Such assumption would also lead to a decrease in slope with latitude. However, the opposite is observed, indicating the shorter lifetime of acetone due to photolysis in the tropics as in higher latitudes modulates overall behaviour of the correlation slope.

The study presented here will be expanded to comparison with models such as the ECHAM/MESSy Atmospheric Chemistry (EMAC) [229, 230] and the COSMO model in CLimate Mode (COSMO-CLM) [231, 232], besides inclusion of other species also measured in CARIBIC such as acetonitrile, a marker for biomass burning and propane, a precursor of acetone.

The correlation slopes presented here can be useful for model calculations, strongly

increasing statistics and providing a better assessment of the standard deviation. Inclusion of other compounds will allow better understanding on the chemistry in the UT.

Short-term measurements of such correlation provide a snapshot of the results presented here. Comparison with up-to-date published results of short-term measurements in the free troposphere are given in the next Section.

7.3.3 Assessment and comparison with literature.

Correlations found in literature between acetone and carbon monoxide in the upper troposphere are shown in Table 7.4.

Table 7.4: Published $ER_{acet-CO}$ in the free troposphere.

Campaign	Time	Location	Lat.[a]	$ER_{acet-CO}$	Ref.
LBA-CLAIRE	March 1998	Paramaribo, Surinam	0	19.5	[233]
INDOEX[b,c]	Feb/Mar 1999	Male, Maldives	0	3.4	[234]
STREAM98[b]	July 1998	Timmins, Canada	45	24.4	[130]
MINOS	July 2001	Crete, Greece	30	21.8	[130]
SAFARI 2000[d]	September 2000	Otavi, Namibia	15	8.1	[218]

[a] Approximated to latitude bins from Table 7.3.

[b] Upper troposphere only.

[c] Aged biomass burning plume.

[d] 2-hours old biomass burning plume measured at an altitude of 3.5 km.

The strong difference of result between the campaign of LBA-Claire (19.5 acetone pptv / CO ppbv) [233] and INDOEX (3.4 pptv/ppbv), a value 80 % smaller [234]. As CO mixing ratios were measured roughly comparable ranges (usually between 60 ppbv and 200 ppbv) acetone changed quite strongly. During LBA-Claire and STREAM98 values up to 4 000 pptv were observed whereas during INDOEX maximum reported acetone mixing ratio was 800 pptv. Here, mixing ratio of acetone was not observed above 1 800 pptv, including all latitudes and seasons.

7.4 Conclusions

The correlation between acetone and carbon monoxide, previously studied only in case studies, can be a strong parameter in an atmospheric chemistry analysis. The CARIBIC project, deploying many instruments regularly in long-distance flights allows case studies, as well as a broad overview of the atmosphere, including seasonal analysis.

The use of potential temperature based representative latitude leads to satisfactory results. Nevertheless, large scattering allows its use only in a statistically significant dataset. Correlation depending on season and latitude. Large variability of correlations in the tropopause, therefore use of CO and correlation factor as acetone mixing ratio estimation on box model calculation must taken in account such large variability.

The knowledge gathered throughout the development of the PTR-IF-MS (Chapter 6) has been largely applied to the PTR-MS system deployed within CARIBIC. The resulting sensitivity increase is expect to enhance system precision (e.g. for acetonitrile measurements) or allow an increase in temporal resolution.

The results obtained here will be compared with the climate models EMAC and the COSMO-CLM, and furthermore, compounds also measured in CARIBIC, such as propane, an important acetone precursor, shall be added to the analysis.

Chapter 8

Summary and Outlook

In this thesis we present a new high-sensitivity PTR-MS system for airborne deployment, entitled PTR-IF-MS. Extremely lightweight, the system has two notable new features, an ion funnel enhanced drift tube and a novel type of calibration system which is especially suitable for aircraft deployment. Besides instrumental development, we present as well a study of the correlation between acetone and carbon monoxide in the upper troposphere. The data from the passenger aircraft based project CARIBIC, gathered regularly in long distance flights, allows the first long-term correlation analysis between both species. In the following, an overview of this work is given.

Chapter 2 reviews the role of VOCs in the atmosphere, its main groups, reactions and budget. VOCs constitute powerful tracers for studying atmospheric chemistry and for validating chemical transport models. PTR-MS technology allows fast and accurate measurements of many VOCs in air with a high sensitivity. A complete description of PTR-MS technology, including its most noteworthy variations, is presented in Chapter 3.

The development of scientific instruments for deployment onboard research aircrafts is constantly accompanied by a strong weight restriction. As such, strong effort has been made throughout the development of the PTR-IF-MS to achieve an unprecedented portability among chemical ionization (and PTR) mass spectrometers. One crucial development in this respect was the unheated permeation source for continuous calibration of the PTR-IF-MS (Chapter 4).

VOC calibration is usually performed using a high-pressurized gas cylinder or a permeation device. While the latter is significantly more suitable for aircraft deployment, being much lighter and not pressurized, it is rarely used during airborne measurements. This arises from the long stabilization time (from hours up to days). After a period

without temperature control (i.e. power-down during transport or aircraft fuelling), the permeation system do not provide accurate calibration until equilibrium is once again reached. Our newly developed calibration device overcomes these drawbacks. By making use of a very small and thin PTFE membrane, an extremely short equilibration time of 18 min has been achieved. As the permeation device is combined with a water reservoir as heat buffer and enclosed in an excellent insulation, we have strongly decreased the temperature drift of the calibration system below 0.3 K/h. The result of these two achievements is a permeation device that yields a permeation rate as a function of an uncontrolled, but accurately measured, temperature. No stabilization time is required prior to system calibration. The complete calibration system (including a venting system) weights less than 3 kg.

State-of-the-art PTR-MS systems have a high-sensitivity which ensures accurate measurements in most applications. Nevertheless, fast (e.g. airborne) measurements at very low mixing ratios, in the pptv-range, may still present large uncertainties. Chapter 5 details an effort to further increase the system sensitivity. Ion trajectory simulations indicate that the ion transmission in the drift tube is below ∼10 %. Due to the high number of collisions along the drift tube, ions tend to drift away from the centre axis, leading to such large ion lost. To minimize such effect we have developed an ion funnel enhanced drift tube. The electrodynamic ion funnel is the only technology capable of focusing an ion batch under strong gas dynamics. Up-to-date, ion funnel technology has been mostly applied with ion mobility mass spectrometers, leading to a well characterised behaviour for relatively slow, "heavy" ions ($m/z > 500$). Here, the electrodynamic ion funnel is used for the first time to focus light ions ($19 < m/z < 150$).

Besides ion focusing, the ion funnel is capable of strongly increasing the kinetic energy of the ions (via RF field), thus allowing the decrease of the drift velocity. As such, the use of an electrodynamic technique in the drift tube allows to enhance the drift and thus reaction time, which directly increases the system sensitivity. The potential of this new drift tube is shown by increasing the system sensitivity by 30 %. The next generation (using resonance based signal amplifier) is currently being manufactured and shall lead to a further sensitivity enhancement.

The PTR-IF-MS system is described in Chapter 6. The system has been developed according to the HALO aircraft certification guidelines, including the required electrical and gas flow specifications and the demands concerning mechanical construction and materials. With comparable sensitivity of state-of-the-art systems, the PTR-IF-MS is the lightest high-sensitivity PTR-MS worldwide (only 57 kg, in comparison with

standard 120 kg). Its limit of detection (LOD) for usual VOCs is in the low pptv range, e.g. LOD for acetone is 15 pptv for 5 s measurement time and ∼4 pptv in 1 min integration time.

Simulation and calculation results indicate that, with the new resonance based signal amplifier, the increase in oscillation energy shall double the current system sensitivity. Moreover, an increase of ion transmission due to a more efficient ion focusing is expected to increase sensitivity by roughly a factor 5, strongly exceeding any published PTR-MS system.

Chapter 7 presents a study on the correlation between acetone and carbon monoxide in the upper troposphere. Such correlation has been previously studied in short-term campaigns onboard research aircrafts, where results have been used for analysis of oceanic sink/emission of acetone, biomass burning plume chemistry and box model calculations. In contrast to such campaigns, in-situ measurement onboard CARIBIC represents a cost-effective manner to retrieve long-range and long-term UT/LS data. Besides covering large parts of the globe, such project allows to infer seasonal and for some species, even inter-annual variations and long-term trends. Acetone and carbon monoxide have been simultaneously sampled in tropospheric air for over 153 000 km during 69 flights. The analysis is limited to summer/winter flights.

The correlation between acetone and carbon monoxide has been analysed relative to its slope, or enhancement ratio ($ER_{acet-CO}$). Such parameter has been grouped for sampling latitude, 5-days backwards trajectory latitude provided from the ECMWF model, and a potential temperature based representative latitude. Wintertime measurements show markedly lower correlation slopes as during summertime. Slopes grouped according the 5-days back-trajectory show an increase with latitude from (summer/winter) 12.2/7.6 pptv acetone / ppbv CO at the equator to 33.9/16.5 at 60°N. Using potential temperature based representative latitude yields (with a few exceptions) similar results, indicating the potential of such parameter applied to statistically significant datasets.

Considering ground sources and the shorter lifetime of acetone, the higher slope observed during summertime can be assumed to be the result of stronger convection. However, such assumption would also lead to a decrease in slope with latitude, which is not observed, indicating that the shorter lifetime of acetone in the tropics due to photolysis dominates the correlation slope. The study presented here will be expanded to comparison with models such as the EMAC and the COSMO-CLM, besides inclusion of other species also measured in CARIBIC such as acetonitrile, a marker for biomass burning and propane, a precursor of acetone.

Appendix A

Ion production mechanism in the HCD ion source

The primary ions in a PTR-MS system (H_3O^+) are produced in a hollow cathode ion source, described in Section 3.2.1. The mechanism of the ion production can be better understood being separated in two parts, the glow discharge and the hollow cathode effect, each presented in the following [235].

A.1 Glow discharge

If the voltage difference between two planar electrodes, where the space between is filled with a neutral gas, is high enough that electrical breakdown occurs, a plasma, characterized as glow discharge will be formed. This plasma has at least eight different regions, as illustrated in Fig. A.1.

Consider an electron emitted from the cathode. Due to strong field, it is first accelerated, and when enough energy is reached, strong ionization with electron multiplication takes place. The two general regions in which these effects occur are known as the Aston dark space and the Cathode layer, respectively.

Farther from the cathode, the field becomes weaker and only fast electrons which have not lost energy by inelastic collisions are able to ionize in the region known as the cathode dark space. The next boundary is between the cathode dark space and the negative glow, where exists a small potential barrier, overcome by a large number of electrons. In this boundary, the number of electrons has increased considerably due to ionization of neutrals, as well as, naturally, a large number of positive ions. The positive ions, as well as metastable atoms, fast unexcited atoms, and intense UV

A. ION PRODUCTION MECHANISM IN THE HCD ION SOURCE

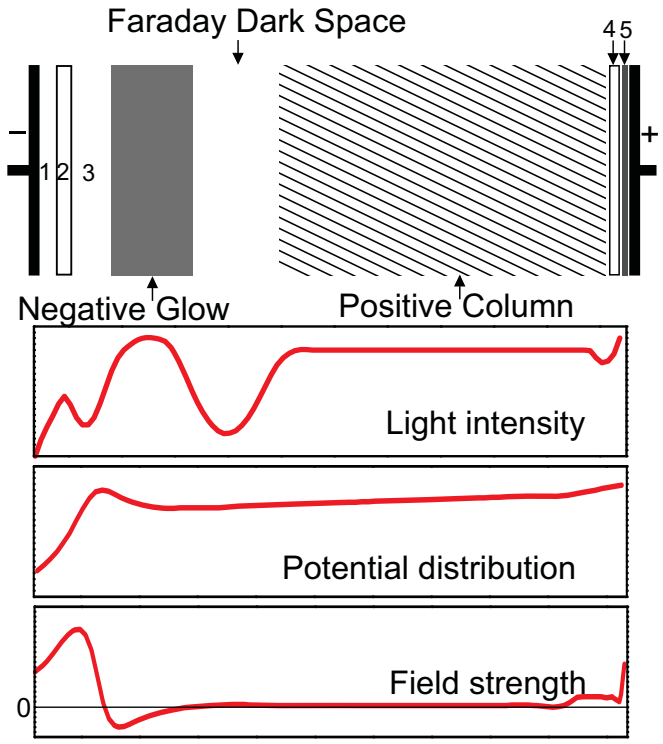

Figure A.1: Different layers inside the hollow cathode source, its light emission intensity and potential distribution. From the left: Cathode; 1:Aston dark space; 2:Cathode layer; 3:Cathode dark space; Negative glow ; Faraday dark space; Positive Column, 4:Anode dark space; 5:Anode glow; Anode.

radiation impinge on the cathode, causing the emission of secondary electrons. Under steady-state conditions (i.e., a self-sustaining discharge) each electron emitted by the cathode must produce a sufficient number of ionizations and excitations to effect the release of one further electron from the cathode.

At this point, electrons entering the negative glow can be separated in two different groups: (1) those produced at or near the cathode which are fast, and have not suffered energy loss by collision; and (2) those created in the cathode dark space, which are slow as a result of many inelastic collisions. The slow electrons normally do not have enough energy to perform ionization, however, usually enough for excitation, producing the characteristic negative glow as they undergo many collisions. The fast electrons penetrate farther and dissipate their energy in many inelastic collisions, producing both ionization and excitation.

The motion of the electrons prior to entering the negative glow is beam like. However, all beam properties are lost in the negative glow, where the motion of the electrons becomes random. Their energy decreases with distance into the negative glow, and recombination with positive ions can take place. With farther increasing distance from the cathode, the field rises slowly, the probability of recombination decreases, and the Faraday dark space develops. Its properties are intermediate between those of the negative zones and positive column. Electrons are pulled out of the negative glow by this weak field and may gain sufficient random energy to excite and ionize atoms.

At this point the positive column develops. The electric field is constant (see Fig. A.1) in the positive column so that, at any point, the concentrations of electrons and positive ions are equal. The electrons, because of their greater mobility, carry practically all the discharge current. Ionization is not obtained from the drift velocity of the electrons in the field direction, but rather from the large random velocity acquired by many elastic collisions in the electric field. At the anode side of the positive column, the electrons are attracted toward the positively charged anode, the positive ions repelled, and a negative space charge is formed. This gives rise to the anode fall. An electron emerging from the positive column enters the anode fall region with a small initial energy and is accelerated towards the anode. After crossing the anode dark space, it has acquired sufficient energy to excite and ionize the gas in front of the anode (the anode glow). It is important to note that most of the potential drop across the electrodes is located in the cathode dark space, where the field strength is at a maximum.

Depending on the allowed discharge current, different patterns (or voltage-current regions) are observed on the HCD. Fig. A.2 shows the schematic characteristic of a self-sustaining discharge. From nA range up to fraction of mA lays the Townsend and

Transition discharge, regions of little interest in the PTR-MS due to small ion production. Further increasing the current, a normal glow discharge pattern is reached, where the voltage remains constant as the current is changed by some orders of magnitude. In the other hand the area occupied by the glow between the electrodes will increase with current, until the effective area of the cathode is fully covered. By then, a further increase of current will force a larger cathode fall, and, thus, potential rises. This is the region of the abnormal glow discharge.

As the current increases further, the potential reaches a maximum and begins to decrease. The cathode at these high current densities has become so hot that secondary electron emission from the cathode becomes increasingly supplemented by thermionic emission. This is an ill-defined transition region where both processes are operative. At still higher currents, secondary electron emission becomes of little or no influence and the discharge acquires the characteristics of an arc. The abnormal glow discharge region is generally considered to end where thermal emission of electrons from the cathode becomes significant.

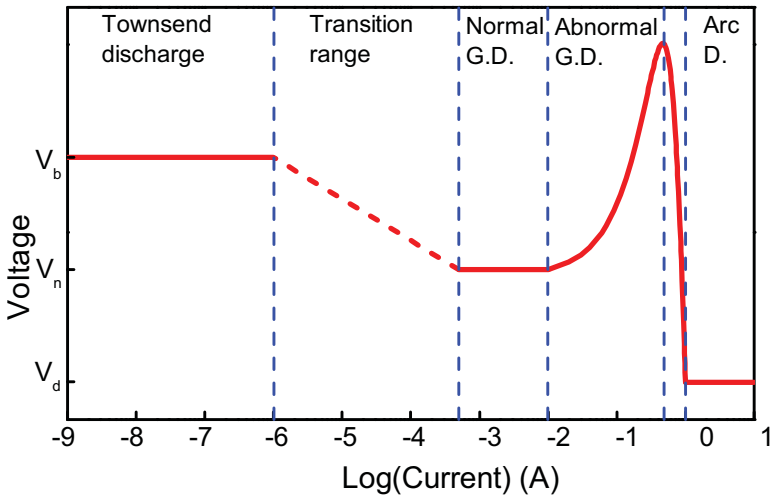

Figure A.2: Voltage-current characteristics of a self-sustaining gas discharge (voltage on a linear and current on a logarithmic scale): Vb: breakdown voltage, Vn: normal cathode fall, and Vd: arc voltage .

A.2 The hollow cathode effect

Due to the beam like nature of the electrons emerging from the cathode dark space, the position of the negative glow is determined by the spatial orientation of the cathode. The hollow cathode effect is best understood by considering two planar parallel cathodes

having a common anode perpendicular to their axis. The electron beams from the two cathodes are then in opposite directions. At large intercathode distances, the two cathodes behave essentially independently of each other, and the two negative glows are separated and well characterized. For a fixed potential, as the intercathode distance is reduced, the two negative glows begin to merge and finally coalesce (Fig. A.3). As this occurs, the current density rises sharply reaching values 10^2 to 10^3 times larger than in a normal glow discharge for the same cathode fall. Simultaneously, the light emitted from the negative glow increases dramatically. The net result of the coalescence of the negative glows is known as the hollow cathode effect.

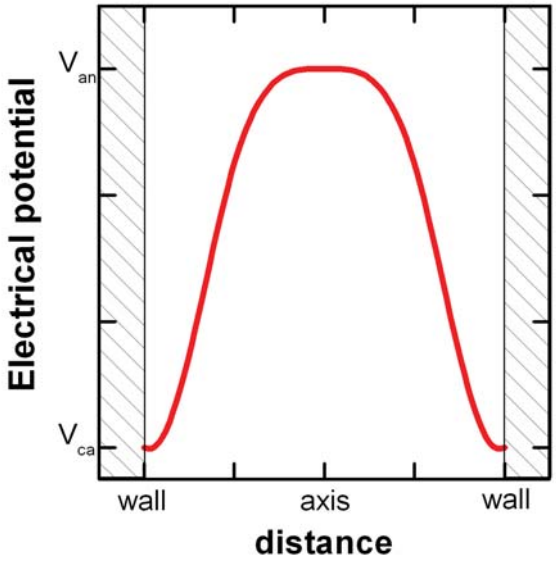

Figure A.3: Schematic view of hollow cathode effect.

The reason that the discharge occurs chiefly between the plane cathodes rather than to their exterior surfaces becomes clear with the following consideration. At the pressures normally used ($<$ 10 Torr), the mean free path of the electrons leaving the inner wall of the cathode is sufficiently large that the electrons can penetrate the positive space charge region of the opposite cathode. The attendant reduction of this space charge causes an increased current and a lower cathode fall. This condition permits a much greater current density from the inner cathode walls than from the outer, and the discharge thus occurs mainly between the plane cathodes. For a given cathode fall, electrons entering the negative glow must release their energy there in ionizing and

exciting collisions, since they cannot advance into the retarding field of the opposite cathode. The HCD has a dark space thickness much less than that for a normal glow discharge, and the negative glow is nearly field free and potential is comparable with anode, as depicted in Fig. A.3. Instead of two plane cathodes, a cylindrical cathode, closed at one end, is usually employed for hollow cathode studies, as well as in the PTR-MS ion source.

Appendix B

Quadrupole mass filtering

This Appendix complements the quadrupole system description given in Section 3.4.1. In the following, the mass filtering capabilities of a quadrupole system is presented.

B.1 Mass filtering and stability regions

Ideally, the rods of a quadrupole are hyperbolic (see Fig. B.1), however circular rods are easier to be manufactured with the required precision, providing an adequate approximation to hyperbolas.

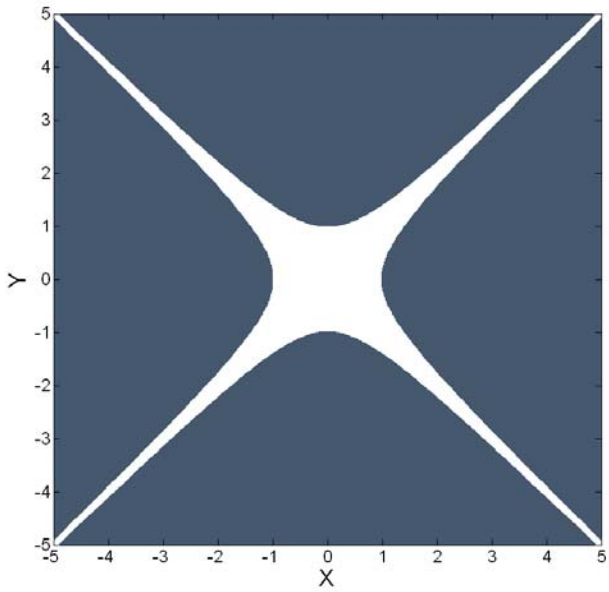

Figure B.1: Ideal hyperbolic shape of quadrupole rods.

Following the hyperbolic geometry, the potential $\Phi(x, y)$ at any point inside the quadrupole is described by:

$$\Phi(x, y, t) = \frac{x^2 - y^2}{r_0^2}\Phi(t) \tag{B.1}$$

where x and y are Cartesian coordinates. The parameter r_0, called "field radius", is the distance from the centre of the quadrupole to any rod. The potential $\Phi(t)$ is given by

$$\Phi(t) = U - V_{\mathrm{RF}} cos(\Omega t) \tag{B.2}$$

where U is the DC voltage, $_{\mathrm{RF}}$ is the zero-to-peak amplitude of the RF voltage applied from each quadrupole rod to ground, Ω is the angular frequency of the RF voltage and t is time.

The ion motion is determined by Newton's law:

$$\vec{f} = m\frac{d\vec{v}}{dt} \tag{B.3}$$

where $\vec{f}$ is the force on an ion, m is the mass of the ion, and $\vec{v}$ is the ion velocity. The force on a positive ion is

$$\vec{f} = -z \cdot e \cdot \nabla\Phi(x, y, t) \tag{B.4}$$

where z is the number of charges on the ion and e is the elementary charge. The electric field in the x direction is:

$$E_x = -\frac{\partial\Phi(x, y, t)}{\partial x} = -\frac{2x}{r_0^2}(U - V_{\mathrm{RF}} cos(\Omega t)) \tag{B.5}$$

and in the y direction:

$$E_y = -\frac{\partial\Phi(x, y, t)}{\partial y} = -\frac{2y}{r_0^2}(U - V_{\mathrm{RF}} cos(\Omega t)) \tag{B.6}$$

Given the independence of E_x in the y coordinate and vice-versa, each direction can be considered alone. As such, the equation of motion for the x and y directions can be written as:

$$\ddot{x} + \frac{2 \cdot z \cdot e}{m \cdot r_0^2}(U - V_{\mathrm{RF}} cos(\Omega t))x = 0 \tag{B.7}$$

$$\ddot{y} - \frac{2 \cdot z \cdot e}{m \cdot r_0^2}(U - V_{\mathrm{RF}} cos(\Omega t))y = 0 \tag{B.8}$$

where $\ddot{x} = \frac{\mathrm{d}^2x}{\mathrm{d}t^2}$ and $\ddot{y} = \frac{\mathrm{d}^2y}{\mathrm{d}t^2}$. These equations can be rewritten in a form of Mathieu equation [236]:

$$\frac{d^2u}{d\xi^2} + (a_u - 2q_u cos(2\xi))u = 0 \tag{B.9}$$

$$\xi = \frac{\Omega t}{2} \qquad u = x \text{ or } y \tag{B.10}$$

where a and q are:

$$a_x = -a_y = \frac{8z \cdot e \cdot U}{m \cdot r_0^2 \cdot \Omega^2} \qquad q_x = -q_y = \frac{4z \cdot e \cdot V_{\mathrm{RF}}}{m \cdot r_0^2 \cdot \Omega^2} \tag{B.11}$$

Solutions to Mathieu equations yield [237]:

$$u(\xi) = \alpha' e^{\mu\xi} \sum_{n=-\infty}^{\infty} C_{2n} e^{2n \cdot i \cdot \xi} + \alpha'' e^{-\mu\xi} \sum_{n=-\infty}^{\infty} C_{2n} e^{-2n \cdot i \cdot \xi} \tag{B.12}$$

where α' and α'' are integration constants depending on the initial position u_0 and initial radial velocity $\dot{u_0}$. The constants C_{2n} and μ depend only on the a and q values. Therefore the ion motion is determined by the (a,q) values, regardless of the initial conditions.

A closer look in Eq. B.12 shows two families of solutions, stable and unstable. Stable solutions arise if μ is imaginary ($\mu = i\beta$) and β is not an integer. In this case the ions oscillate in the x-y plane with limited amplitudes and pass through the quadrupole field. Integer values of β form a series of solutions, which are periodic and unstable. As such, ion amplitudes grow exponentially in the x, y or in both directions, leading to ion lost. Substituting $\mu = i\beta$ into Eq. B.12 and simplifying it gives the equation of motion for stable ions:

$$u(\xi) = A \sum_{n=-\infty}^{\infty} C_{2n} cos(2n + \beta)\xi + B \sum_{n=-\infty}^{\infty} C_{2n} sin(2n + \beta)\xi \tag{B.13}$$

where $A = \alpha' + \alpha''$ and $B = i(\alpha' + \alpha'')$. From Eq. B.13, β is an important parameter that determines the oscillation frequency of the ions. The relationship of β to (a,q) is

given by the recursive formula:

$$\beta^2 = a + \cfrac{q^2}{(2+\beta)^2 - a - \cfrac{q^2}{(4+\beta^2) - a - \cfrac{q^2}{(6+\beta)^2 - a - \ldots}}} + \cfrac{q^2}{(\beta-2)^2 - a - \cfrac{q^2}{(\beta^2-4) - a - \cfrac{q^2}{(\beta-6)^2 - a - \ldots}}} \tag{B.14}$$

When $q \leq 0.4$, β can be approximated by

$$\beta^2 \approx a + \frac{q^2}{2} \tag{B.15}$$

Therefore, for a given combination of RF and DC voltages, ions in a quadrupole field have oscilaltory motion that is characterized by frequencies unique to their mass-to-charge ratio. The lowest frequency is named "secular frequency". Higher frequencies are not simple harmonics of the lowest frequency. These frequencies can be calculated using the following relationship [237]:

$$\omega_u = (2n + \beta)\frac{\Omega}{2}, n = 0, \pm 1, \pm 2, \ldots \tag{B.16}$$

As previously discussed, the stability of the ion trajectory depends on the a and q values. Using a stability diagram, stable combination of (a,q) values are readily seen. In the stability diagram there is an infinite number of regions where ion motion is stable in both the x and y directions. The first overlapping region for combined x and y stability with iso-β lines is plotted in Fig. B.2, where most of commercial mass filters are operated.

Considering that a/q is equal to $2U/V$, all ions lie along an operating (or scan) line a/q =constant. Therefore, by scanning the U and V values along this line (i.e. with a fixed ratio), ions with different masses will be transmitted in sequence of mass-to-charge ratio, producing a mass spectrum. Each operating line with specific slope (a/q) corresponds to one resolution setting. By increasing the U/V ratio, the operating line approaches closer to the tip of the stability region and only a small range of m/z values will be transmitted. This corresponds to a higher resolution. The operational mass range and resolution are discussed in the following.

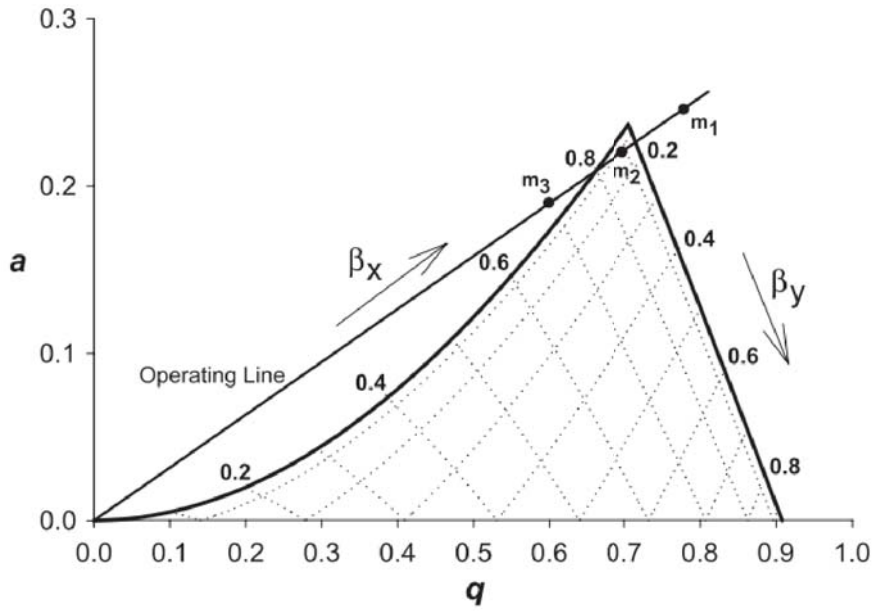

Figure B.2: Stability regions. Reproduced from the publication of D.J. Douglas [237].

B.2 Mass range and resolution in a quadrupole filter

The two important operating characteristics of a quadrupole, the mass range and the maximum resolution are dependent upon five basic parameters. Length and diameter of the rods, the peak-to-peak maximum voltage of the rods, the RF frequency and the injection energy of the ions [236]. The mass range, or rather, the highest mass (M_m) to which an instrument can be tuned is given by the following relation:

$$M_m = \frac{7 \times 10^6 \cdot V_{\mathrm{RF}}}{f^2 \cdot R^2} \tag{B.17}$$

where f is the frequency in Hz ($f = \dfrac{\Omega}{2\pi}$) and R is the radius of the rod. M_m is given in amu.

For the majority of instruments designed and operated to the present date, the available choice of V_{RF} and R is relatively limited. V_{RF} is of the order of 3000 V and R has acceptable values in the range 3-10 mm. V_{RF} is limited by the difficulties inherent in the design of very stable high-voltage RF generators and R by the problem of maintaining a high mechanical accuracy at a reasonable cost with both very large and very small instruments.

The selection of mass range sets a limit to the resolution that can be obtained

throughout the operating range. The finite length of the quadrupole electrodes limits the time spent by the ions in the focusing field and hence limits the resolution that can be obtained. Although a precise relationship cannot be quoted, there is strong evidence from the various experimental studies that a good representation is given by [236]:

$$\frac{M}{\Delta M} = \frac{1}{K} N^n \tag{B.18}$$

where N is the number of cycles of the RF field to which the ions are exposed and ΔM is the width of the "peak" at the mass M. K is usually assumed to be about 20 for all practical purposes and n is considered to be about 2 [238].

In a given instrument, the number of cycles, N, and hence the limiting resolution, can easily be determined in terms of the following basic operating parameters: the length of the quadrupole rods, L, the RF frequency, f, and the ion injection energy, k_z, as such:

$$N = f \cdot L \sqrt{\frac{m}{2 \cdot e \cdot k_z}} \tag{B.19}$$

Therefore the Eq. B.18 can be rewritten as:

$$\frac{m}{\Delta m} = \frac{0.05 f^2 \cdot L^2 \cdot m}{2 \cdot e \cdot k_z} \tag{B.20}$$

hence

$$\Delta m = \frac{40 \cdot e \cdot k_z}{f^2 \cdot L^2} \tag{B.21}$$

Using capital M to indicate the mass in amu gives:

$$\Delta M = \frac{4 \times 10^9 k_z}{f^2 \cdot L^2} \tag{B.22}$$

The range of values of ion injection energy is narrow in practical instruments. The lower limit, of the order of 2 eV, cannot easily be extended because of difficulties of efficient injection of ions into the quadrupole.

Typical values can be assumed: $L = 0.2\,\mathrm{m}$, $f = 2.0\,\mathrm{MHz}$, $k_z = 5\,\mathrm{eV}$, therefore Eq. B.22 yields

$$\Delta M = 0.125\,\mathrm{amu} \tag{B.23}$$

which shows that an adequate resolution is possible, and, neglecting second-order effects such as field imperfections, the minimum attainable peak width, ΔM, is independent of ion mass.

It is important to recognize that mass resolution indicates the maximum possible performance and has been calculated by making no allowance for instrument imperfections. In practice, factors such as misalignment lowers the resolution close to unity for standard quadrupole filters application.

References

[1] M.E. Brown and C.C. Funk. **Climate: Food security under climate change**. *Science*, **319**(5863):580, 2008.

[2] C. Raleigh and H. Urdal. **Climate change, environmental degradation and armed conflict**. *Political Geography*, **26**(6):674 – 694, 2007.

[3] P.A. O'Hara. **Political economy of climate change, ecological destruction and uneven development**. *Ecological Economics*, **69**(2):223 – 234, 2009.

[4] D. Layfield. **International policy on climate change: after Kyoto, what next?** *Environmental Politics*, **19**(4):657–661, 2010.

[5] R. Knutti, T.F. Stocker, F. Joos and G.K. Plattner. **Constraints on radiative forcing and future climate change from observations and climate model ensembles**. *Nature*, **416**(6882):719–723, 2002.

[6] C. Frei, R. Schoell, S. Fukutome, J. Schmidli and P.L. Vidale. **Future change of precipitation extremes in Europe: Intercomparison of scenarios from regional climate models**. *Journal of Geophysical Research*, **111**(D6):D06105, 2006.

[7] D.T. Shindell, G. Faluvegi, D.M. Koch, G.A. Schmidt, N. Unger and S.E. Bauer. **Improved Attribution of Climate Forcing to Emissions**. *Science*, **326**(5953):716–718, 2009.

[8] J. Lelieveld, TM Butler, JN Crowley, TJ Dillon, H. Fischer, L. Ganzeveld, H. Harder, MG Lawrence, M. Martinez, D. Taraborrelli et al. **Atmospheric oxidation capacity sustained by a tropical forest**. *Nature*, **452**(7188):737–740, 2008.

[9] A. Quillet, C. Peng and M. Garneau. **Toward dynamic global vegetation models for simulating vegetation–climate interactions and feedbacks: recent developments, limitations, and future challenges**. *Environmental Reviews*, **18**:333–353, 2010.

[10] JH Seinfeld and SN Pandis. **Atmospheric Chemistry and Physics: From Air Pollution to Climate Change, 1203 pp**. 2006.

[11] J. S. Hosking, M. R. Russo, P. Braesicke and J. A. Pyle. **Modelling deep convection and its impacts on the tropical tropopause layer**. *Atmospheric Chemistry and Physics*, **10**(22):11175–11188, 2010.

[12] A. Gettelman, MI Hegglin, SW Son, J. Kim, M. Fujiwara, T. Birner, S. Kremser, M. Rex, JA Anel, H. Akiyoshi et al. **Multimodel assessment of the upper troposphere and lower stratosphere: Tropics and global trends**. *Journal of Geophysical Research*, **115**, 2010.

[13] R. Holzinger, DB Millet, B. Williams, A. Lee, N. Kreisberg, SV Hering, J. Jimenez, JD Allan, DR Worsnop and AH Goldstein. **Emission, oxidation, and secondary organic aerosol formation of volatile organic compounds as observed at Chebogue Point**. *Journal of Geophysical Research*, **112**:12, 2007.

[14] C. Warneke, SA McKeen, JA De Gouw, PD Goldan, WC Kuster, JS Holloway, EJ Williams, BM Lerner, DD Parrish, M. Trainer et al. **Determination of urban volatile organic compound emission ratios and comparison with an emissions database**. *Journal of Geophysical Research*, **112**, 2007.

[15] R. Atkinson. **Atmospheric chemistry of VOCs and NOx**. *Atmospheric Environment*, **34**(12-14):2063–2101, 2000.

[16] U. Platt and F. Heintz. **Nitrate radicals in tropospheric chemistry**. *Israel Journal of Chemistry*, **34**(3):289–300, 1994.

[17] C. R. Hoyle, M. Boy, N. M. Donahue, J. L. Fry, M. Glasius, A. Guenther, A. G. Hallar, K. Huff Hartz, M. D. Petters, T. Petäjä, T. Rosenoern and A. P. Sullivan. **A review**

of the anthropogenic influence on biogenic secondary organic aerosol. *Atmospheric Chemistry and Physics*, **11**(1):321–343, 2011.

[18] U. Pöschl. **Atmospheric aerosols: Composition, transformation, climate and health effects**. *Angewandte Chemie International Edition*, **44**(46):7520–7540, 2005.

[19] M.O. Andreae. **Aerosols Before Pollution**. *Science*, **315**:50–51, 2007.

[20] AG Carlton, C. Wiedinmyer and JH Kroll. **A review of Secondary Organic Aerosol(SOA) formation from isoprene**. *Atmospheric Chemistry and Physics*, **9**(14):4987–5005, 2009.

[21] J. De Gouw and J.L. Jimenez. **Organic aerosols in the Earths atmosphere**. *Environmental Science & Technology*, **43**(20):7614–7618, 2009.

[22] SA McKeen, T. Gierczak, JB Burkholder, PO Wennberg, TF Hanisco, ER Keim, R.S. Gao, SC Liu, AR Ravishankara and DW Fahey. **The photochemistry of acetone in the upper troposphere: A source of odd-hydrogen radicals**. *Geophysical Research Letters*, **24**(24):3177–3180, 1997.

[23] H. Singh, Y. Chen, A. Tabazadeh, Y. Fukui, I. Bey, R. Yantosca, D. Jacob, F. Arnold, K. Wohlfrom, E. Atlas et al. **Distribution and fate of selected oxygenated organic species in the troposphere and lower stratosphere over the Atlantic**. *Journal of Geophysical Research*, **105**(D3):3795–3805, 2000.

[24] H.B. Singh, M. Kanakidou, PJ Crutzen and DJ Jacob. **High concentrations and photochemical fate of oxygenated hydrocarbons in the global troposphere**. *Nature*, **378**(6552):50–54, 1995.

[25] G.S. Tyndall, J.J. Orlando, T.J. Wallington and M.D. Hurley. **Pressure dependence of the rate coefficients and product yields for the reaction of CH_3CO radicals with O_2**. *International Journal of Chemical Kinetics*, **29**(9):655–663, 1997.

[26] PO Wennberg, TF Hanisco, L. Jaegle, DJ Jacob, EJ Hintsa, EJ Lanzendorf, JG Anderson, R.S. Gao, ER Keim, SG Donnelly et al. **Hydrogen radicals, nitrogen radicals, and the production of O_3 in the upper troposphere**. *Science*, **279**(5347):49, 1998.

[27] MA Blitz, DE Heard, MJ Pilling, SR Arnold and MP Chipperfield. **Pressure and temperature-dependent quantum yields for the photodissociation of acetone between 279 and 327.5 nm**. *Geophys. Res. Lett*, **31**, 2004.

[28] T. J. Dillon, A. Pozzer, J. N. Crowley and J. Lelieveld. **Does acetone react with HO_2 in the upper-troposphere?** *Atmospheric Chemistry and Physics Discussions*, **10**(7):16747–16773, 2010.

[29] J. de Gouw and C. Warneke. **Measeruements of Volatile Organic Compounds In the Earth's Atmosphere Using Proton-Transfer-Reaction Mass Spectrometry**. *Mass Spectrometry Reviews*, **26**:223–257, 2007.

[30] F. Arnold and G. Hauck. **Lower stratosphere trace gas detection using aircraft-borne active chemical ionization mass spectrometry**. *Nature*, **315**:307–309, 1985.

[31] R. Holzinger, C. Warneke, A. Hansel, A. Jordan, W. Lindinger, D.H. Scharffe, G. Schade and P.J. Crutzen. **Biomass burning as a source of formaldehyde, acetaldehyde, methanol, acetone, acetonitrile, and hydrogen cyanide**. *Geophysical Research Letters*, **26**(8):1161–1164, 1999.

[32] O. Möhler, T. Reiner and F. Arnold. **A novel aircraft-based tandem mass spectrometer for atmospheric ion and trace gas measurements**. *Review of Scientific Instruments*, **64**:1199, 1993.

[33] D. Sprung, C. Jost, T. Reiner, A. Hansel and A. Wisthaler. **Acetone and acetonitrile in the tropical Indian Ocean boundary layer and free troposphere- Aircraft-based intercomparison of AP-CIMS and PTR-MS measurements**. *Journal of Geophysical Research. D. Atmospheres(0148-0227)*, **106**:28, 2001.

[34] D. Sprung and A. Zahn. **Acetone in the upper troposphere/lowermost stratosphere measured by the CARIBIC passenger aircraft: Distribution, seasonal cycle, and variability**. *Journal of Geophysical Research*, **115**(D16):D16301, 2010.

[35] C. Warneke, J.A. de Gouw, W.C. Kuster, P.D. Goldan and R. Fall. **Validation of atmospheric VOC measurements by proton-transfer-reaction mass spectrometry using a gas-chromatographic preseparation method**. *Environmental Science & Technology*, **37**(11):2494–501, 2003.

[36] CAM Brenninkmeijer, P. Crutzen, F. Boumard, T. Dauer, B. Dix, R. Ebinghaus, D. Filippi, H. Fischer, H. Franke, U. Frieß et al. **Civil aircraft for the regular investigation of the atmosphere based on an instrumented container: the new CARIBIC system**. *Atmospheric Chemistry and Physics*, **7**:4953–4976, 2007.

[37] A. Zahn, C. A. M. Brenninkmeijer and P. F. J. van Velthoven. **Passenger aircraft project CARIBIC 1997-2002, Part I: the extratropical chemical tropopause**. *Atmospheric Chemistry and Physics Discussions*, **4**(1):1091–1117, 2004.

[38] R.G. Prinn. **The cleansing capacity of the atmosphere**. *Annual Review of Environment and Resources*, **28**(1):29–57, 2003.

[39] R. Volkamer, J.L. Jimenez, F. San Martini, K. Dzepina, Q. Zhang, D. Salcedo, L.T. Molina, D.R. Worsnop and M.J. Molina. **Secondary organic aerosol formation from anthropogenic air pollution: Rapid and higher than expected**. *Geophys. Res. Lett*, **33**:17, 2006.

[40] J.G. Calvert. **The mechanisms of atmospheric oxidation of aromatic hydrocarbons**. 2002.

[41] F.W. Lurmann, H.H. Main, KT Knapp, L. Stockburger, RA Rasmussen and K. Fung. **Analysis of the ambient VOC data collected in the Southern California Air Quality Study**. *Final Report to California Air Resources Board Contract*, 1992.

[42] J.M. Roberts and S.B. Bertman. **The thermal decomposition of peroxyacetic nitric anhydride(PAN) and peroxymethacrylic nitric anhydride(MPAN)**. *International Journal of Chemical Kinetics*, **24**(3):297–307, 1992.

[43] R. Atkinson and J. Arey. **Atmospheric Degradation of Volatile Organic Compounds**. *Chemical Reviews*, **103**(12):4605–4638, 2003.

[44] J.A. Logan. **Tropospheric ozone: Seasonal behavior, trends, and anthropogenic influence.** *Journal of Geophysical Research*, **90**(10):463–10, 1985.

[45] HB Singh, D. O'hara, D. Herlth, W. Sachse, DR Blake, JD Bradshaw, M. Kanakidou and PJ Crutzen. **Acetone in the atmosphere: Distribution, sources, and sinks**. *Journal of Geophysical Research*, **99**(D1):1805–1819, 1994.

[46] D.J. Jacob, B.D. Field, E.M. Jin, I. Bey, Q. Li, J.A. Logan, R.M. Yantosca and H.B. Singh. **Atmospheric budget of acetone**. *Journal of Geophysical Research*, **107**(10.1029), 2002.

[47] HB Singh, LJ Salas, RB Chatfield, E. Czech, A. Fried, J. Walega, MJ Evans, BD Field, DJ Jacob, D. Blake et al. **Analysis of the atmospheric distribution, sources, and sinks of oxygenated volatile organic chemicals based on measurements over the Pacific during TRACE-P**. *Journal of Geophysical Research*, **109**:D15S07, 2004.

[48] S. Taddei, P. Toscano, B. Gioli, A. Matese, F. Miglietta, F.P. Vaccari, A. Zaldei, T. Custer and J. Williams. **Carbon Dioxide and Acetone Air- Sea Fluxes over the Southern Atlantic**. *Environmental science & technology*, **43**(14):5218–5222, 2009.

[49] I. Hermans, T.L. Nguyen, P.A. Jacobs and J. Peeters. **Tropopause Chemistry Revisited: HO2-Initiated Oxidation as an Efficient Acetone Sink**. *Journal of the American Chemical Society*, **126**(32):9908–9909, 2004.

[50] JJ Remedios, G. Allen, AM Waterfall, H. Oelhaf, A. Kleinert and DP Moore. **Detection**

of organic compound signatures in infrared, limb emission spectra observed by the MIPAS-B2 balloon instrument. *Atmospheric Chemistry and Physics*, **7**(6):1599–1613, 2007.

[51] PF Coheur, H. Herbin, C. Clerbaux, D. Hurtmans, C. Wespes, M. Carleer, S. Turquety, CP Rinsland, J. Remedios, D. Hauglustaine et al. **ACE-FTS observation of a young biomass burning plume: first reported measurements of C2H4, C3H6O, H2CO and PAN by infrared occultation from space**. *Atmospheric Chemistry and Physics*, **7**:5437–5446, 2007.

[52] F. Arnold, V. Bürger, B. Droste-Fanke, F. Grimm, A. Krieger, J. Schneider and T. Stilp. **Acetone in the upper troposphere and lower stratosphere: Impact on trace gases and aerosols**. *Geophysical Research Letters*, **24**(23):3017–3020, 1997.

[53] R.B. Chatfield, E.P. Gardner and J.G. Calvert. **Sources and sinks of acetone in the troposphere: Behavior of reactive hydrocarbons and a stable product**. *Journal of Geophysical Research*, **92**(D4):4208–4216, 1987.

[54] A. Colomb, J. Williams, J. Crowley, V. Gros, R. Hofmann, G. Salisbury, T. Klüpfel, R. Kormann, A. Stickler, C. Forster et al. **Airborne measurements of trace organic species in the upper troposphere over Europe: the impact of deep convection**. *Environmental Chemistry*, **3**(4):244–259, 2006.

[55] J.A. de Gouw, C. Warneke, R. Holzinger, T. Klupfel and J. Williams. **Intercomparison between airborne measurements of methanol, acetonitrile and acetone using two differently configured PTR-MS instruments**. *International Journal of Mass Spectrometry*, **239**:129–137, 2004.

[56] H. Fischer, M. De Reus, M. Traub, J. Williams, J. Lelieveld, J. De Gouw, C. Warneke, H. Schlager, A. Minikin, R. Scheele et al. **Deep convective injection of boundary layer air into the lowermost stratosphere at midlatitudes**. *Atmospheric Chemistry and Physics*, **3**(3):739–745, 2003.

[57] A. Kiendler and F. Arnold. **Detection of gaseous oxygenated hydrocarbons in upper tropospheric and lower stratospheric aircraft borne experiments**. *International Journal of Mass Spectrometry*, **223**:733–741, 2003.

[58] H. A. Scheeren, J. Lelieveld, G. J. Roelofs, J. Williams, H. Fischer, M. de Reus, J. A. de Gouw, C. Warneke, R. Holzinger, H. Schlager, T. Klpfel, M. Bolder, C. van der Veen and M. Lawrence. **The impact of monsoon outflow from India and Southeast Asia in the upper troposphere over the eastern Mediterranean**. *Atmospheric Chemistry and Physics*, **3**(5):1589–1608, 2003.

[59] HB Singh, Y. Chen, GL Gregory, GW Sachse, R. Talbot, DR Blake, Y. Kondo, JD Bradshaw, B. Heikes and D. Thornton. **Trace chemical measurements from the northern midlatitude lowermost stratosphere in early spring: Distributions, correlations, and fate**. *Geophysical Research Letters*, **24**(2):127–130, 1997.

[60] K.H. Wohlfrom, T. Hauler, F. Arnold and H. Singh. **Acetone in the free troposphere and lower stratosphere: Aircraft-based CIMS and GC measurements over the North Atlantic and a first comparison**. *Geophysical Research Letters*, **26**(18):2849–2852, 1999.

[61] TG Karl, TJ Christian, RJ Yokelson, P. Artaxo, W.M. Hao and A. Guenther. **The Tropical Forest and Fire Emissions Experiment: method evaluation of volatile organic compound emissions measured by PTR-MS, FTIR, and GC from tropical biomass burning**. *Atmospheric Chemistry and Physics*, **7**(22):5883–5897, 2007.

[62] A. Wisthaler, P. Strøm-Tejsen, L. Fang, T.J. Arnaud, A. Hansel, T.D. MAerk and D.P. Wyon. **PTR-MS assessment of photocatalytic and sorption-based purification of recirculated cabin air during simulated 7-h flights with high passenger density**. *Environmental Science & Technology*, **41**(1):229–234, 2007.

[63] LM Russell, AA Mensah, EV Fischer, BC Sive, RK Varner, WC Keene, J. Stutz and AAP Pszenny. **Nanoparticle growth following photochemical α-and β-pinene oxidation at Appledore Island during International Consortium for Research on Transport and Transformation/Chemistry of Halogens at the Isles of Shoals 2004**. *Journal of Geophysical Research*, **112**(D10):D10S21, 2007.

[64] U. Janovsky, S. Scholl-Bürgi, D. Karall, J. Beauchamp, A. Hansel, G. Poupart, A. Schmid and A. Amann. **Breath gas analysis in patients suffering from propionic acidaemia**. *Breath Analysis for Clinical Diagnosis and Therapeutic Monitoring*, 401–7, 2005.

[65] W. Lindinger, J. Taucher, A. Jordan, A. Hansel and W. Vogel. **Endogenous production of methanol after the consumption of fruit**. *Alcoholism: Clinical and Experimental Research*, **21**(5):939–943, 1997.

[66] M.L. Mateus, C. Lindinger, J.C. Gumy and R. Liardon. **Release Kinetics of Volatile Organic Compounds from Roasted and Ground Coffee: Online Measurements by PTR-MS and Mathematical Modeling**. *Journal of Agricultural and Food Chemistry*, **55**(25):10117–10128, 2007.

[67] N. Araghipour, J. Colineau, A. Koot, W. Akkermans, J.M.M. Rojas, J. Beauchamp, A. Wisthaler, T.D. Märk, G. Downey, C. Guillou et al. **Geographical origin classification of olive oils by PTR-MS**. *Food Chemistry*, **108**(1):374–383, 2008.

[68] D. Mayr, R. Margesin, F. Schinner and T. D. Mrk. **Detection of the spoiling of meat using PTR-MS**. *International Journal of Mass Spectrometry*, **223-224**:229 – 235, 2003.

[69] W. Grabmer, J. Kreuzwieser, A. Wisthaler, C. Cojocariu, M. Graus, H. Rennenberg, D. Steigner, R. Steinbrecher and A. Hansel. **VOC emissions from Norway spruce (Picea abies L. [Karst]) twigs in the field–Results of a dynamic enclosure study**. *Atmospheric Environment*, **40**(Supplement 1):128 – 137, 2006.

[70] S.D. Maleknia, T. L. Bell and M.A. Adams. **PTR-MS analysis of reference and plant-emitted volatile organic compounds**. *International Journal of Mass Spectrometry*, **262**(3):203 – 210, 2007.

[71] A. Hansel, A. Jordan, R. Holzinger, P. Prazeller, W. Vogel and W. Lindinger. **Proton transfer reaction mass spectrometry: on-line trace gas analysis at the ppb level**. *International Journal of Mass Spectrometry and Ion Processes*, **149**:609–619, 1995.

[72] W. Lindinger, A. Hansel and A. Jordan. **On-line monitoring of volatile organic compounds at pptv levels by means of proton-transfer-reaction mass spectrometry (PTR-MS) medical applications, food control and environmental research**. *International Journal of Mass Spectrometry and Ion Processes*, **173**(3):191–241, 1998.

[73] F.W. McLafferty. **Mass spectrometric analysis broad applicability to chemical research**. *Analytical Chemistry*, **28**(3):306–316, 1956.

[74] K. Biemann and J. Seibl. **Application of mass spectrometry to structure problems. II. Stereochemistry of epimeric, cyclic alcohols**. *Journal of the American Chemical Society*, **81**(12):3149–3150, 1959.

[75] C. Djerassi, JM Wilson, H. Budzikiewicz and JW Chamberlin. **Mass Spectrometry in Structural and Stereochemical Problems. XIV. 1 Steroids with One or Two Aromatic Rings 2**. *Journal of the American Chemical Society*, **84**(23):4544–4552, 1962.

[76] A.T. James and A.J.P. Martin. **Gas-liquid partition chromatography: the separation and micro-estimation of volatile fatty acids from formic acid to dodecanoic acid**. *Biochemical Journal*, **50**(5):679, 1952.

[77] M.S.B. Munson and F.H. Field. **Chemical Ionization Mass Spectrometry. I. General Introduction**. *Journal of the American Chemical Society*, **88**(12):2621–2630, 1966.

REFERENCES

[78] F.C. Fehsenfeld, E.E. Ferguson and A.L. Schmeltekopf. **Thermal-Energy Ion-Neutral Reaction Rates. III. The Measured Rate Constant for the Reaction $O^+(^4S)+CO_2(^1\Sigma) \rightarrow O_2^+(^2\Pi)+CO(^1\Sigma)$**. *Journal of Chemical Physics*, **44**(3022):4087, 1966.

[79] E.E. Ferguson, F.C. Fehsenfeld and A.L. Schmeltekopf. **Flowing Afterglow Measurements of Ion-Neutral Reactions**. **5**:1 – 56, 1969.

[80] N.G. Adams and D. Smith. **The selected ion flow tube (SIFT); A technique for studying ion-neutral reactions**. *International Journal of Mass Spectrometry and Ion Physics*, **21**(3-4):349 – 359, 1976.

[81] D. David Smith and P. Spanel. **Selected ion flow tube mass spectrometry (SIFT-MS) for on-line trace gas analysis**. *Mass Spectrometry Reviews*, **24**(5):661–700, 2005.

[82] P. Spanel, M. Pavlik and D. Smith. **Reactions of H_3O^+ and OH^- ions with some organic molecules; applications to trace gas analysis in air**. *International Journal of Mass Spectrometry and Ion Processes*, **145**(3):177–186, 1995.

[83] A. Lagg, J. Taucher, A. Hansel and W. Lindinger. **Applications of proton transfer reactions to gas analysis**. *International Journal of Mass Spectrometry and Ion Processes*, **134**(1):55–66, 1994.

[84] A. Jordan, S. Haidacher, G. Hanel, E. Hartungen, J. Herbig, L. Märk, R. Schottkowsky, H. Seehauser, P. Sulzer and TD Märk. **An online ultra-high sensitivity Proton-transfer-reaction mass-spectrometer combined with switchable reagent ion capability (PTR+ SRI- MS)**. *International Journal of Mass Spectrometry*, 2009.

[85] F. Howorka, W. Lindinger and M. Pahl. **Ion sampling from the negative glow plasma in a cylindrical hollow cathode**. *International Journal or Mass Spectrometry and Ion Physics*, **12**(1):67 – 77, 1973.

[86] W. Lindinger, E. Alge, H. Stri, R. N. Varney, H. Helm, P. Holzmann and M. Pahl. **Investigation of ion-molecule reactions using a drift tube with separated ion source**. *International Journal or Mass Spectrometry and Ion Physics*, **30**(3-4):251 – 261, 1979.

[87] A. Bogaerts and R. Gijbels. **Fundamental aspects and applications of glow discharge spectrometric techniques**. *Spectrochimica Acta Part B: Atomic Spectroscopy*, **53**(1):1–42, 1998.

[88] S.T. Arnold, AA Viggiano and R.A. Morris. **Rate Constants and Product Branching Fractions for the Reactions of $H3O^+$ and NO^+ with C2-C12 Alkanes**. *The Journal of Physical Chemistry A*, **102**(45):8881–8887, 1998.

[89] B.E. Henry E. Kosciuch D.R. Hanson, J. Greenberg. **Proton transfer reaction mass spectrometry at high drift tube pressure**. *International Journal of Mass Spectrometry*, **223-224**:507–518, 2003.

[90] R.S. Blake, P.S. Monks and A.M. Ellis. **Proton-Transfer Reaction Mass Spectrometry**. *Chemical Reviews*, **109**(2):711–724, 2009.

[91] DR Hanson, M. Koppes, A. Stoffers, R. Harsdorf and K. Edelen. **Proton transfer mass spectrometry at 11hPa with a circular glow discharge: Sensitivities and applications**. *International Journal of Mass Spectrometry*, **282**(1-2):28–37, 2009.

[92] S. Inomata, H. Tanimoto, N. Aoki, J. Hirokawa and Y. Sadanaga. **A novel discharge source of hydronium ions for proton transfer reaction ionization: design, characterization, and performance**. *Rapid Communications in Mass Spectrometry*, **20**:1025–1029, 2006.

[93] T. Mikoviny, L. Kaser and A. Wisthaler. **Development and characterization of a High-Temperature Proton-Transfer-Reaction Mass Spectrometer (HT-PTR-MS)**. *Atmospheric Measurement Techniques*, **3**(3):537–544, 2010.

[94] C. Warneke, C. van der Veen, S. Luxembourg, J. de Gouw and A. Kok. **Measurements of benzene and toluene in ambient air using proton-transfer-reaction mass spectrometry: calibration, humidity dependence, and field intercomparison**. *International Journal of Mass Spectrometry*, **207**(3):167 – 182, 2001.

[95] I. Dotan, W. Lindinger and DL Albritton. **Mobilities of H_2O^+ and $H_3O^+.nH_2O$(n= 0, 1, 2) ions in He**. *The Journal of Chemical Physics*, **67**(12):5968–5969, 1977.

[96] J. de Gouw, C. Warneke, T. Karl, G. Eerdekens, C. van der Veen and R. Fall. **Sensitivity and specificity of atmospheric trace gas detection by proton-transfer-reaction mass spectrometry**. *International Journal of Mass Spectrometry*, **223-224**:365–382, 2003.

[97] AA Viggiano and R.A. Morris. **Rotational and Vibrational Energy Effects on Ion-Molecule Reactivity As Studied by the VT-SIFDT Technique**. *J. Phys. Chem*, **100**(50):19227–19240, 1996.

[98] L. Keck, U. Oeh and C. Hoeschen. **Corrected equation for the concentrations in the drift tube of a proton transfer reaction-mass spectrometer (PTR-MS)**. *International Journal of Mass Spectrometry*, **264**(1):92 – 95, 2007.

[99] J.A. De Gouw, C.J. Howard, T.G. Custer, B.M. Baker and R. Fall. **Proton-transfer chemical-ionization mass spectrometry allows real-time analysis of volatile organic compounds released from cutting and drying of crops**. *Environmental Science & Technology*, **34**(12):2640–2648, 2000.

[100] J.A. de Gouw, C.J. Howard, T.G. Custer and R. Fall. **Emissions of volatile organic compounds from cut grass and clover are enhanced during the drying process**. *Geophysical Research Letters*, **26**(7):811–814, 1999.

[101] T. Thornberry, D.M. Murphy, D.S. Thomson, J. de Gouw, C. Warneke, T.S. Bates, P.K. Quinn and D. Coffman. **Measurement of Aerosol Organic Compounds Using a Novel Collection/Thermal-Desorption PTR-ITMS Instrument**. *Aerosol Science and Technology*, **43**(5):486–501, 2009.

[102] B. T. Jobson and J. K. McCoskey. **Sample drying to improve HCHO measurements by PTR-MS instruments: laboratory and field measurements**. *Atmospheric Chemistry and Physics*, **10**(4):1821–1835, 2010.

[103] W. Paul, HP Reinhard and U. von. **Das elektrische Massenfilter als Massenspektrometer und Isotopentrenner**. *Zeitschrift für Physik A Hadrons and Nuclei*, **152**(2):143–182, 1958.

[104] P. Prazeller, P.T. Palmer, E. Boscaini, T. Jobson and M. Alexander. **Proton transfer reaction ion trap mass spectrometer**. *Rapid Communications in Mass Spectrometry*, **17**(14):1593–1599, 2003.

[105] C. Warneke, JA De Gouw, ER Lovejoy, PC Murphy, WC Kuster and R. Fall. **Development of proton-transfer ion trap-mass spectrometry: On-line detection and identification of volatile organic compounds in air**. *Journal of the American Society for Mass Spectrometry*, **16**(8):1316–1324, 2005.

[106] L.H. Mielke, D.E. Erickson, S.A. McLuckey, M. Müller, A. Wisthaler, A. Hansel and P.B. Shepson. **Development of a Proton-Transfer Reaction-Linear Ion Trap Mass Spectrometer for Quantitative Determination of Volatile Organic Compounds.** *Analytical chemistry*, 2008.

[107] R.S. Blake, C. Whyte, C.O. Hughes, A.M. Ellis and P.S. Monks. **Demonstration of Proton-Transfer Reaction Time-of-Flight Mass Spectrometry for real-time analysis of trace volatile organic compounds**. *Analytical Chemistry*, **76**(13):3841–3845, 2004.

[108] CJ Ennis, JC Reynolds, BJ Keely and LJ Carpenter. **A hollow cathode proton transfer reaction time of flight mass spectrometer**. *International Journal of Mass Spectrometry*, **247**(1-3):72–80, 2005.

[109] H. Tanimoto, N. Aoki, S. Inomata, J. Hirokawa and Y. Sadanaga. **Development of a PTR-TOF-MS instrument for real-time measurements of volatile organic compounds in air**. *International Journal of Mass Spectrometry*, **263**(1):1–11, 2007.

[110] A. Jordan, S. Haidacher, G. Hanel, E. Hartungen, L. Mrk, H. Seehauser, R. Schottkowsky, P. Sulzer and T.D. Mrk. **A high resolution and high sensitivity proton-transfer-reaction time-of-flight mass spectrometer (PTR-TOF-MS)**. *International Journal of Mass Spectrometry*, **286**(2-3):122 – 128, 2009.

[111] T. Karl, R. Fall, PJ Crutzen, A. Jordan and W. Lindinger. **High concentrations of reactive biogenic VOCs at a high altitude site in late autumn**. *Geophysical Research Letters*, **28**(3):507–510, 2001.

[112] W. Lindinger and A. Jordan. **Proton-transfer-reaction mass spectrometry (PTR–MS): on-line monitoring of volatile organic compounds at pptv levels**. *Chemical Society Reviews*, **27**(5):347–375, 1998.

[113] W.B. Knighton, E.C. Fortner, S.C. Herndon, E.C. Wood and R.C. Miake-Lye. **Adaptation of a proton transfer reaction mass spectrometer instrument to employ NO^+ as reagent ion for the detection of 1,3-butadiene in the ambient atmosphere**. *Rapid Communications in Mass Spectrometry*, **23**(20):3301–3308, 2009.

[114] M. Norman, A. Hansel and A. Wisthaler. **$O_2{}^+$ as reagent ion in the PTR-MS instrument: Detection of gas-phase ammonia**. *International Journal of Mass Spectrometry*, **265**(2-3):382–387, 2007.

[115] JA de Gouw, PD Goldan, C. Warneke, WC Kuster, JM Roberts, M. Marchewka, SB Bertman, AAP Pszenny and WC Keene. **Validation of proton transfer reaction-mass spectrometry (PTR-MS) measurements of gas-phase organic compounds in the atmosphere during the New England Air Quality Study (NEAQS) in 2002**. *Journal of Geophysical Research*, **108**(D21), 2003.

[116] I.E. Galbally, S.J. Lawson, I.A. Weeks, S.T. Bentley, R.W. Gillett, M. Meyer and A.H. Goldstein. **Volatile organic compounds in marine air at Cape Grim, Australia**. *Environmental Chemistry*, **4**(3):178–182, 2007.

[117] S. Inomata, H. Tanimoto, S. Kato, J. Suthawaree, Y. Kanaya, P. Pochanart, Y. Liu and Z. Wang. **PTR-MS measurements of non-methane volatile organic compounds during an intensive field campaign at the summit of Mount Tai, China, in June 2006**. *Atmospheric Chemistry and Physics*, **10**(15):7085–7099, 2010.

[118] TM Ruuskanen, R. Taipale, J. Rinne, MK Kajos, H. Hakola and M. Kulmala. **Quantitative long-term measurements of VOC concentrations by PTR-MS: annual cycle at a boreal forest site**. *Atmos. Chem. Phys. Discuss*, **9**:81–134, 2009.

[119] G. Salisbury, J. Williams, R. Holzinger, V. Gros, N. Mihalopoulos, M. Vrekoussis, R. Sarda-Esteve, H. Berresheim, R. Von Kuhlmann, M. Lawrence et al. **Ground-based PTR-MS measurements of reactive organic compounds during the MINOS campaign in Crete, July–August 2001**. *Atmospheric Chemistry and Physics*, **3**(4):940, 2003.

[120] R. Taipale, T. M. Ruuskanen, J. Rinne, M. K. Kajos, H. Hakola, T. Pohja and M. Kulmala. **Technical Note: Quantitative long-term measurements of VOC concentrations by PTR-MS; measurement, calibration, and volume mixing ratio calculation methods**. *Atmospheric Chemistry and Physics*, **8**(22):6681–6698, 2008.

[121] TM Rogers, EP Grimsrud, SC Herndon, JT Jayne, C.E. Kolb, E. Allwine, H. Westberg, BK Lamb, M. Zavala, LT Molina et al. **On-road measurements of volatile organic compounds in the Mexico City metropolitan area using proton transfer reaction mass spectrometry**. *International Journal of Mass Spectrometry*, **252**(1):26–37, 2006.

[122] II Timkovsky, NF Elanskii, AI Skorokhod and RA Shumskii. **Studying of biogenic volatile organic compounds in the atmosphere over Russia**. *Izvestiya Atmospheric and Oceanic Physics*, **46**(3):319–327, 2010.

[123] A. Colomb, V. Gros, S. Alvain, R. Sarda-Esteve, B. Bonsang, C. Moulin, T. Kluepfel and J. Williams. **Variation of atmospheric volatile organic compounds over the Southern Indian Ocean (30–49^o S)**. *Environmental Chemistry*, **6**(1):70–82, 2009.

[124] H. Riede R. Sander P. Jöckel P. Hoor A. Pozzer S. Wong-Zehnpfennig Z. Hosaynali Beygi H. Fischer V. Gros A. Colomb B. Bonsang N. Yassaa I. Peeken E. L. Atlas C. M. Waluda J. A. van Aardenne J. Lelieveld J. Williams, T. Custer. **Assessing the effect of marine isoprene and ship emissions on ozone, using modelling and measurements from the South Atlantic Ocean**. *Environmental Chemistry*, **7**:171, 2010.

[125] R. Schnitzhofer, A. Wisthaler and A. Hansel. **Real-time profiling of organic trace gases in the planetary boundary layer by PTR-MS using a tethered balloon**. *Atmospheric Measurement Techniques*, **2**:773–777, 2009.

[126] G. Eerdekens, L. Ganzeveld, T. Kluepfel, V. Sinha, N. Yassaa, J. Williams, H. Harder, D. Kubistin, M. Martinez and J. Lelieveld. **Flux estimates of isoprene, methanol and acetone from airborne PTR-MS measurements over the tropical rainforest during the GABRIEL 2005 campaign**. *Atmospheric Chemistry and Physics*, **9**:4207–4227, 2009.

[127] J. G. Murphy, D. E. Oram and C. E. Reeves. **Measurements of volatile organic compounds over West Africa**. *Atmospheric Chemistry and Physics*, **10**(12):5281–5294, 2010.

[128] PJ Crutzen, J. Williams, U. Pöschl, P. Hoor, H. Fischer, C. Warneke, R. Holzinger, A. Hansel, W. Lindinger, B. Scheeren et al. **High spatial and temporal resolution measurements of primary organics and their oxidation products over the tropical forests of Surinam**. *Atmospheric Environment*, **34**(8):1161–1165, 2000.

[129] JA de Gouw, C. Warneke, HA Scheeren, C. van der Veen, M. Bolder, MP Scheele, J. Williams, S. Wong, L. Lange, H. Fischer et al. **Overview of the trace gas measurements on board the Citation aircraft during the intensive field phase of INDOEX**. *Journal of Geophysical Research*, **106**(D22):28453–28468, 2001.

[130] M. De Reus, H. Fischer, F. Arnold, J. De Gouw, R. Holzinger, C. Warneke and J. Williams. **On the relationship between acetone and carbon monoxide in different air masses**. *Atmospheric Chemistry and Physics*, **3**(5):1709–1723, 2003.

[131] J. Lelieveld, H. Berresheim, S. Borrmann, PJ Crutzen, FJ Dentener, H. Fischer, J. Feichter, PJ Flatau, J. Heland, R. Holzinger et al. **Global air pollution crossroads over the Mediterranean**. *Science*, **298**(5594):794, 2002.

[132] J. De Gouw, C. Warneke, D.D. Parrish, J.S. Holloway, M. Trainer and F.C. Fehsenfeld. **Emission sources and ocean uptake of acetonitrile (CH_3CN) in the atmosphere**. *Journal of Geophysical Research*, **108**(D11):4329, 2003.

[133] T. Karl, T. Jobson, W.C. Kuster, E. Williams, J. Stutz, R. Shetter, S.R. Hall, P. Goldan, F. Fehsenfeld and W. Lindinger. **Use of proton-transfer-reaction mass spectrometry to characterize volatile organic compound sources at the La Porte super site during the Texas Air Quality Study 2000**. *Journal of geophysical research*, **108**(D16):4508, 2003.

[134] M. Steinbacher, J. Dommen, C. Ammann, C. Spirig, A. Neftel and ASH Prevot. **Performance characteristics of a proton-transfer-reaction mass spectrometer (PTR-MS) derived from laboratory and field measurements**. *International Journal of Mass Spectrometry*, **239**(2-3):117–128, 2004.

[135] S. Inomata, H. Tanimoto, S. Kameyama, U. Tsunogai, H. Irie, Y. Kanaya and Z. Wang. **Technical Note: Determination of formaldehyde mixing ratios in air with PTR-MS: laboratory experiments and field measurements**. *Atmospheric Chemistry and Physics*, **8**(2):273–284, 2008.

[136] A. Vlasenko, A. M. Macdonald, S. J. Sjostedt and J. P. D. Abbatt. **Formaldehyde measurements by Proton Transfer Reaction Mass Spectrometry (PTR-MS): correction for humidity effects**. *Atmospheric Measurement Technics Discussion*, **3**:965–988, 2010.

[137] R. Holzinger, A. Jordan, A. Hansel and W. Lindinger. **Automobile Emissions of Acetonitrile: Assessment of its Contribution to the Global Source**. *Journal of Atmospheric Chemistry*, **38**(2):187–193, 2001.

[138] M. M. Kleb, G. Chen, J. H. Crawford, F. M. Flocke and C. C. Brown. **An overview of measurement comparisons from the INTEX-B/MILAGRO airborne field campaign**. *Atmospheric Measurement Techniques*, **4**(1):9–27, 2011.

[139] D. M. Bon, I. M. Ulbrich, J. A. de Gouw, C. Warneke, W. C. Kuster, M. L. Alexander, A. Baker, A. J. Beyersdorf, D. Blake, R. Fall, J. L. Jimenez, S. C. Herndon, L. G. Huey, W. B. Knighton, J. Ortega, S. Springston and O. Vargas. **Measurements of volatile organic compounds at a suburban ground site (T1) in Mexico City during the MILAGRO 2006 campaign: measurement comparison, emission ratios, and source attribution**. *Atmospheric Chemistry and Physics*, **11**(6):2399–2421, 2011.

[140] J. Williams, U. Pöschl, PJ Crutzen, A. Hansel, R. Holzinger, C. Warneke, W. Lindinger and J. Lelieveld. **An Atmospheric Chemistry Interpretation of Mass Scans Obtained from a Proton Transfer Mass Spectrometer Flown over the Tropical Rainforest of Surinam**. *Journal of Atmospheric Chemistry*, **38**(2):133–166, 2001.

[141] MML Steeghs, C. Sikkens, E. Crespo, SM Cristescu and FJM Harren. **Development of a proton-transfer reaction ion trap mass spectrometer: Online detection and analysis of volatile organic compounds**. *International Journal of Mass Spectrometry*, **262**(1-2):16–24, 2007.

[142] A. Hansel and A. Wisthaler. **A method for real-time detection of PAN, PPN and MPAN in ambient air**. *Geophysical research letters*, **27**(6):895–898, 2000.

[143] T. Karl, P.J. Crutzen, M. Mandl, M. Staudinger, A. Guenther, A. Jordan, R. Fall and W. Lindinger. **Variability-lifetime relationship of VOCs observed at the Sonnblick Observatory 1999–estimation of HO-densities**. *Atmospheric Environment*, **35**(31):5287 – 5300, 2001.

[144] R. Holzinger, A. Lee, K.T. Paw and U.A.H. Goldstein. **Observations of oxidation products above a forest imply biogenic emissions of very reactive compounds**. *Atmospheric Chemistry and Physics*, **5**(1):67–75, 2005.

[145] Jacek Namiesnik. **Generation of standard gaseous mixtures**. *Journal of Chromatography A*, **300**:79 – 108, 1984.

[146] George C. Rhoderick and Walter R. Miller. **Development of hydrocarbon gas standards**. *Journal of Chromatography A*, **653**(1):71 – 81, 1993.

[147] E.C. Apel, J.G. Calvert and F.C. Fehsenfeld. **The nonmethane hydrocarbon intercomparison experiment (NOMHICE): Tasks 1 and 2**. *Journal of Geophysical Research*, **99**(D8):16651, 1994.

[148] E. Apel, J. Calvert, J. Greenberg, D. Riemer, R. Zika, T. Kleindienst, W. Lonneman, K. Fung and E. Fujita. **Generation and validation of oxygenated volatile organic carbon standards for the 1995 Southern Oxidants Study Nashville Intensive**. *Journal of Geophysical Research*, **103**:22281–22294, 1998.

[149] RS Barratt. **The preparation of standard gas mixtures. A review**. *The analyst*, **106**(1265):817–849, 1981.

[150] Henderson W. M. Huxman T. E. Abrell L. Jardine, K. J. and T. Shartsis. **Dynamic Solution Injection: a new method for preparing pptv-ppbv standard atmospheres of volatile organic compounds**. *Atmospheric Measurement Techniques*, **3**:3047–3066, 2010.

[151] DL Williams. **Calibration in Air Monitoring**. *ASTM STP*, **598**:183–197, 1976.

[152] M. Gautrois and R. Koppmann. **Diffusion technique for the production of gas standards for atmospheric measurements**. *Journal of Chromatography A*, **848**(1-2):239–249, 1999.

[153] RA Washenfelder, CM Roehl, KA McKinney, RR Julian and PO Wennberg. **A compact, lightweight gas standards generator for permeation tubes**. *Review of Scientific Instruments*, **74**:3151, 2003.

[154] C. Jost. **Calibration with permeation devices: is there a pressure dependence of the permeation rates?** *Atmospheric Environment*, **38**(21):3535–3538, 2004.

[155] J.M. Thompson and D.B. Perry. **A new system of refillable and uniquely identifiable diffusion tubes for dynamically generating VOC and SVOC standard atmospheres at ppm and ppb concentrations for calibration of field and laboratory measurements**. *Journal of Environmental Monitoring*, **11**(8):1543–1544, 2009.

[156] P. Veres, J. B. Gilman, J. M. Roberts, W. C. Kuster, C. Warneke, Burling I. R. and J. de Gouw. **Development and validation of a portable gas phase standard generation and calibration system for volatile organic compounds**. *Atmospheric Measurement Techniques*, **3**:333–357, 2010.

[157] A. Naganowska-Nowak, P. Konieczka, A. Przyjazny and J. Namiesnik. **Development of techniques of generation of gaseous standard mixtures**. *Critical Reviews in Analytical Chemistry*, **35**(1):31–55, 2005.

[158] G. Legreid, J.B. Lööv, J. Staehelin, C. Hueglin, M. Hill, B. Buchmann, A. Prevot and S. Reimann. **Oxygenated volatile organic compounds (OVOCs) at an urban background site in Zrich (Europe): Seasonal variation and source allocation**. *Atmospheric Environment*, **41**(38):8409 – 8423, 2007.

[159] E. Starokozhev, E. Fries, A. Cycura and W. Puttmann. **Distribution of VOCs between air and snow at the Jungfraujoch high alpine research station, Switzerland, during CLACE 5 (winter 2006)**. *Atmospheric Chemistry and Physics*, **9**:3197–3207, 2009.

[160] S.D. Maleknia, T.L. Bell and M.A. Adams. **Eucalypt smoke and wildfires: temperature dependent emissions of biogenic volatile organic compounds**. *International Journal of Mass Spectrometry*, **279**(2-3):126–133, 2009.

[161] B. Rappengluck, E. Apel, M. Bauerfeind, J. Bottenheim, P. Brickell, P. Cavolka, J. Cech, L. Gatti, H. Hakola, J. Honzak, R. Junek, D. Martin, C. Noone, Ch. Plass-Dlmer, D. Travers and D. Wang. **The first VOC intercomparison exercise within the Global Atmosphere Watch (GAW)**. *Atmospheric Environment*, **40**(39):7508 – 7527, 2006.

[162] KP Wyche, RS Blake, AM Ellis, P.S. Monks, T. Brauers, R. Koppmann and EC Apel. **Technical Note: Performance of Chemical Ionization Reaction Time-of-Flight Mass Spectrometry (CIR-TOF-MS) for the measurement of atmospherically significant oxygenated volatile organic compounds**. *Atmospheric Chemistry and Physics*, **7**:609–620, 2007.

[163] A.E. O'Keeffe and GC Ortman. **Primary Standards for Trace Gas Analysis.** *Analytical Chemistry*, **38**(6):760–763, 1966.

[164] VICI Metronics. **Generating Calibration Gas Standards**. Technical report, 2004.

[165] G.D. Mitchell. **A review of permeation tubes and permeators**. *Separation & Purification Reviews*, **29**(1):119–128, 2000.

[166] S. Tumbiolo, L. Vincent, J.F. Gal and P.C. Maria. **Thermogravimetric calibration of**

permeation tubes used for the preparation of gas standards for air pollution analysis. *The Analyst*, **130**(10):1369–1374, 2005.

[167] P. Pandey and RS Chauhan. **Membranes for gas separation**. *Progress in Polymer Science*, **26**(6):853–893, 2001.

[168] MH Klopffer and B. Flaconneche. **Transport properties of gases in polymers: bibliographic review**. *Oil & Gas Science and Technology*, **56**(3):223–244, 2001.

[169] V. Stannett. **The transport of gases in synthetic polymeric membranes–an historic perspective**. *Journal of Membrane Science*, **3**(2):97–115, 1978.

[170] SA Stern and S. Trohalaki. **Fundamentals of gas diffusion in rubbery and glassy polymers**. *Barrier polymers and structures*, 22–59, 1990.

[171] Z. Xiuli, Z. Weidong, H. Xinmin, Z. Huifeng, Z. Zeting and Z. Jianchun. **Mathematical Model of Gas Permeation Through PTFE Porous Membrane and the Effect of Membrane Pore Structure**. *Chinese Journal of Chemical Engineering*, **11**(4), 2003.

[172] N. Yi-Yan, RM Felder and WJ Koros. **Selective permeation of hydrocarbon gases in poly (tetrafluoroethylene) and poly (fluoroethylene-propylene) copolymer**. *Journal of Applied Polymer Science*, **25**(8):1755–1774, 1980.

[173] H. Mohamed and S.S. Abdel-Hady, E.E.and Mohamed. **Temperature dependence of the free volume in polytetrafluoroethylene studied by positron annihilation spectroscopy**. *Radiation Physics and Chemistry*, **76**(2):160 – 164, 2007. Proceedings of the 8th International Workshop on Positron and Positronium Chemistry.

[174] AS Michaels and RB Parker Jr. **Sorption and flow of gases in polyethylene**. *Journal of Polymer Science*, **41**(138):53–71, 1959.

[175] A.S. Michaels and H.J. Bixler. **Flow of gases through polyethylene**. *Journal of Polymer Science*, **50**(154):413–439, 1961.

[176] A.S. Michaels and H.J. Bixler. **Solubility of gases in polyethylene**. *Journal of Polymer Science*, **50**(154):393–412, 1961.

[177] SW Rutherford and DD Do. **Review of time lag permeation technique as a method for characterisation of porous media and membranes**. *Adsorption*, **3**(4):283–312, 1997.

[178] J.G. Choi, DD Do and HD Do. **Surface diffusion of adsorbed molecules in porous media: Monolayer, multilayer, and capillary condensation regimes**. *Industrial & Engineering Chemistry Research*, **40**(19):4005–4031, 2001.

[179] H. Kim, Y. Han and J. Park. **Evaluation of permeable pore sizes of macroporous materials using a modified gas permeation method**. *Materials Characterization*, **60**(1):14 – 20, 2009.

[180] N. Epstein. **On tortuosity and the tortuosity factor in flow and diffusion through porous media**. *Chemical engineering science*, **44**(3):777–779, 1989.

[181] E.G. Hoffmann. **Calculation of Relative Molar Response Factors of Thermal Conductivity Detectors in Gas Chromatography**. *Analytical Chemistry*, **34**:1216–1222, 1962.

[182] A. Hernández, JI Calvo, P. Prádanos and F. Tejerina. **Pore size distributions in microporous membranes. A critical analysis of the bubble point extended method**. *Journal of Membrane Science*, **112**(1):1–12, 1996.

[183] B. Duncan, J. Urquhart and S. Roberts. **Review of Measurement and Modelling of Permeation and Diffusion in Polymers**. *National Physical Laboratory REPORT*, **12**, 2005.

[184] A. Bandy, D. Thornton and A. Driedger III. **Airborne Measurements of Sulfur Dioxide, Dimethyl Sulfide, Carbon Disulfide, and Carbonyl Sulfide by Isotope Dilution Gas Chromatography**. *Mass Spectrometry. Journal Geophysical Research*, **98**:23423–23433, 1993.

[185] BW Blomquist, BJ Huebert, CW Fairall and IC Faloona. **Determining the sea-air flux of dimethylsulfide by eddy correlation using mass spectrometry**. *Atmos. Meas. Tech*, **3**:1–20, 2010.

[186] L. Huang, P. Hsu, C. Kuo, S. Chen and J. Lai. **Pore size control of PTFE membranes by stretch operation with asymmetric heating system**. *Desalination*, **233**(1-3):64 – 72, 2008.

[187] O. Soppart and JI Baumbach. **Comparison of electric fields within drift tubes for ion mobility spectrometry**. *Measurement Science and Technology*, **11**(10):1473–9, 2000.

[188] K.J. Gillig, B.T. Ruotolo, E.G. Stone and D.H. Russell. **An electrostatic focusing ion guide for ion mobility-mass spectrometry**. *International Journal of Mass Spectrometry*, **239**(1):43–49, 2004.

[189] E.C. Lynn, M.C. Chung and C.C. Han. **Characterizing the transmission properties of an ion funnel**. *Rapid Communications in Mass Spectrometry*, **14**(22):2129–2134, 2000.

[190] AV Tolmachev, T. Kim, HR Udseth, RD Smith, TH Bailey and JH Futrell. **Simulation-based optimization of the electrodynamic ion funnel for high sensitivity electrospray ionization mass spectrometry**. *International Journal of Mass Spectrometry*, **203**(1):31–47, 2000.

[191] R.R. Julian, S.R. Mabbett and M.F. Jarrold. **Ion Funnels for the Masses: Experiments and Simulations with a Simplified Ion Funnel**. *Journal of the American Society for Mass Spectrometry*, **16**(10):1708–12, 2005.

[192] J. Xu and W.B. Whitten. **Monte Carlo simulation of ion transport in ion mobility spectrometry**. *International Journal for Ion Mobility Spectrometry*, **11**:13–17, 2008.

[193] VL Varentsov and AA Ignatiev. **Numerical investigations of internal supersonic jet targets formation for storage rings**. *Nuclear Instruments and Methods in Physics Research Section A: Accelerators, Spectrometers, Detectors and Associated Equipment*, **413**(2-3):447–456, 1998.

[194] JB Neumayr, L. Beck, D. Habs, S. Heinz, J. Szerypo, PG Thirolf, V. Varentsov, F. Voit, D. Ackermann, D. Beck et al. **The ion-catcher device for SHIPTRAP**. *Nuclear Inst. and Methods in Physics Research, B*, **244**(2):489–500, 2006.

[195] R.T. Kelly, A.V. Tolmachev, J.S. Page, K. Tang and R.D. Smith. **The ion funnel: Theory, implementations, and applications**. *Mass Spectrometry Reviews*, 2009.

[196] S.A. Shaffer, K. Tang, G.A. Anderson, D.C. Prior, H.R. Udseth and R.D. Smith. **A novel ion funnel for focusing ions at elevated pressure using electrospray ionization mass spectrometry**. *Rapid Communications in Mass Spectrometry*, **11**(16):1813–1817, 1997.

[197] P.R. Kemper, N.F. Dupuis and M.T. Bowers. **A new, higher resolution, ion mobility mass spectrometer**. *International Journal of Mass Spectrometry*, 2009.

[198] R.D. Smith, K. Tang and J.S. Page. **An electrodynamic ion funnel interface for greater sensitivity and higher throughput with linear ion trap mass spectrometers**. *International Journal of Mass Spectrometry*, **265**(2-3):244–250, 2007.

[199] D. Gerlich. **Inhomogeneous RF fields: a versatile tool for the study of processes with slow ions**. *Advances in Chemical Physics*, **82**(1), 1992.

[200] S.A. Shaffer, A. Tolmachev, D.C. Prior, G.A. Anderson, H.R. Udseth and R.D. Smith. **Characterization of an improved electrodynamic ion funnel interface for electrospray ionization mass spectrometry**. *Analytical Chemistry*, **71**(15):2957–2964, 1999.

[201] AV Tolmachev, AF Dodonov, IV Chernushevich and KG Standing. **A collisional focusing ion guide for coupling an atmospheric pressure ion source to a mass spectrometer**. *Nuclear Instruments and Methods in Physics Research Section B: Beam Interactions with Materials and Atoms*, **124**(1):112–119, 1997.

[202] J.S. Page, A.V. Tolmachev, K. Tang and R.D. Smith. **Theoretical and experimental evaluation of the low m/z transmission of an electrodynamic ion funnel**. *Journal of the American Society for Mass Spectrometry*, **17**(4):586–592, 2006.

[203] D. Gerlich. **State-selected and state-to-state ion-molecule reaction dynamics. Part 1. Experiment**. *Advances in Chemical Physics*, **82**(1), 1992.

[204] RM Moision and PB Armentrout. **An Electrospray Ionization Source for Thermochemical Investigation with the Guided Ion Beam Mass Spectrometer**. *Journal of the American Society for Mass Spectrometry*, **18**(6):1124–1134, 2007.

[205] J.S. Page, K. Tang, R.T. Kelly and R.D. Smith. **Subambient Pressure Ionization with Nanoelectrospray Source and Interface for Improved Sensitivity in Mass Spectrometry**. *Analytical Chemistry*, **80**(5), 2008.

[206] Q. Zhao, M.W. Soyk, G.M. Schieffer, K. Fuhrer, M.M. Gonin, RS Houk and E.R. Badman. **An Ion Trap-Ion Mobility-Time of Flight Mass Spectrometer with Three Ion Sources for Ion/Ion Reactions**. *Journal of the American Society for Mass Spectrometry*, **20**(8):1549–1561, 2009.

[207] DJ Jacob, EG Heikes, S.M. Fan, JA Logan, DL Mauzerall, JD Bradshaw, HB Singh, GL Gregory, RW Talbot, DR Blake et al. **Origin of ozone and NOx in the tropical troposphere: A photochemical analysis of aircraft observations over the South Atlantic basin**. *Journal of Geophysical Research*, **101**(D19):24235, 1996.

[208] G.H. Mount, F.L. Eisele, D.J. Tanner, J.W. Brault, P.V. Johnston, J.W. Harder, E.J. Williams, A. Fried and R. Shetter. **An intercomparison of spectroscopic laser long-path and ion-assisted in situ measurements of hydroxyl concentrations during the Tropospheric OH Photochemistry Experiment, fall 1993**. *Journal of geophysical research*, **102**(D5):6437–6455, 1997.

[209] CN Hewitt, S. Hayward and A. Tani. **The application of proton transfer reaction-mass spectrometry (PTR-MS) to the monitoring and analysis of volatile organic compounds in the atmosphere**. *Journal of Environmental Monitoring*, **5**(1):1–7, 2003.

[210] A. Guenther, T. Karl, P. Harley, C. Wiedinmyer, P. I. Palmer and C. Geron. **Estimates of global terrestrial isoprene emissions using MEGAN (Model of Emissions of Gases and Aerosols from Nature)**. *Atmospheric Chemistry and Physics*, **6**(11):3181–3210, 2006.

[211] J.L. Funk, C.G. Jones, C.J. Baker, H.M. Fuller, C.P. Giardina and M.T. Lerdau. **Diurnal variation in the basal emission rate of isoprene**. *Ecological Applications*, **13**(1):269–278, 2003.

[212] D.D. Lucas and R.G. Prinn. **Parametric sensitivity and uncertainty analysis of dimethylsulfide oxidation in the clear-sky remote marine boundary layer**. *Atmospheric Chemistry and Physics*, **5**(6):1505–1525, 2005.

[213] Y. Sheng, F. Chen, Y. Yu, X. Wang, G. Sheng, J. Fu and E. Zeng. **Emission of volatile organic sulfur compounds from a heavily polluted river in Guangzhou, South China**. *Environmental Monitoring and Assessment*, **143**:121–130, 2008.

[214] B. Ginzburg, I. Chalifa, J. Gun, I. Dor, O. Hadas and O. Lev. **DMS Formation by Dimethylsulfoniopropionate Route in Freshwater**. *Environmental Science & Technology*, **32**(14):2130–2136, 1998.

[215] S.-L. Sihto, M. Kulmala, V.-M. Kerminen, M. Dal Maso, T. Petj, I. Riipinen, H. Korhonen, F. Arnold, R. Janson, M. Boy, A. Laaksonen and K. E. J. Lehtinen. **Atmospheric sulphuric acid and aerosol formation: implications from atmospheric measurements for nucleation and early growth mechanisms**. *Atmospheric Chemistry and Physics*, **6**(12):4079–4091, 2006.

[216] J.S. Page, A.V. Tolmachev, K. Tang and R.D. Smith. **Variable low-mass filtering using an electrodynamic ion funnel**. *Journal of Mass Spectrometry*, **40**(9):1215, 2005.

[217] J.A. Logan, M.J. Prather, S.C. Wofsy and M.B. McElroy. **Tropospheric chemistry: A global perspective**. *Journal of Geophysical Research*, **86**(C8):7210–7254, 1981.

[218] C. Jost, J. Trentmann, D. Sprung, M.O. Andreae, J.B. McQuaid and H. Barjat. **Trace gas chemistry in a young biomass burning plume over Namibia: Observations and model simulations**. *Journal of Geophysical Research*, **108**(D13):8482, 2003.

[219] SM Miller, DM Matross, AE Andrews, DB Millet, M. Longo, EW Gottlieb, AI Hirsch, C. Gerbig, JC Lin, BC Daube et al. **Sources of carbon monoxide and formaldehyde in North America determined from high-resolution atmospheric data**. *Atmospheric Chemistry and Physics*, **8**:7673–7696, 2008.

[220] Z. Luo, D. Kley, R.H. Johnson and H. Smit. **Ten years of measurements of tropical upper-tropospheric water vapor by MOZAIC. Part II: assessing the ECMWF humidity analysis**. *Journal of Climate*, **21**(7):1449–1466, 2008.

[221] Z. Luo, D. Kley, R.H. Johnson and H. Smit. **Ten years of measurements of tropical upper-tropospheric water vapor by MOZAIC. Part I: Climatology, variability, transport, and relation to deep convection**. *Journal of Climate*, **20**(3):418–435, 2007.

[222] V. Thouret, J.P. Cammas, B. Sauvage, G. Athier, R. Zbinden, P. Nédélec, P. Simon and F. Karcher. **Tropopause referenced ozone climatology and inter-annual variability (1994–2003) from the MOZAIC programme**. *Atmospheric Chemistry and Physics*, **6**(4):1051, 2006.

[223] T. Machida, H. Matsueda and Y. Sawa. **A new JAL project: CONTRAIL-Comprehensive Observation Network for Trace gases by AIrLiner**. *IGAC Newsletter*, **37**:23–30, 2007.

[224] A. Zahn and C.A.M. Brenninkmeijer. **New Directions: A Chemical Tropopause Defined**. *Atmospheric Environment*, **37**(3):439–440, 2003.

[225] MP Scheele, PC Siegmund and PFJ Van Velthoven. **Sensitivity of trajectories to data resolution and its dependence on the starting point: in or outside a tropopause fold**. *Meteorological Applications*, **3**(3):267–273, 1996.

[226] A. Zahn, R. Neubert, M. Maiss and U. Platt. **Fate of long-lived trace species near the Northern Hemispheric tropopause: Carbon dioxide, methane, ozone, and sulfur hexafluoride**. *Journal of Geophysical Research*, **104**(D11):13923–13942, 1999.

[227] M. Koeppe, M. Hermann, CAM Brenninkmeijer, J. Heintzenberg, H. Schlager, T. Schuck, F. Slemr, D. Sprung, PFJ van Velthoven, A. Zahn Wiedensohler and H. Ziereisand. **Origin of aerosol particles in the midlatitude and subtropical upper troposphere and lowermost stratosphere from cluster analysis of CARIBIC data**. *Atmospheric Chemistry and Physics*, **9**:8413–8430, 2009.

[228] GJ Frost, A. Fried, YN Lee, B. Wert, B. Henry, JR Drummond, MJ Evans, F.C. Fehsenfeld, PD Goldan, JS Holloway et al. **Comparisons of box model calculations and measurements of formaldehyde from the 1997 North Atlantic Regional Experiment**. *Journal of Geophysical Research*, **107**(10.1029), 2002.

[229] AJG Baumgaertner, P. Jöckel and C. Brühl. **Energetic particle precipitation in ECHAM5/MESSy1–Part 1: Downward transport of upper atmospheric NOx produced by low energy electrons**. *Atmospheric Chemistry and Physics*, **9**:2729–2740, 2009.

[230] AJG Baumgaertner, P. Jöckel, H. Riede, G. Stiller and B. Funke. **Energetic particle precipitation in ECHAM5/MESSy–Part 2: Solar proton events**. *Atmospheric Chemistry and Physics*, **10**:7285–7302, 2010.

[231] G. Smiatek, B. Rockel and U. Schattler. **Time invariant data preprocessor for the climate version of the COSMO model (COSMO-CLM)**. *Meteorologische Zeitschrift*, **17**(4):395–405, 2008.

[232] A. Dobler and B. Ahrens. **Analysis of the Indian summer monsoon system in the regional climate model COSMO-CLM**. *Journal of Geophysical Research*, **115**(D16):D16101, 2010.

[233] MO Andreae, P. Artaxo, H. Fischer, SR Freitas, JM Gregoire, A. Hansel, P. Hoor, R. Kormann, R. Krejci, L. Lange et al. **Transport of biomass burning smoke to the upper troposphere by deep convection in the equatorial region**. *Geophys. Res. Lett*, **28**(6):951–954, 2001.

[234] T. Reiner, D. Sprung, C. Jost, R. Gabriel, OL Mayol-Bracero, MO Andreae, TL Campos and RE Shelter. **Chemical characterization of pollution layers over the tropical Indian Ocean: Signatures of emissions from biomass and fossil fuel burning**. *Journal of Geophysical Research*, **106**(D22):28497, 2001.

[235] PJ Slevin and WW Harrison. **The hollow cathode discharge as a spectrochemical emission source**. *Applied Spectroscopy Reviews*, **10**(2):201–255, 1975.

[236] P.H. Dawson. **Quadrupole mass spectrometry and its applications**. 1995.

[237] D.J. Douglas. **Linear quadrupoles in mass spectrometry**. *Mass Spectrometry Reviews*, **28**(6):937–960, 2009.

[238] P. H. Dawson. **Performance characteristics of an r.f.-only quadrupole**. *International Journal of Mass Spectrometry and Ion Processes*, **67**(3):267 – 276, 1985.

List of Figures

LIST OF FIGURES

List of Tables

Acknowledgements

I gratefully acknowledge the supervision of Prof. Johannes Orphal and his valuables comments to the draft of this thesis.

I thank Prof. Thomas Leisner for participating in this doctoral work as co-supervisor.

I acknowledge the team which I had the privilege to be part of, including Helmut Widmann, Lisa Kattner, Shahrokh Sanati and, former members, Detlev Sprung and Josef Weppner. Many thanks to Christoph Dyroff, Felix Geiger and Marco Neumaier, I appreciate immensely the careful revision of the manuscript and the many fruitful discussions.

I thank the group leader, Dr. Andreas Zahn for his support and the creative environment which has pushed me further.

I would like to thank Alexander Streilli and co-workers at the IMK workshop. The high quality of your work has made the construction of the PTR-IF-MS possible.

To Frank Helleis and Michael Flanz, MPI-CH, Mainz, thank you for the helpful support during the implementation of the V-25 computer.

To Prof. Manfred Kappes and Dr. Patrick Weis, I gratefully acknowledge the valuable discussions on ion funnel technology.

I gratefully acknowledge the financing of the instrument development and my position by the Helmholtz Association of German Research Centres (HGF) and the German Research Foundation (DFG).

ACKNOWLEDGEMENTS

I would like to thank as well all the people that were not directly involved with this work but made me feel at home during my time in Germany: Andreas Keller, Ellen-Rose Trübger, Gerhard Höhne, Ronald Wallstabe, Serge Van Criekingen, Vitor de Souza, among many others.

To my family in Brazil, thank you for the support at all times. You are the best family a person could ask for.

And to my fiancée Ananda, I thank you for been by my side with patience and understanding during the most-demanding periods of this work. It could not have been achieved without your love and support.